6-1-2012

Kinetically Controlled Synthesis of Triblock Copolymer Stabilized Gold Nanoparticles

Theodore Saleem Sabir
Loma Linda University

LOMA LINDA UNIVERSITY
School of Medicine
in conjunction with the
Faculty of Graduate Studies

————————————————

Kinetically Controlled Synthesis of Triblock Copolymer Stabilized
Gold Nanoparticles

by

Theodore Saleem Sabir

————————————————

A dissertation submitted in partial satisfaction of
the requirements for the degree of
Doctor of Philosophy in Biochemistry

————————————————

June 2012

Each person whose signature appears below certifies that this dissertation in his/her opinion is adequate, in scope and quality, as a dissertation for the degree Doctor of Philosophy.

_____ , Chairperson
Christopher C. Perry, Assistant Professor of Biochemistry

_____
Danilo Boskovic, Assistant Professor of Biochemistry

_____
Eileen Brantley, Assistant Professor of Pharmacology

_____
Penelope Duerksen-Hughes, Professor of Biochemistry

_____
R. Steven Kurti, Associate Professor of Dental Research

_____
Jamie Milligan, Professor of Radiation Chemistry

ACKNOWLEDGMENTS

"Isaac reopened the wells that had been dug in the time of his father Abraham, which the Philistines had stopped up after Abraham died, and he gave them the same names his father had given them. Isaac's servants dug in the valley and discovered a well of fresh water there. But the herdsmen of Gerar quarreled with Isaac's herdsmen and said, "The water is ours!" So he named the well Esek, because they disputed with him. Then they dug another well, but they quarreled over that one also; so he named it Sitnah. He moved on from there and dug another well, and no one quarreled over it. He named it Rehoboth, saying, "Now the Lord has given us room and we will flourish in the land." From there he went up to Beersheba. That night the Lord appeared to him and said, "I am the God of your father Abraham. Do not be afraid, for I am with you; I will

bless you and will increase the number of your descendants for the

sake of my servant Abraham."

Genesis

CONTENT

TABLES

FIGURES

SCHEMES

ABBREVIATIONS

AFM	Atomic force microscopy
AuNP	Gold nanoparticle
BHT	Butylated hydroxytoluene
CMC	Critical micelle concentration
CMT	Critical micelle temperature
CP	Cloud point
CTAB	Cetyltrimethylammonium bromide
DLS	Dynamic light scattering
DPD	Dissipative particle dynamics
ESR	Electron spin resonance
FESEM	Field emission scanning electron microscopy
FTIR	Fourier transform infrared spectroscopy
FWHM	Full width half maximum
$HAuCl_4$	Tetrachloroauric (III) acid
$HAuCl_4.3H_2O$	Tetrachloroaurate (III) Hydrate
HMW	High molecular weight
KJMA	Kolmogorov-Johnson-Mehl-Avrami
LMCT	Ligand-to-metal charge transfer
LMW	Low molecular weight
LSPRs	Localized surface Plasmon resonances
PEG	Polyethylene glycol
PEO	Poly ethylene oxide

PPO	Poly propylene oxide
PVDF	Polyvinylidene fluoride
NMR	Nuclear magnetic resonance
SANS	Small angle neutron scattering
SERS	Surface-enhanced Raman scattering
STEM	Scanning transmission electron microscopy
TBP	Triblock copolymers
TEM	Transmission electron microscopy
XRD	X-ray diffraction

ABSTRACT OF THE DISSERTATION

Kinetically Controlled Synthesis of Triblock Copolymer Stabilized
Gold Nanoparticles

by

Theodore Saleem Sabir

Doctor of Philosophy, Graduate Program in Biochemistry
Loma Linda University, June 2012
Dr. Christopher C. Perry, Chairperson

Concerns for the environmental and economic impact of organic solvents in gold nanoparticle synthesis have motivated the search for more environmentally benign alternatives. One viable approach is the synthesis of AuNPs from tetrachloroauric(III) acid ($HAuCl_4$) using triblock copolymers (TBPs). However, a major challenge of using TBPs is the heterogeneous nature of the formed nanocrystals. Establishing control over AuNP size and shape requires a detailed mechanistic understanding of precursor reduction and nanoparticle growth. By using mixtures of TBPs (L31 and F68), a more flexible method to tune AuNP size and shape is demonstrated. This is achieved by adjusting the TBP/Au(III) ratio and the concentrations of seed citrate-stabilized AuNPs. Kinetic models are used to explain why L31 inhibits the rate of AuNP formation and growth. Experimental evidence of sigmoidal growth kinetics, early time bimodal gold nanoparticle size distributions, and polycrystallinity suggest that aggregative AuNP growth is an important mechanism.

CHAPTER ONE

INTRODUCTION

The field of nanoscience involves the study of objects and systems where at least

one dimension is in the range of 1-100 nm.[1] At this level, objects and systems have

length scales in the size range needed to define the physical properties of materials.[2] The

term nanotechnology, as defined by NASA, refers to the "creation of functional

materials, devices and systems through control of matter on the nanometer scale (1-100

nm), and exploitation of novel phenomena and properties (physical, chemical,

biological)".[3] The field of nanotechnology branches into areas of science such as

biochemistry, organic chemistry, molecular biology, physics and surface science.

Nanotechnology is currently one of the fastest growing technologies with substantial

impacts in the development and design of a host of novel products. Some products may

even be revolutionary or paradigm-shifting in their applications. Current research in

nanotechnology is driven by the desire to find new materials with unique properties at the

nanoscale. An example of such an attempt is the nanocar (Figure 1.1).[4] These efforts are

exploiting the unique characteristic phenomena that are governed by the principles of

quantum mechanics.
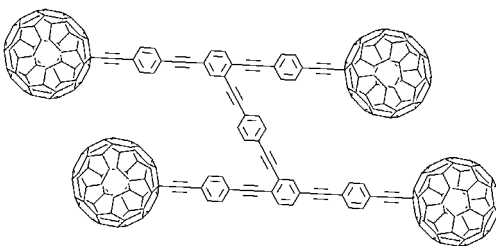
Figure 1.1 An example of a nanocar.[4]

The advancements in synthetic chemistry enable the preparation of small

molecules with specific useful structures. Interfacial and colloidal sciences are producing

a growing selection of strategies to construct materials. This, in its broadest terms,

represents nanochemistry, a branch of synthetic chemistry that is used to make nanoscale

building blocks of varying sizes, shapes, compositions, structure, charge and

functionality. Such structures cover the range from carbon nanostructures (nanotubes,

nanoparticles, fullerenes and nanorods)[5,6,7,8,9] to DNA origami.[10]

The intense focus on nanomaterials is based upon the fact that fundamental

physical and electronic properties are substantially different at this scale. In particular, the

high surface-to-volume ratio imparts high reactivity potential for catalysis or sensor

applications.[11] The volume of an object $V \propto l^3$, (where l is the characteristic atomic

length) decreases with scale more rapidly than does the surface area ($S \propto l^2$) : $S/V \propto l^{-1}$.

This scaling dependence is reflected in the observed changes of certain material

properties, such as the melting point for example.[3] Furthermore, such changes in material

properties relative to bulk characteristics can be modified without change in chemical

composition (e.g. magnetization, optical properties (color), melting point, hardness, etc.).

The changes in the bulk properties such as decreased melting point, solubility, or

increased hardness are related to the higher surface energy due to higher density of surface atoms. Similarly, the size tunable electronic properties are rationalized by quantum-confinement effects. Generally, the nanomaterials may be categorized in terms of quantum confinement[12] or in terms of dimensionality[13] (Table 1.1).

Table 1.1 Examples of reduced-dimensionality systems.[12]

3D confinement (0-D)	2D confinement (1-D)	1D confinement (thin films) (2-D)
Fullerenes	Carbon nanotubes and nanofilaments	Nanolaminated materials
Colloidal particles		Grain boundary films
Nanoporous silicon	Metal and magnetic nanowires	Clay platelets
Activated carbons	Oxide and carbide nanorods	Semiconductor quantum wells
Nitride and carbide precipitates in high-strength low-alloy steels	Semiconductor quantum wires	Langmuir-Blodgett films
Semiconductor		Grapheme/grapheme oxide films
Semiconductor quantum dots		
Quasi-crystals		

For clarity, additional terms are sometimes employed: nanoparticle, nanocluster, nanopowder, colloid, nanocrystal, and quantum dot. *Nanoparticles* are defined as amorphous or semi-crystalline 0-D nanostructures with dimensions larger than 10 nm, and a relatively large (15%) size dispersion. For amorphous/semi-crystalline nanostructures smaller in size (i.e., 1–10 nm), with narrow size distribution, the term *nanocluster* is more often used. In contrast, *colloidal* materials are more polydisperse and less well characterized (Table 1.2). The agglomeration of noncrystalline nanostructural subunits should best be termed a *nanopowder*. Any nanomaterial that is crystalline is referred to as a *nanocrystal*. A special case of nanocrystal that is composed from semiconductor material is called a *quantum dot* (QD).[13]

A Table 1.2 Comparison of 0-D nanoarchitectures with traditional colloids.[14]

Nanoparticles/nanoclusters	Colloids
Size: 1–100 nm (nanoclusters: 1–10 nm)	Typically >10 nm
Homogeneous molecular composition >15% Size dispersion (less polydispersity for nanoclusters relative to nanoparticles)	Poorly defined compositions >15% Size dispersion
Reproducible synthesis (control over size, shape, and composition)	Nonreproducible, uncontrollable morphology/ composition
Reproducible physical properties and catalytic activity	Nonreproducible properties
Soluble in polar/nonpolar organic solvents	Typically only soluble in polar solvents
Contain clean surfaces	Contain surface-adsorbed species such as —OH, —X, —OH_2, etc.

Nanoparticles
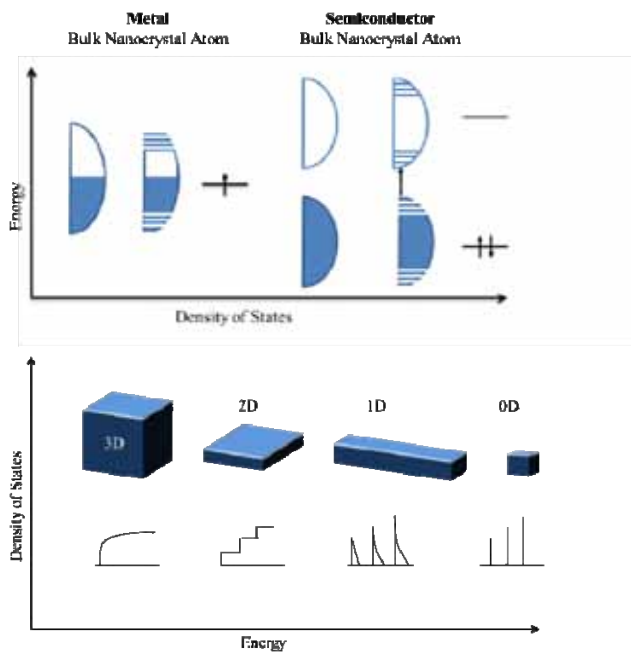
Figure 1.2   Density of States.   Upper panel: Schematic illustration comparing the density of states of metal with that of semiconductor clusters. Lower panel: Density of states for a semiconductor as a function of dimension.

Optical Properties of Nanoparticles

The size and shape of noble metal (Au, Ag) nanoparticles affect the color of their appearance.[15] Gold nanoparticle spheres in a polar solvent have a characteristic red color, while silver nanoparticle spheres appear yellow.[16] The origin of the color, is not due to quantum confinement as in semiconductor nanocrystals, as there is no bandgap between valence and conduction bands, and the energy states form a continuum analogous to bulk metal (Figure 1.2).[17] Theoretical treatments have shown that the color is due to the collective oscillation of the free electrons in the conduction band, known as surface plasmon resonance (SPR) or localized surface plasmon resonance (LSPR).[2, 15b] This oscillation frequency is usually in the visible region for gold and silver. In contrast to quantum dots where the size variation alters the optical properties of the nanoparticles, when metal nanoparticles are enlarged, the optical properties are altered only slightly. However, if anisotropy with respect to shape and size is involved, such as is present in nanorods when compared to nanospheres, the optical properties can change significantly.
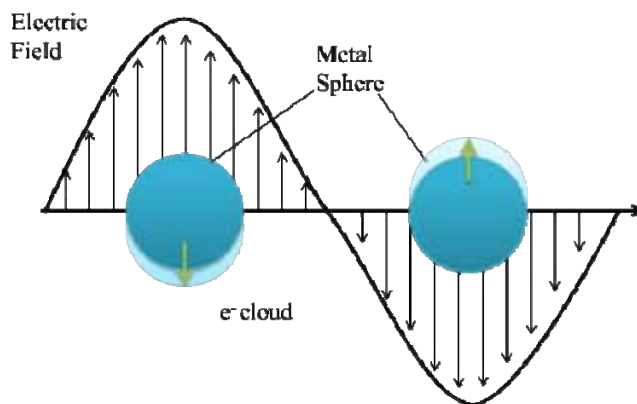
Figure 1.3 Plasmon Resonance. Schematic of plasmon oscillation for a sphere, showing the displacement of the conduction electron charge cloud relative to the nuclei.[2]

What is the origin of the LSPR? As the mean free path of an electron is ~50 nm for gold and silver, there will be minimal electron scattering from the bulk particles which are below this in size. Thus, light-matter interactions will occur at the surface and when the wavelength of light is much larger than the nanoparticle size, standing resonance conditions are produced. Light in resonance with the conduction electron plasmon frequency will cause oscillations of the metal conduction electrons (Figure 1.3). This resonance condition is found to be dependent upon the shape, size, and dielectric constants of both the metal and the surrounding medium.[2] The effects of shape and size can be explained by the change in the electric field density at the surface resulting in a change in the apparent cross-sections of nanoparticles and their optical properties including absorption and scattering.

The surrounding dielectric on the NP surface will affect the oscillation frequency due to its effects on the ability of the surface to accommodate electron charge density from the nanoparticles. This includes the solvent and the capping material. The capping material, however, is more important in determining the plasmon resonance shift. Thus, chemically bonded molecules can be detected by observing the change they induce in the electron density on the surface, *i.e.*, SPR shift. This is the basis for the use of noble metal nanoparticles as sensitive sensors. The SPR can be calculated analytically in the case of spherical particles by solving Maxwell's equations for small spheres interacting with an electromagnetic field. Modern approaches use numerical methods such as discrete dipole approximation (DDA) to calculate SPR for arbitrary nanoparticle geometries.[18]

The photochemistry or "the chemistry of light" is an important investigative study tool to understand the behavior of molecules. Light introduces a minimal perturbation

during observations and readily transmits through space. Technical advances in light sources such as optical filters and photon counting detectors are employed in optical imaging systems. Using sensitive imaging systems we can quantitatively analyze a variety of chemical reactions on the molecular level or with respect to molecular aggregates. The nanoparticle surface properties are easily affected by particle morphologies and surrounding dielectric environments.[19]

Gold Nanoparticles

Gold (Au) is historically regarded as the elite element. It was one of the first precious metals to be discovered and studied. Colloidal gold held an important role in medicine as early as the fourth and fifth centuries when Chinese and Indian physicians used it to treat patients. Then during the Middle Ages, European alchemists studied gold's medicinal uses and the possibility of making gold out of other metals.[20] Alchemist Paracelsus and his contemporary Giovanni Andrea used Aurum potable to treat mental illness, ulcers, epilepsy and diarrhea.[20a, 21] In 1618 philosopher and doctor of medicine Franscisco Antonii published a book that contains information on the preparation of colloidal gold and its medical applications.[20b] Colloidal gold continued to be used to treat various diseases including cancer.[22,21] With advancing technology new applications for colloidal gold or AuNPs emerged including catalytic processes, delivery of low and high molecular weight drugs, cellular delivery of bio-macromolecules and medical imaging.[15a, 23]

Gold compounds and their photochemistries is complex and are described in literature over nearly three hundred years. Recent research led to a deeper understanding

of a variety of unique complexes of gold. Light sensitive Au (I) and Au (III) compounds are classified according to the nature of reactive excited states.[24] These include metal-centered, ligand-to-metal charge transfer, metal-to-ligand charge transfer, metal-to-metal charge transfer and intra ligand.[25]

Chemical and Physical Properties of Gold Nanoparticles

Nanomaterials possess unique properties that are not observed in their bulk counterparts and that are affected by the sizes and shapes of the nanoparticles.[26] Many fundamental properties including crystalline phases, electronic properties and LSPRs are size dependent. Surface free energies and surface stress are important components to the overall phase stability. For nanoparticles free energies of surface is a large component of the total free energy. Electronic properties are also size dependent, specifically the electronic band gap. Changes in the band gap will influence many properties including surface reactivity. Size will also alter the LSPR. Gold has an LSPR that can occur throughout the visible region of the spectrum depending on the size of the nanoparticle. Though, size is not the only factor that influences LSPR as the shape has also been known to affect these phenomena. Shape influences the extinction spectra by red-shifting the LSPR into the near-infrared region of the electromagnetic spectrum. Surface properties such as aggregation and concentration will also affect the chemical reactivity of the nanoparticles.[21,26,27]

Recently there has been much research on the optical properties of AuNPs because of their potential biomedical applications. AuNPs can enhance the light absorption, light scattering, local electromagnetic field and fluorescence. This

enhancement is due to the unique interaction of light with the free electrons in the gold. When AuNPs are exposed to light, the electric field of light causes the collective oscillation of the conduction-band electrons (LSPRs) at the surface of the nanoparticle.[26,27] For gold nanorods the electrons oscillate along both the long and short axis resulting in a resonance band in the near-infrared region and a weak band in the visible region.[23a] The excitation of the SPR results in the enhancement of the photophysical properties of the AuNPs. Rayleigh scattering, also known as light scattering, is enhanced because of the excitation of the SPR. Since AuNPs have high-scattering cross-section and have superior photostability, they can be used for imaging intensive medical applications.

AuNPs also possess surface-enhanced Raman scattering (SERS). SERS results from two factors: long range electromagnetic enhancement and short-range chemical enhancement.[16b] Long-range electromagnetic enhancement is due to the resonance of the applied light field with the collective electron oscillations of the nanoparticles resulting in strongly enhanced local electric fields at the surface. Short-range chemical enhancement is due to a change in the molecular polarizability by the charge transfer interaction of the molecules with the metal surface and interaction with atoms near the metal surface.[28] AuNPs have been used as SERS substrates to probe components in living cells. AuNPs absorb light strongly and quickly convert it into heat. The highly efficient and localized light to heat conversion can be useful for the photothermal therapy of cancers.[29]

Synthesis and Characterization of Gold Nanoparticles

Synthesis Techniques

There are two methods to synthesize nanoparticles. In the "bottom-up" approach materials can be built from molecular components by principles of chemical and molecular recognition. In the "top-down" approach larger objects are broken down and small objects constructed from larger entities without atomic-level control. Top-down approach uses electromagnetic radiation either photon and or electron beam lithography to etch into surfaces and create two or three-dimensional structures. Bottom-up methods use organic and inorganic synthesis to create three-dimensional structures.[30] Solution based AuNP synthesis uses a bottom-up approach introduced first by Turkevitch in 1951.[31] This approach was improved upon by Frens in 1973.[32] In 1994 the Brust-Schiffrin method for AuNP synthesis was published. This synthesis uses a two-phase system. $AuCl_4^-$ is transferred to toluene using tetraoctylammonium bromide as the phase transfer reagent and reduced by $NaBH_4$ in the presence of dodecanethiol, other sulfur ligands can also be used.[11]

Currently researchers are working to create methods to synthesize anisotropic AuNPs through a seed methodology. Seed methodology uses a small amount of gold precursor i.e., citrate nanoparticles as a platform to synthesis larger nanoparticles. Liz-Marzan et al.[33] synthesized triangular/hexagonal and smaller pseudo-spherical gold NPs from $HAuCl_4$ using salicylic acid. Similarly, nanoplates were made using aspartic acid,[34] with the assistance of UV-vis irradiation,[35] or by using gamma irradiation in a reaction medium containing gold(I) and ascorbic acid in the presence of CTAB.[36] In this work, I demonstrate a more environmentally begin seeding methodology by using triblock

copolymers (TBPs) to produce hexagonal/triangular and smaller pseudo-spherical AuNPs. Size and shape control is important because the newly synthesized particle's physical and chemical properties depend on the size and shape.

Characterization Techniques

Characterization techniques are central to fully understand the exact nature of synthesized nanomaterials. There are a variety of analytical methods that have been successfully applied to the characterization of nanomaterials. Typically, spectroscopic and scattering characterization techniques span the electromagnetic spectrum (Table 1.3). These methods can be sub-divided into spectroscopic, scattering, and microscopy techniques that primarily grew out of the field of colloidal chemistry. Table 1.4 summaries the advantages and disadvantages of each characterization technique.

Table 1.3 Wavelengths and frequencies for different types of electromagnetic waves.

Type of Electromagnetic Wave	Wavelength(m)	Frequency (Hz)
Radio	10^3	10^4
Microwave	10^{-2}	10^8
Infrared	10^{-5}	10^{12}
Visible		
Red	$750\text{-}620 \times 10^{-9}$	$400\text{-}484 \times 10^{12}$
Orange	$620\text{-}590 \times 10^{-9}$	$484\text{-}508 \times 10^{12}$
Yellow	$590\text{-}570 \times 10^{-9}$	$508\text{-}526 \times 10^{12}$
Green	$570\text{-}495 \times 10^{-9}$	$526\text{-}606 \times 10^{12}$
Cyan	$495\text{-}476 \times 10^{-9}$	$606\text{-}630 \times 10^{12}$
Blue	$475\text{-}450 \times 10^{-9}$	$631\text{-}668 \times 10^{12}$
Violet	$450\text{-}380 \times 10^{-9}$	$668\text{-}789 \times 10^{12}$
Ultraviolet	$400\text{-}10 \times 10^{-9}$	$10^{15}\text{-}10^{16}$
X-Ray	10^{-10}	10^{18}
Gamma Ray	10^{-12}	10^{20}

$$\nu = \frac{c}{\lambda}$$

Scattering Techniques

The scattering methodologies for characterization of nanomaterials include dynamic light scattering, Raman scattering and X-ray diffraction approaches.

Dynamic Light Scattering (DLS). This technique allows particle sizing down to 1 nm diameter. Typical applications include the characterization of emulsions, micelles, polymers, proteins, nanoparticles or colloids. DLS can be used to determine the size distribution profile of small particles and probe the behavior of complex fluids such as concentrated polymer solutions. These techniques depend on scattering of the energized particles' within the sample. They provide important information about the structure,

hydrodynamic size, aggregation and morphology. Of the various scattering techniques available DLS is probably the most commonly used for characterizing the hydrodynamic size. It is simple, noninvasive and nondestructive. In this technique the fluctuations in the scattered light intensity due to the Brownian motion of the particles are used to determine the particle diffusion coefficient which is then related to its hydrodynamic radius. Some groups have used this technique to even explore the effect of physiologically relevant dosing media on a variety of unmodified nanomaterials.[37]

Raman Scattering. Raman techniques maybe applied to the characterization of NPs. Raman spectroscopy measures the inelastic scattering of monochromatic radiation (UV, visible, or near IR) by a sample. If the final vibrational state of the molecule is more energetic than the initial then the emitted photon will be shifted to a lower frequency in order for the total energy of the system to remain balanced. This shift in frequency is designated as a Stokes shift. If the final vibrational state is less energetic than the initial then the emitted photon will be shifted to a higher frequency and this is designated as an Anti-Stokes shift. The incident light becomes either Stokes or anti-Stokes shifted in wavelength resulting in sharp fingerprint Raman bands that are characteristic of the sample and complementary to infrared (IR) spectroscopy. It was observed that carbon nanotubes show Raman scattering which is sensitive to isotope composition.[38] Some groups used Raman spectroscopy to investigate the noncovalent interaction between pyrene-labeled cellulose and multi-walled carbon nanotubes.[39]

X-ray Diffraction. X-ray diffraction (XRD) is used to generate structural information about crystalline samples. It provides a characteristic profile of the substance, like a fingerprint, and is ideally suited for characterization and identification of

polycrystalline phases.[40] It is frequently used to characterize materials containing nano-

sized components embedded in an extended biological matrix, such as those found in

tissue scaffolds and bone cements.[41] In some cases, XRD is used to characterize a

biomolecule after it has been associated with the nanomaterials (NM).[42]

Microscopy Techniques

Electron Microscopy.   Microscopy techniques are based on visualizing a sample

using electrons or a scanning probe. Transmission electron microscopy (TEM) and

Scanning electron microscopy (SEM) readily obtain single particle resolution and are

more frequently applied to characterizing the NM core along with core shell size and or

structure. The direct imaging capability of the TEM and SEM is particularly useful for

nanomaterials with non-spherical shapes allowing a direct measure of the aspect ratio.[43]

TEM is more commonly used to image the core. Although dried samples are typically

required for TEM analysis, some groups have imaged liquid samples of fixed fibroblast

cells stained with epidermal growth factor labeled AuNPs.[44] SEM has less resolving

power for features less than 20 nm although the technology is steadily improving even in

this area.[45,46,47]

Atomic Force Microscopy. In contrast to TEM and SEM, atomic force

microscopy (AFM) is a scanning probe technique. This technique provides a range of

information about the nanomaterials and the NM-biomolecule interactions on a single-

particle basis. AFM was once considered a specialized technique but most recent

advances in both instrumentation and software have only expanded the technique's

capabilities. Unlike TEM and SEM which are best performed with conducting or

semiconducting samples under vacuum conditions, AFM can be applied to nonconductive, wet and soft samples. This allows for many different types of materials to be analyzed.48 AFM could potentially allow for a 3D representation of ligands attached to a nanoparticle surface, as was shown to be particularly useful in characterizing DNA derived nanostructures[.49,10a]

Near Field Scanning Optical Microscopy. Another surface probe microscopy technique, near-field scanning optical microscopy breaks the optical resolution limit of light microscopy by placing the detection probe at distances smaller than the wavelength of light. High frequency spatial and spectral information is obtained by analyzing the evanescent fields close to the sample surface. This technique has the advantage of combining optical and or spectroscopic data with high-resolution surface topographical information. This technique allows the contrast mechanism to be easily adapted to study properties such as structure and stress. Dynamic properties can also be studied at a sub-wavelength level using this technique.[50]

Spectroscopy

UV-Visible Spectroscopy. Spectroscopic techniques exploit the interaction of electromagnetic radiation with a sample material resulting in the wavelength dependent absorption and, in the case of fluorescence, re-emission of photons. Typically, a wavelength dependent spectrum is produced with characteristic absorption/emission peaks inherent to the sample.51 The UV-visible absorbance properties of nanomaterials can be used to monitor important properties such as concentration, size and aggregation state. Metal nanoparticles especially the gold and silver exhibit a strong absorption in the

visible region known as the surface Plasmon resonance (SPR) band. The SPR band is dependent on a number of factors and is found to be sensitive to size, shape and composition.[52,53] Both direct and in-direct analysis of UV-visible spectroscopy data can also provide information on the NM-bioconjugate. Direct characterization is possible when the biomolecule has a distinct UV-visible profile that remains discernible upon conjugation to the NM.

Fluorescence Spectroscopy. Fluorescence occurs when an orbital electron of an atom or nanostructure relaxes to its ground state by releasing a photon after being exited to a higher quantum state by some type of energy. The fluorescence spectroscopy technique offers a powerful and sensitive technique for determining a number of parameters associated with the immobilization of biomolecules to a NM surface including fluorophore local environment, biomolecule-NM coupling ratio, conformational state and in some instances intra-assembly molecular distances.[54] A number of researchers use the intrinsic fluorescence from tryptophan (Trp) residues to obtain information about local changes in tertiary structure upon nanoparticle binding.[55,56]

Infrared Spectroscopy. Infrared (IR) Spectroscopy measures the absorption of IR radiation by a sample resulting from the vibrational stretching and bending modes within the molecule. Fourier Transform (FT)-IR was used to characterize peptide and protein binding to nanoparticles.[57,58,59] Careful interpretation of the stretching and bending vibrations in the amide regions can provide secondary structural information and hence the conformational state of the bound protein.

Molecular Modeling

Molecular modeling, though not considered a classical nanoparticle tool, can provide important insight into the structure and function of nanoparticles and their bioconjugates. The overall goal of any modeling effort is to gain insight into properties or behavior of a system that cannot be directly observed. Although not fully extended to nanomaterials *per se*, predictive modeling can clearly aid in the characterization and understanding of these materials. This was demonstrated by Saunders and co-workers who applied a total interaction energy model to accurately predict the size distribution of size-selectively precipitated nanoparticles. These studies showed that modeling is helpful in estimating parameters such as nanoparticle size.[60,61]

Table 1.4 Advantages and disadvantages of nanoparticle characterization techniques.[62]

Technique	Advantages	Disadvantages
Scattering Techniques		
Dynamic Light Scattering (DLS)	1. Provides a distribution of NP size. 2. Hydrodynamic radius is provided.	1. Limited to low concentrations 2. Optimization of the scan parameters is often required.
Raman Techniques	1. Highly specific even with small volumes of sample. 2. No interference from water.	1. The detection needs a sensitive and highly optimized instrumentation. 2. Sample heating can destroy the sample or cover the Raman spectrum.
X-ray Diffraction	1. Simple sample preparation. 2. Measurements can be taken rapidly.	1. Large crystal samples are hard to scan. 2. Single crystals are hard to obtain.
Microscopy Techniques		
Electron Microscopy	1. Can analyze individual NMs, can be used to determine NM size and shapes. 2. Can determine NM composition.	1. Conducting sample usually required. 2. Dry samples needed for analysis. 3. Mainly used to characterize NP core.
Atomic Force Microscopy (AFM)	1. Size and shape characterization of the NM and biomolecule can be determined. 2. Biomolecular interactions can be characterized using functionalized tips.	1. Only small area can be mapped and the can time can be slowed. 2. Analysis is, in general, limitation to the NP exterior.
Near Field Scanning Optical Microscopy	1. High resolution surface analysis at ambient conditions. 2. Contrast techniques with optical microscopy may also be applied for high resolution analysis.	1. Small surface are analyzed. 2. Analysis limited to the surface of the NP. 3. Currently a "specialist" technique.
Spectroscopy Techniques		
UV-Vis Absorbance Spectroscopy	1. Cost effective 2. Can determine concentration, size and sometimes shape.	1. Requires fairly concentrated samples as sensitivity is low. 2. Provides average information only no distribution information.
Fluorescence Spectroscopy	1. Fluorescence can be environmentally sensitive which can be used to provide biomolecule conformational information or confirm attachment to NM.	1. Intrinsic or extrinsic fluorescence required which may necessitate labeling.
Infrared Spectroscopy	1. Confirms NM-biomolecule attachment through the appearance of characteristic fingerprint IR bands.	1. Sample preparation can be complicated. 2. H_2O is an interference, strong absorbance

Gold Nanoparticles for Drug Delivery

Nanomaterials are showing a great promise as adjuvants to chemotherapeutics. It is believed that the reason nanomaterials are currently explored for a pharmacological purpose is due to their unique pharmacokinetic and pharmacodynamic properties. Some nanomaterials of major clinical interest are AuNPs and nanomaterial based surfactants. Nanoparticles can be used as drug carriers that increase both drug potency and targeting.[63]

AuNPs can be prepared surrounded by an organic monolayer which allows for the conjugation of targeting ligands and drugs.[64] As such, AuNPs can be synthesized to increase the pharmacokinetic characteristics of a particular drug. AuNPs also contain unique photochemical characteristics that may allow for the controlled physical manipulation of their shape and size for managed site specific effects.[65] For example, it was shown that upon near-infrared laser radiation of engineered AuNP drug capsules, there was an alteration in the particle shape allowing for drug release at a specific site.[66]

Triblock Copolymers and Drug Delivery

Nonionic triblock copolymers, being a class of nanomaterials, working in a similar way to liposomes, are able to act as drug carriers improving pharmacokinetics and biodistribution of particular drugs.[67] They are a class of self-associating, amphiphilic, pluronics (PL) with hydrophilic ethylene oxide (EO) and hydrophobic propylene oxide (PO) blocks. Like the other nanomaterials these pluronics can be functionalized to improve their target efficacy. In polar solvents, they self-associate into micelles at particular concentrations based on their engineered chain composition and length,

defining the degree of their amphiphilicity. As a result of this amphiphilicity the polymer self-associates into micelles, which contain both a hydrophilic and hydrophobic region, in a concentration dependent manner. The concentration at which this occurs is called the critical micelle concentration (CMC). This unique characteristic has been utilized recently in order to solubilize and transport hydrophobic drug within the hydrophobic core of the PL micelles.

Nonionic triblock copolymers in combination with their cargo drugs are believed to alter the microviscosity of tumor membranes and their surrounding vasculature rendering these pluronics of increasing interest in chemotherapeutics.[68] Given that membrane protein stability and conformation are largely dependent on membrane integrity, the features of nonionic triblock copolymers may possibly be used to alter membrane protein function. In addition, these triblock copolymers are known to have exceptional stability against oxidation and can play a significant role in the advancement of clinically useful diagnostic and therapeutic nanomedicines.[5]

Shape and Size Control in Gold Nanoparticles

Gold nanoparticles are intensively studied due to their shape and size dependent physicochemical properties with useful applications in biomedicine and other fields. In the past decade the chemists sought to understand the shape and size control of nanoparticles through various strategies. It continues to be the focus of research in nanotechnology today. Citrate-stabilized gold nanoparticles with up to 200 nanometer size distributions were synthesized.[69] These gold nanoparticles exhibited uniform quasi-

spherical shapes as they were prepared through kinetically controlled seeded growth strategies through the reduction of tetrachlorohydroauric acid by sodium citrate.

One of the major difficulties encountered during production of nanoparticles with respect to their shape and size is the poor quality of the product. The shapes and sizes of the nanoparticles obtained are generally irregular and non-uniform. Some minor progress in this regard was noted in recent years. For example, the seeded growth of AuNPs using sodium citrate hydroxylamine to obtain nanoparticles smaller than 100 nm in diameter were attempted by the Natan *et. al.*[70,71,72] Although this was an improvement over the past syntheses, it was not free from secondary populations of rod-shaped particles. Murphy *et. al.*[73] and Marzan *et. al.*[74] further improved this and reported the synthesis of monodisperse AuNPs of up to 180 nm in diameter using ascorbic acid as a reducing agent and cetyltrimethyl Ammonium bromide (CTAB) as a cationic surfactant. These methods allow some limited control but the choices of the reagents create environmental hazards and pose possible restrictions to further functionalization.[75, 76] The development of new AuNP synthetic strategies with environmentally friendly reagents leading to monodispersity of the shape and size specificities continues to challenge the research community.

Scope of the Research

The goal of this proposed research is to increase the mechanistic understanding of nucleation and growth of gold nanoparticles (Au NPs) from tetrachloroauric (III) acid ($HAuCl_4$) via a "one-pot" approach using triblock non-ionic block copolymers (TBPs) of poly (ethylene oxide) (PEO) and poly (propylene oxide) (PPO) PEO-PPO-PEO.
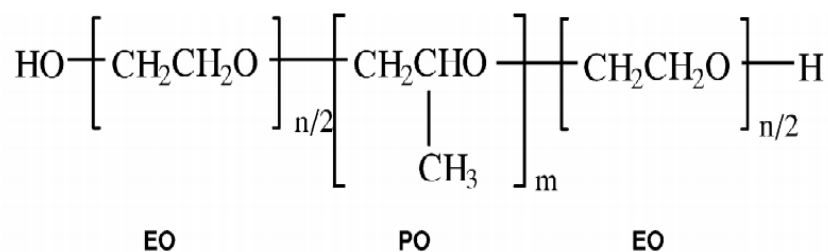
Figure 1.4 Monomer units of triblock copolymers (TBPs).

The central hypothesis is that Au NP morphology and size can be adjusted by the TBP/Au (III) ratio. This is based upon two premises: (1) the hydrophobic/hydrophilic environment can be regulated via the hydrophobic TBP L31 to control the reaction kinetics; (2) kinetic models of AuNP formation and growth are used as predictive tools for rational Au NP synthesis. Non-ionic coated Au NPs are synthesized by tetrachloroauric (III) acid ($HAuCl_4$) reduction by the EO_x blocks in a L31 (EO_2-PO_{16}-EO_2) /F68 (EO_{78}-PO_{30}-EO_{78}) aqueous solution. Au NP size and shape are characterized by using (a) atomic force microscopy (AFM), (b) dynamic light scattering (DLS) (c) ultraviolet-visible (UV-vis) spectroscopy and (d) Field emission scanning electron microscopy (FESEM). In the seeding methodology Au NPs are present initially in the precursor solutions. The kinetic control of the reaction is achieved by varying the TBP/Au (III) ratio and the Au NP shape and size optimized by varying the parameters of TBP/Au ratio and citrated AuNP seed size and concentration. Our *central hypothesis* is that the variation in TBP/Au ratio and seed concentration will change Au NP size and shape. In this thesis we test this hypothesis by changing the parameters of the TBP/Au ratio, and the citrate coated Au NP seed size and concentration.

References

1. Love, J. C.; Estroff, L. A.; Kriebel, J. K.; Nuzzo, R. G.; Whitesides, G. M., Self-Assembled Monolayers of Thiolates on Metals as a Form of Nanotechnology. *Chem. Rev.* **2005,** *105*, 1103-1169.

2. Kelly, K. L.; Coronado, E.; Zhao, L. L.; Schatz, G. C., The Optical Properties of Metal Nanoparticles: The Influence of Size, Shape, and Dielectric Environment. *J. Phys. Chem. B* **2003,** *107* (3), 668-677.

3. NASA http://www.ipt.arc.nasa.gov/nanotechnology.html.

4. Lee, Y.; Graeser, R.; Kratz, F.; Geckeler, K. E., Drug Delivery: Paclitaxel-Loaded Polymer Nanoparticles for the Reversal of Multidrug Resistance in Breast Cancer Cells. *Adv. Funct. Mater.* **2011,** *21* (22), 4201-4201.

5. Prasad, S. K., *Modern Concepts In Nanotechnology*. Discovery Publishing House Pvt. Limited: 2008.

6. Hiralal, P.; Unalan, H. E.; Amaratunga, G. A. J., Nanowires for energy generation. *Nanotechnology* **2012,** *23* (19), 194002.

7. Kroto, H. W.; Heath, J. R.; O'Brien, S. C.; Curl, R. F.; Smalley, R. E., C60: Buckminsterfullerene. *Nature* **1985,** *318* (6042), 162-163.

8. Watson, J. D.; Berry, A., *DNA: The Secret of Life*. Alfred A. Knopf: 2004.

9. *Nanoscience and Nanotechnologies: Opportunities and Uncertainties*. The Royal Society: 2004.

10. (a) Rana, S.; Bajaj, A.; Mout, R.; Rotello, V. M., Monolayer coated gold nanoparticles for delivery applications. *Adv. Drug Delivery Rev.* **2012,** *64* (2), 200-216; (b) Mora-Huertas, C. E.; Fessi, H.; Elaissari, A., Polymer-based nanocapsules for drug delivery. *Int. J. Pharm.* **2010,** *385* (1–2), 113-142.

11. Daniel, M.-C.; Autruc, D., Gold nanoparticles: assembly, supramolecular chemistry, quantum-size-related properties, and applications toward biology, catalysis, and nanotechnology. *Chem. Rev. (Washington, DC, U. S.)* **2004,** *104* (1), 293.

12. Rao, D. D.; Vorhies, J. S.; Senzer, N.; Nemunaitis, J., siRNA vs. shRNA: Similarities and differences. *Adv. Drug Delivery Rev.* **2009,** *61* (9), 746-759.

13. Fahlman, B. D., Nanomaterials Materials Chemistry. Springer Netherlands: 2011; pp 457-583.

14. Fahlman, B. D., *Materials Chemistry (2nd Ed)*. Springer: New York, 2011.

15. (a) Jain, P. K.; Huang, X.; El-Sayed, I. H.; El-Sayed, M. A., Noble Metals on the Nanoscale: Optical and Photothermal Properties and Some Applications in Imaging, Sensing, Biology, and Medicine. *Acc. Chem. Res.* **2008,** *41* (12), 1578-1586; (b) Link, S.; El-Sayed, M. A., Size and temperature dependence of the plasmon absorption of colloidal gold nanoparticles. *J. Phys. Chem. B* **1999,** *103* (21), 4212-4217.

16. (a) Link, S.; El-Sayed, M. A., Spectral Properties and Relaxation Dynamics of Surface Plasmon Electronic Oscillations in Gold and Silver Nanodots and Nanorods. *J. Phys. Chem. B* **1999,** *103* (40), 8410-8426; (b) Lee, K. S.; El-Sayed, M. A., Gold and Silver Nanoparticles in Sensing and Imaging: Sensitivity of Plasmon Response to Size, Shape, and Metal Composition. *J. Phys. Chem. B* **2006,** *110* (39), 19220-19225.

17. Alivisatos, A. P., Semiconductor Clusters, Nanocrystals, and Quantum Dots. *Science* **1996,** *271* (5251), 933-937.

18. (a) Yang, W.-H.; Schatz, G. C.; Van Duyne, R. P., Discrete dipole approximation for calculating extinction and Raman intensities for small particles with arbitrary shapes. *J. Chem. Phys.* **1995,** *103* (3), 869; (b) Draine, B. T.; Flatau, P. J., The discrete dipole approximation for periodic targets: theory and tests. *J. Opt. Soc. Am. A* **2008,** *25*, 2693-2703.

19. Kiss, L. B.; Söderlund, J.; Niklasson, G. A.; Granqvist, C. G., New approach to the origin of lognormal size distributions of nanoparticles. *Nanotechnology* **1999,** *10* (1), 25.

20. (a) Pricker, S., Medical uses of gold compounds: Past, present and future. *Gold Bull.* **1996,** *29* (2), 53-60; (b) Thakor, A. S.; Jokerst, J.; Zavaleta, C.; Massoud, T. F.; Gambhir, S. S., Gold Nanoparticles: A Revival in Precious Metal Administration to Patients. *Nano Lett.* **2011,** *11* (10), 4029-4036.

21. Dykman, L.; Khlebtsov, N., Gold nanoparticles in biomedical applications: recent advances and perspectives. *Chem. Soc. Rev.* **2012,** *41* (6), 2256-2282.

22. Arvizo, R.; Bhattacharya, R.; Mukherjee, P., Gold nanoparticles: opportunities and challenges in nanomedicine. *Expert Opin. Drug Deliv.* **2010,** *7* (6), 753-763.

23. (a) Jain, P. K.; Lee, K. S.; El-Sayed, I. H.; El-Sayed, M. A., Calculated Absorption and Scattering Properties of Gold Nanoparticles of Different Size, Shape, and Composition: Applications in Biological Imaging and Biomedicine. *J. Phys. Chem. B* **2006,** *110* (14), 7238-7248; (b) Li, J.-L.; Wang, L.; Liu, X.-Y.; Zhang, Z.-P.; Guo, H.-C.; Liu, W.-M.; Tang, S.-H., In vitro cancer cell imaging and therapy using transferrin-conjugated gold nanoparticles. *Cancer Lett.* **2009,** *274* (2), 319-326.

24. Kunkely, H.; Vogler, A., Photooxidation of dichloro- and dibromoaurate(1-) induced by ds excitation. *Inorg. Chem.* **1992,** *31* (22), 4539-4541.

25. (a) Mason, W. R.; Gray, H. B., Electronic structures of square-planar complexes. *J. Am. Chem. Soc.* **1968,** *90* (21), 5721-5729; (b) Koutek, M. E.; Mason, W. R., Electronic structure and spectra of linear dihaloaurate(I) ions. *Inorg. Chem.* **1980,** *19* (3), 648-653; (c) Isci, H.; Mason, W. R., Ligand-to-metal charge-transfer spectra of tetrahaloaurate(III) and trans-dicyanodihaloaurate(III) ions. *Inorg. Chem.* **1983,** *22* (16), 2266-2272.

26. Chen, H. M.; Liu, R.-S., Architecture of Metallic Nanostructures: Synthesis Strategy and Specific Applications. *J. Phys. Chem. C* **2011,** *115* (9), 3513-3527.

27. Shenhar, R.; Rotello, V. M., Nanoparticles: Scaffolds and Building Blocks. *Acc. Chem. Res.* **2003,** *36* (7), 549-561.

28. Nikoobakht, B.; El-Sayed, M. A., Surface-Enhanced Raman Scattering Studies on Aggregated Gold Nanorods. *J. Phys. Chem. A* **2003,** *107* (18), 3372-3378.

29. Huang, X.; Jain, P.; El-Sayed, I.; El-Sayed, M., Plasmonic photothermal therapy (PPTT) using gold nanoparticles. *Lasers Med. Sci.* **2008,** *23* (3), 217-228.

30. Daniel, M.-C.; Astruc, D., Gold Nanoparticles: Assembly, Supramolecular Chemistry, Quantum-Size-Related Properties, and Applications toward Biology, Catalysis, and Nanotechnology. *Chem. Rev.* **2004,** *104* (1), 293-346.

31. Turkevich, J.; Stevenson, P. C.; Hillier, J., A study of the nucleation and growth processes in the synthesis of colloidal gold. *Discuss. Faraday Soc.* **1951,** *11*, 55-75.

32. (a) Frens, G., Particle size and sol stability in metal colloids. *Colloid Polym. Sci.* **1972,** *250* (7), 736-741; (b) Frens, G., Controlled Nucleation for the Regulation of the Particle Size in Monodisperse Gold Suspensions. *Nature Physical Science* **1973,** *241*, 20-22.

33. Malikova, N.; Pastoriza-Santos, I.; Schierhorn, M.; Kotov, N. A.; Liz-Marzán, L. M., Layer-by-Layer Assembled Mixed Spherical and Planar Gold Nanoparticles: Control of Interparticle Interactions. *Langmuir* **2002,** *18* (9), 3694-3697.

34. Tan, Y. N.; Lee, J. Y.; Wang, D. I. C., Aspartic Acid Synthesis of Crystalline Gold Nanoplates, Nanoribbons, and Nanowires in Aqueous Solutions. *J. Phys. Chem. C* **2008,** *112* (14), 5463-5470.

35. Kim, J.-U.; Cha, S.-H.; Shin, K.; Jho, J. Y.; Lee, J.-C., Preparation of Gold Nanowires and Nanosheets in Bulk Block Copolymer Phases under Mild Conditions. *Adv. Mater.* **2004,** *16* (5), 459-464.

36. Biswal, J.; Ramnani, S. P.; Shirolikar, S.; Sabharwal, S., Synthesis of rectangular plate like gold nanoparticles by in situ generation of seeds by combining both radiation and chemical methods. *Radiat. Phys. Chem.* **2011,** *80* (1), 44-49.

37. Murdock, R. C.; Braydich-Stolle, L.; Schrand, A. M.; Schlager, J. J.; Hussain, S. M., Characterization of Nanomaterial Dispersion in Solution Prior to In Vitro Exposure Using Dynamic Light Scattering Technique. *Toxicol. Sci.* **2008,** *101* (2), 239-253.

38. Liu, Z.; Li, X.; Tabakman, S. M.; Jiang, K.; Fan, S.; Dai, H., Multiplexed Multicolor Raman Imaging of Live Cells with Isotopically Modified Single Walled Carbon Nanotubes. *J. Am. Chem. Soc.* **2008,** *130* (41), 13540-13541.

39. Yang, Q.; Shuai, L.; Zhou, J.; Lu, F.; Pan, X., Functionalization of Multiwalled Carbon Nanotubes by Pyrene-Labeled Hydroxypropyl Cellulose. *J. Phys. Chem. B* **2008,** *112* (41), 12934-12939.

40. Fahlman, B. D., Materials Characterization Materials Chemistry. Springer Netherlands: 2011; pp 585-667.

41. Fu, Q.; Zhou, N.; Huang, W.; Wang, D.; Zhang, L.; Li, H., Effects of nano HAP on biological and structural properties of glass bone cement. *Journal of Biomedical Materials Research Part A* **2005,** *74A* (2), 156-163.

42. Castelletto, V.; Newby, G. E.; Zhu, Z.; Hamley, I. W.; Noirez, L., Self-Assembly of PEGylated Peptide Conjugates Containing a Modified Amyloid β-Peptide Fragment. *Langmuir* **2010,** *26* (12), 9986-9996.

43. Tom, R. T.; Samal, A. K.; Sreeprasad, T. S.; Pradeep, T., Hemoprotein Bioconjugates of Gold and Silver Nanoparticles and Gold Nanorods: Structure−Function Correlations. *Langmuir* **2006,** *23* (3), 1320-1325.

44. Jonge, N. d.; Peckys, D. B.; Kremers, G. J.; Piston, D. W., Electron microscopy of whole cells in liquid with nanometer resolution. *Proc. Natl. Acad. Sci. U. S. A.* **2009,** *106* (7), 2159-2164.

45. Smith, J. E.; Wang, L.; Tan, W., Bioconjugated silica-coated nanoparticles for bioseparation and bioanalysis. *TrAC Trends in Analytical Chemistry* **2006,** *25* (9), 848-855.

46. Rayavarapu, R. G.; Petersen, W.; Ungureanu, C.; Post, J. N.; van Leeuwen, T. G.; Manohar, S., Synthesis and Bioconjugation of Gold Nanoparticles as Potential Molecular Probes for Light-Based Imaging Techniques. *International Journal of Biomedical Imaging* **2007,** *2007*.

47. Skrabalak, S. E.; Chen, J.; Sun, Y.; Lu, X.; Au, L.; Cobley, C. M.; Xia, Y., Gold Nanocages: Synthesis, Properties, and Applications. *Acc. Chem. Res.* **2008,** *41* (12), 1587-1595.

48. Midgley, P. A.; Durkan, C., The frontiers of microscopy. *Materials Today* **2008,** *11, Supplement* (0), 8-11.

49. Kuzuya, A.; Komiyama, M., DNA origami: Fold, stick, and beyond. *Nanoscale* **2010,** *2* (3), 310-322.

50. Park, H. K.; Lim, Y. T.; Kim, J. K.; Park, H. G.; Chung, B. H., Nanoscopic observation of a gold nanoparticle-conjugated protein using near-field scanning optical microscopy. *Ultramicroscopy* **2008,** *108* (10), 1115-1119.

51. Pavia, D. L., *Introduction to Spectroscopy*. Brooks/Cole, Cengage Learning: 2009.

52. Schwartzberg, A. M.; Zhang, J. Z., Novel Optical Properties and Emerging Applications of Metal Nanostructures. *J. Phys. Chem. C* **2008,** *112* (28), 10323-10337.

53. Amendola, V.; Meneghetti, M., Size Evaluation of Gold Nanoparticles by UV−vis Spectroscopy. *J. Phys. Chem. C* **2009,** *113* (11), 4277-4285.

54. Lakowicz, J. R., *Principles of Fluorescence Spectroscopy*. Springer: 2006.

55. Wu, X.; Narsimhan, G., Characterization of Secondary and Tertiary Conformational Changes of β-Lactoglobulin Adsorbed on Silica Nanoparticle Surfaces. *Langmuir* **2008,** *24* (9), 4989-4998.

56. Shang, L.; Wang, Y.; Jiang, J.; Dong, S., pH-Dependent Protein Conformational Changes in Albumin:Gold Nanoparticle Bioconjugates: A Spectroscopic Study. *Langmuir* **2007,** *23* (5), 2714-2721.

57. Jiang, X.; Jiang, J.; Jin, Y.; Wang, E.; Dong, S., Effect of Colloidal Gold Size on the Conformational Changes of Adsorbed Cytochrome c: Probing by Circular Dichroism, UV−Visible, and Infrared Spectroscopy. *Biomacromolecules* **2004,** *6* (1), 46-53.

58. Perevedentseva, E.; Cai, P. J.; Chiu, Y. C.; Cheng, C. L., Characterizing Protein Activities on the Lysozyme and Nanodiamond Complex Prepared for Bio Applications. *Langmuir* **2010,** *27* (3), 1085-1091.

59. Krpetić, Z. e.; Nativo, P.; Porta, F.; Brust, M., A Multidentate Peptide for Stabilization and Facile Bioconjugation of Gold Nanoparticles. *Bioconjugate Chem.* **2009,** *20* (3), 619-624.

60. Kim, Y.; Klutz, A.; Hechler, B.; Gao, Z.-G.; Gachet, C.; Jacobson, K., Application of the functionalized congener approach to dendrimer-based signaling agents acting through adenosine receptors. *Purinergic Signalling* **2009,** *5* (1), 39-50.

61. Prasuhn, D. E.; Deschamps, J. R.; Susumu, K.; Stewart, M. H.; Boeneman, K.; Blanco-Canosa, J. B.; Dawson, P. E.; Medintz, I. L., Polyvalent Display and Packing of Peptides and Proteins on Semiconductor Quantum Dots: Predicted Versus Experimental Results. *Small* **2010,** *6* (4), 555-564.

62. Sapsford, K. E.; Tyner, K. M.; Dair, B. J.; Deschamps, J. R.; Medintz, I. L., Analyzing Nanomaterial Bioconjugates: A Review of Current and Emerging Purification and Characterization Techniques. *Anal. Chem.* **2011,** *83* (12), 4453-4488.

63. Kattumuri, V.; Katti, K.; Bhaskaran, S.; Boote, E. J.; Casteel, S. W.; Fent, G. M.; Robertson, D. J.; Chandrasekhar, M.; Kannan, R.; Katti, K. V., Gum Arabic as a Phytochemical Construct for the Stabilization of Gold Nanoparticles: In Vivo Pharmacokinetics and X-ray-Contrast-Imaging Studies. *Small* **2007,** *3* (2), 333-341.

64. (a) Chan, W. C. W., *Bio-Applications Of Nanoparticles*. Springer Science + Business Media: 2007; (b) Connor, E. E.; Mwamuka, J.; Gole, A.; Murphy, C. J.; Wyatt, M. D., Gold Nanoparticles Are Taken Up by Human Cells but Do Not Cause Acute Cytotoxicity. *Small* **2005,** *1* (3), 325-327; (c) Verma, A.; Rotello, V. M., Surface recognition of biomacromolecules using nanoparticle receptors. *Chem. Commun.* **2005,** (3), 303-312.

65. Pissuwan, D.; Valenzuela, S. M.; Cortie, M. B., Therapeutic possibilities of plasmonically heated gold nanoparticles. *Trends Biotechnol.* **2006,** *24* (2), 62-67.

66. Skirtach, A. G.; Muñoz Javier, A.; Kreft, O.; Köhler, K.; Piera Alberola, A.; Möhwald, H.; Parak, W. J.; Sukhorukov, G. B., Laser-Induced Release of Encapsulated Materials inside Living Cells. *Angew. Chem., Int. Ed. Engl.* **2006,** *45* (28), 4612-4617.

67. (a) Drummond, D. C.; Meyer, O.; Hong, K.; Kirpotin, D. B.; Papahadjopoulos, D., Optimizing Liposomes for Delivery of Chemotherapeutic Agents to Solid Tumors. *Pharmacol. Rev.* **1999,** *51* (4), 691-744; (b) Batrakova, E. V.; Kabanov, A. V., Pluronic block copolymers: Evolution of drug delivery concept from inert nanocarriers to biological response modifiers. *Journal of Controlled Release* **2008,** *130* (2), 98-106.

68. (a) Batrakova, E. V.; Kabanov, A. V., Pluronic block copolymers: Evolution of drug delivery concept from inert nanocarriers to biological response modifiers. *J. Controlled Rel.* **2008,** *130* (2), 98-106; (b) Batrakova, E. V.; Li, S.; Alakhov, V. Y.; Miller, D. W.; Kabanov, A. V., Optimal Structure Requirements for Pluronic Block Copolymers in Modifying P-glycoprotein Drug Efflux Transporter Activity in

Bovine Brain Microvessel Endothelial Cells. *J. Pharmacol. Exp. Ther.* **2003,** *304* (2), 845-854; (c) Batrakova, E. V.; Li, S.; Li, Y.; Alakhov, V. Y.; Elmquist, W. F.; Kabanov, A. V., Distribution kinetics of a micelle-forming block copolymer Pluronic P85. *J. Controlled Release* **2004,** *100* (3), 389-397; (d) Kabanov, A. V.; Batrakova, E. V.; Alakhov, V. Y., Pluronic® block copolymers for overcoming drug resistance in cancer. *Adv. Drug Deliv. Rev.* **2002,** *54* (5), 759-779.

69.   Bastús, N. G.; Comenge, J.; Puntes, V. c., Kinetically Controlled Seeded Growth Synthesis of Citrate-Stabilized Gold Nanoparticles of up to 200 nm: Size Focusing versus Ostwald Ripening. *Langmuir* **2011,** *27* (17), 11098-11105.

70.   Brown, K. R.; Walter, D. G.; Natan, M. J., Seeding of Colloidal Au Nanoparticle Solutions. 2. Improved Control of Particle Size and Shape. *Chem. Mater.* **1999,** *12* (2), 306-313.

71.   Brown, K. R.; Lyon, L. A.; Fox, A. P.; Reiss, B. D.; Natan, M. J., Hydroxylamine Seeding of Colloidal Au Nanoparticles. 3. Controlled Formation of Conductive Au Films. *Chem. Mater.* **1999,** *12* (2), 314-323.

72.   Brown, K. R.; Natan, M. J., Hydroxylamine Seeding of Colloidal Au Nanoparticles in Solution and on Surfaces. *Langmuir* **1998,** *14* (4), 726-728.

73.   (a) Sau, T. K.; Murphy, C. J., Seeded High Yield Synthesis of Short Au Nanorods in Aqueous Solution. *Langmuir* **2004,** *20* (15), 6414-6420; (b) Murphy, C. J.; Sau, T. K.; Gole, A. M.; Orendorff, C. J.; Gao, J.; Gou, L.; Hunyadi, S. E.; Li, T., Anisotropic Metal Nanoparticles: Synthesis, Assembly, and Optical Applications. *J. Phys. Chem. B* **2005,** *109* (29), 13857-13870; (c) Jana, N. R.; Gearheart, L.; Murphy, C. J., Wet chemical synthesis of silver nanorods and nanowires of controllable aspect ratio *Chem. Commun.* **2001**, 617 - 618.

74.   (a) Liz-Marzán, L. M., Tailoring Surface Plasmons through the Morphology and Assembly of Metal Nanoparticles. *Langmuir* **2006,** *22* (1), 32-41; (b) Abalde-Cela, S.; Aldeanueva-Potel, P.; Mateo-Mateo, C.; Rodríguez-Lorenzo, L.; Alvarez-Puebla, R. A.; Liz-Marzán, L. M., Surface-enhanced Raman scattering biomedical applications of plasmonic colloidal particles. *J. Royal Soc. Interface* **2010,** *7* (Suppl 4), S435-S450.

75.   Jana, N. R.; Gearheart, L.; Murphy, C. J., Seeding Growth for Size Control of 5−40 nm Diameter Gold Nanoparticles. *Langmuir* **2001,** *17* (22), 6782-6786.

76.   Rodríguez-Fernández, J.; Pérez-Juste, J.; García de Abajo, F. J.; Liz-Marzán, L. M., Seeded Growth of Submicron Au Colloids with Quadrupole Plasmon Resonance Modes. *Langmuir* **2006,** *22* (16), 7007-7010.

CHAPTER TWO

FLUORESCENCE OF COMMERCIAL PLURONIC F127

SAMPLES: TEMPERATURE DEPENDENT MICELLIZATION

Abstract

We present a novel approach of using the butylated hydroxytoluene (BHT)

antioxidant found in commercial Pluronic F127 samples as a marker of polymer

aggregation. The BHT marker was compared to the pyrene dye and static light scattering

methods as a way to measure the critical micelle concentration (CMC) and critical

micelle temperature (CMT). The n→π* transitions of BHT are sensitive to the

microenvironment as demonstrated by plotting the fractional intensities of its excitation

($\approx$ 280 nm) and emission ($\approx$ 325 nm) peaks. BHT is more sensitive to changes in

temperature than concentration. The partition coefficient increases $\approx$ 40-fold for pyrene

compared to $\approx$ 2 fold for BHT when the temperature is increased from 25 to 37 °C. CMT

values determined using the BHT fluorescence decrease with increasing F127

concentration. Our results show that BHT can be used as a reliable marker of changes in

the microenvironment of Pluronic F127.

Abbreviations

AFM	Atomic force microscopy
BHT	Butylated hydroxytoluene
CMC	Critical micelle concentration
CMT	Critical micelle temperature
DLS	Dynamic light scattering
ESR	Electron spin resonance
FTIR	Fourier transform infrared spectroscopy
PEO	Poly ethylene oxide
PPO	Poly propylene oxide
NMR	Nuclear magnetic resonance
SANS	Small angle neutron scattering
TEM	Transmission electron microscopy

Introduction

Triblock non-ionic copolymers of poly (ethylene oxide) (PEO) and poly (propylene oxide) (PPO) are produced either in the sequence PEO-PPO-PEO or PPO-PEO-PPO and are known commercially as Pluronics or Poloxamers. Pluronics have been shown to have beneficial synergistic properties in combination with anti-cancer drugs.[1] Finding a reliable way to measure the critical micelle concentration (CMC), critical micelle temperature (CMT), and drug partitioning between aqueous and micelle phases are of particular significance to the optimization of pharmaceutical formulations using Pluronic copolymers.[2] In particular, Pluronic F127 or Poloxamer 407 has received much attention because of its unique thermo-reversible gelation properties that has found numerous pharmaceutical applications.[1d, 3] Pluronics are used increasingly as components in building novel nanomaterials, and therefore the intensive study of the physico-chemical properties of Pluronics is relevant for constructing well-defined nanomaterials that can be used as building blocks for more complex molecular architectures.

Aspects of the structural and dynamic properties of micellar self-assembly of the PEO-PPO-PEO block copolymers have been investigated by a variety of experimental methods, including fluorescence spectroscopy,[2, 4] differential scanning calorimetry,[5] transmission electron microscopy (TEM),[6] viscometry,[7] light scattering,[8] nuclear magnetic resonance (NMR),[9] UV-vis absorption of selected probes,[10] surface tension,[11] electron spin resonance (ESR),[12] small angle neutron scattering (SANS),[6a, 13] Fourier transform infrared spectroscopy (FTIR),[14] and Raman spectroscopy.[15] At room temperature (RT) both the PEO and the PPO blocks of the Pluronic F127 are hydrophilic and water soluble forming a transparent solution. The triblock copolymers exist as

unimers solvated by water molecules. Spectroscopic analysis by ^{1}H NMR, Fluorescence and FTIR revealed that the hydrophobic PPO portion of the Pluronic polymers is important in the temperature-induced micellization,[14] whereas the transitional behavior of Pluronic polymers, from micellization to liquid crystal formation, is affected by the PEO segments.[16]

Simulations using the mean-field lattice[17] and the more sophisticated dynamic mean field density functional theories[18] have been used to model Pluronic polymer reorganization. In mean-field lattice theory, the conformation of the polymer chains exists in two forms: a polar one, and non-polar one. The polymer segments are allowed to assume both polar and non-polar conformations (corresponding to the *gauche* and *trans* rotations of the C-C and C-O bonds).[17] The polar form allows significant interactions with the water solvent, whereas the non-polar one denotes poor solvent-solute interactions and contraction of the polymer chains. Relative to increasing temperature, there is qualitative agreement between theory and experiment for Pluronic F127 regarding the decrease in the CMC, its increase in aggregation number, the micellar size, and the fraction of polymer molecules in micellar form. The more sophisticated dynamic mean field density functional calculations of Pluronic F127 by Lam and Wood[19] reproduced experimental observations of increasing micellar sizes with concentration consistent with previous cryo-TEM observations.[6] Simulations by Yang *et al.*[20] of Pluronic F103 have shown that above the CMC, the spherical micelle core consists mainly of PPO and the hydrated PEO swollen outer shell or corona. The picture that emerges from these simulations is a step-wise micellization process that could explain the observed molecular-weight dispersion of Pluronic micelles. At lower micellar

concentration, the micelles consist of many copolymer aggregates that form independent hard-spheres; with increasing concentration (10 wt %) there are micellar clusters due to the coalescence of spherical micelles. Finally, a liquid-crystalline phase of disk-like micelles forms.

Pluronics are often used without further purification as starting materials in polymeric synthesis and drug delivery applications. Furthermore, the comparison between purified and "as received" samples is complicated by the possible shift in the molecular weight distribution during extraction.[5] Therefore, it would be convenient to be able to directly quantify the Pluronic CMC and CMT values obtained from some suitable characteristic of the Pluronic itself, such as fluorescence, in commercial samples. Typical commercial Pluronic F127 samples contain ~ 100 ppm of the antioxidant butylated hydroxytoluene (BHT), which we show can be used as a reliable marker for temperature dependent polymer reorganization when compared to a reporter such as the commonly used pyrene. Together, these different approaches have the potential to monitor distinct components of the micellization process. As part of our effort to develop novel nanomaterials incorporating Pluronics as an integral component, we describe a novel approach to characterize to the aggregation properties of Pluronic F127 using the fluorescence of the antioxidant BHT. Independent size distribution results using static light scattering and dynamic light scattering (DLS), transmission electron microscopy (TEM), and atomic force microscopy (AFM) all support the validity of this approach. These results demonstrate that the BHT spectral transitions observed in the excitation and emission fluorescence spectra of the commercial polymer samples may be exploited as a probe of structural reorganization.

Materials and Methods

Materials

The Pluronic® triblock copolymers P127 (PEO_{99}-PPO_{65}-PEO_{99}, Batches#: 038K0113 and 119K0073), Poloxamer 407, Pluronic 31R1 (PPO_{27}-PEO_4-PPO_{27}, Batch#: 04402BN), and Pluronic L-31 (PEO_1-PPO_{16}-PEO_1, Batch #: 01631MH) were used as received (Sigma Aldrich, Milwaukee, WI, USA). Polyethylene glycol 8000 (PEG 8000, Batch#: 314521) was used as received (J.T. Baker Chemical Co., Philipsburg, NJ). Different percentages of Pluronic solutions were prepared from 10 mM PBS buffer freshly made from milli-Q water. Pyrene (99%) and 2, 6-bis (1, 1-dimethylethyl)-4-methylphenol also known as butylated hydroxytoluene (BHT) were used as received (Sigma Aldrich, Milwaukee, WI, USA).

UV-Vis and Fluorescence Spectroscopy

UV-vis measurements were done on a Varian Cary-100 spectrometer. All fluorescence spectra were recorded on a Model T PTI spectrofluorometer (Photon Technology International, Birmingham, NJ, USA), equipped with a magnetic micro-stirrer and Peltier temperature regulation. The lamp, excitation, emission and photon multiplier tube slits were set at 0.30, 0.20, 1.00 and 1.60 mm, respectively. For Pluronic solutions the excitation and emission spectra were monitored at $\lambda_{em} = 360$ nm and $\lambda_{ex} = 260$ nm respectively. For pyrene containing solutions, used to monitor the micellization process of the Pluronic, the excitation and emission spectra were monitored at $\lambda_{em} = 395$ nm and $\lambda_{ex} = 335$ nm, respectively. Static light scattering experiments were done at $\lambda_{em} = 330$ nm and $\lambda_{ex} = 330$ nm, at a 90° scattering angle respectively. The spectra were

corrected for inner filter effects by determining the extinction coefficients, $\varepsilon(\lambda)$, from a series of spectra 1 to 20 % w/v or by calculating from a 20 % w/v F127 stock solution. Standard curve determination of BHT in methanol gives the value of molar absorption coefficient $\lambda_{279} = 1.77 \pm 0.04 \times 10^3 \text{ M}^{-1}\text{cm}^{-1}$. The corrected intensities were determined from the relationship suggested by Lakowicz,[21] $F_c = F_o 10^{(\varepsilon(\lambda excitation) + \varepsilon(\lambda emission))/2}$, where F_c, and F_o are the corrected and uncorrected intensities, respectively.

Material Characterization

The CMC values determined from the BHT probe were compared to the pyrene solubilization method. Pluronic solutions were prepared as described previously by direct dissolution in 10 mM PBS, giving a final pyrene concentration of 0.6 μM.[22] The purity, molecular weight and size distributions of Pluronic F127 polymer were characterized by desorption/ionization time-of-flight (MALDI-TOF; Bruker autoflex), GC-MS (Agilent 6989 N GC and Agilent 5973 mass selection detector), size exclusion chromatography (SEC) (Waters 510 pump, 717 auto sampler, 410 differential refractometer), DLS (NICOMP 370 submicron particle sizer), TEM (Zeiss, operating at 80 kV) and AFM (Veeco Dimension 5000 in tapping mode). The Pluronic F127, as received, had $\approx$ 25% w/v PPO-PEO lower molecular weight diblock polymer consistent with published work (Figure 2.1).[6b, 13a]
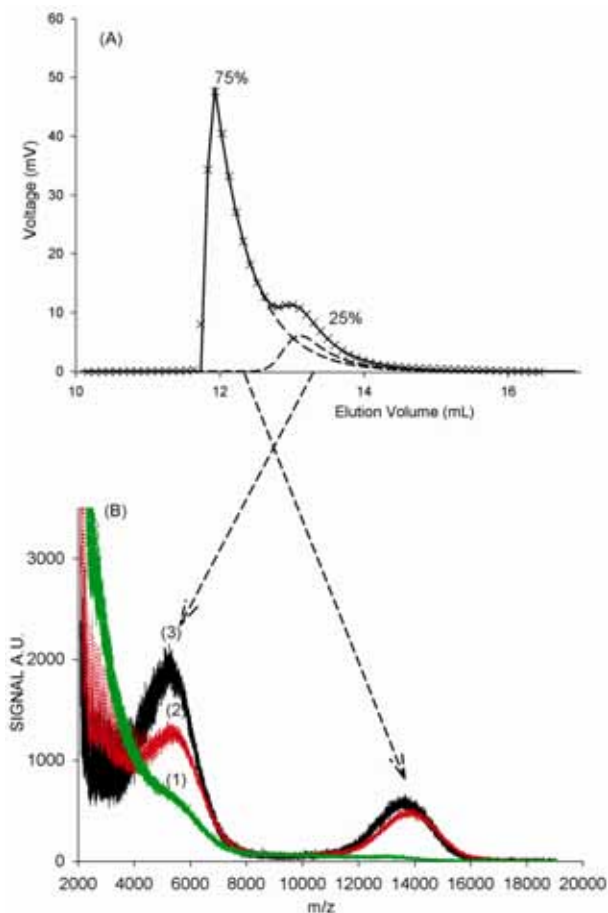
Figure 2.1 Molecular weight distribution of the native polymer as analyzed by: (A) SEC (B) MALDI-TOF-MS. For SEC, isocratic separation was performed using two PLgel 3μm Mixed-E 300 x7.5 mm columns (Varian Inc.) connected in tandem and coupled with a PLgel 3μm 50 x 7.5 mm guard column (Varian Inc.). Column temperature was controlled at 35°C. The mobile phase consisted of stabilized tetrahydrofuran (THF), with a flow rate of 1 ml/min. In B, the plots are: (1) hexane extract, (2) F127 residue after hexane extraction, (3) as-received polymer. Positive ion spectra were recorded in reflectron mode applying an accelerating voltage of 20 kV. The spectra of 50-80 shots were averaged to improve the signal-to-noise ratio. Samples were prepared by dissolving the analyte in a 1:1 (v/v) acetonitrile and water solution and dropping 0.5 μl on a dithranol (10 mg/ml, 0.5 μl in THF) matrix that was deposited previously on the sample plate (stainless steel). The drop was allowed to dry, and the sample holder then introduced into ion source.

Partition Coefficient Calculation

To estimate the partitioning of the probe into the F127 micellar phase we used a modified model developed by Kabanov *et al.*.[2] The extent of partitioning of the probe is quantified by the micelle-water coefficient (*P*) defined by the ratio of the probe concentrations in the micellar and aqueous phases:

$$P = \frac{[\Pr obe]_m}{[\Pr obe]_{aq}} \qquad (1)$$

The fractional uptake (α) of the probe into the micelles is given by:

$$\alpha = \frac{I - I_0}{I_\infty - I_0} \quad 2(a); \quad \alpha = \frac{I_\infty - I}{I_\infty - I_0} \quad 2(b)$$

where I is the total fluorescence intensity, I_o is the baseline intensity, and I_∞ is the saturation level of fluorescence. With increasing polymer concentration, equation 2(a) is applied when the intensity increases and 2(b) is used when the intensity decreases. This fraction can be expressed in terms of *P*:

$$\alpha = \frac{P\Theta}{P\Theta + 1 - \Theta} = \frac{P\upsilon(C_{pl} - CMC + Hx)}{P\upsilon(C_{pl} - CMC + Hx) + (100 - \upsilon(C_{pl} - CMC + Hx))} \qquad (3)$$

where the volume fraction of the micelle phase, Θ, is given by $0.01\upsilon(C_{pl} - CMC + Hx)$, where υ (assumed an average value of 0.87 for Pluronics[2, 23]) is the partial specific volume, C_{pl} is the total Pluronic concentration in % w/v, and CMC is the concentration at

the inflection point. The Hx term is an offset such that Θ is ≈ 0 below the CMC. This model assumes at the CMC, C_{pl} is $\approx$ CMC, i.e., most of the F127 is in the micellar phase.

Results

Sensitivity of the Observed BHT Electronic Transitions to the Pluronic F127 Microenvironment

Figure 2.2 compares the excitation and emission spectra of Pluronic F127 at 37°C. Three peaks are resolved in the excitation spectrum centered at $\approx$235, 280, and 313 nm. In the emission spectrum, two peaks at $\approx$ 305 and 325 nm are resolved. These peaks are assigned to electronic transitions of BHT, since the F127 as-received samples contain 100 ppm BHT antioxidant preservative (Figure 2.3). The assignment of these peaks to BHT is supported by the intensity increases of these peaks when additional BHT (10 μM) is added to a 5% w/v F127 solution (Figure 2.4). We also measured the fluorescence of lower molecular weight Pluronics L31 and 31R1 and PEG 8000 and found peaks associated with phenolic antioxidants (Figure 2.5).

In separate experiments using the pyrene dye probe, we plotted the ratio of the first vibrational band I_1 (372 nm), the highest energy vibrational band, to the fluorescence intensity of the third vibrational band I_3 (385 nm) that is known to correlate with solvent polarity (Figure 2.6).[24] This (I_1/I_3) ratio, known also as the "Py scale", correlates with other scales of polarity such as the π* scale of Kamlet and Taft[24a] and is a measure of changes in the microenvironment around the pyrene. Moreover, the inflection point of the sigmoid fit to (I_1/I_3) against copolymer concentration has been used as a measure of the CMC and CMT.[25] With increasing Pluronic concentration and subsequent micelle formation, this ratio drops from $\approx$ 1.6 to $\approx$ 1.1 and $\approx$ 0.9 at 25 and 37°C, respectively.
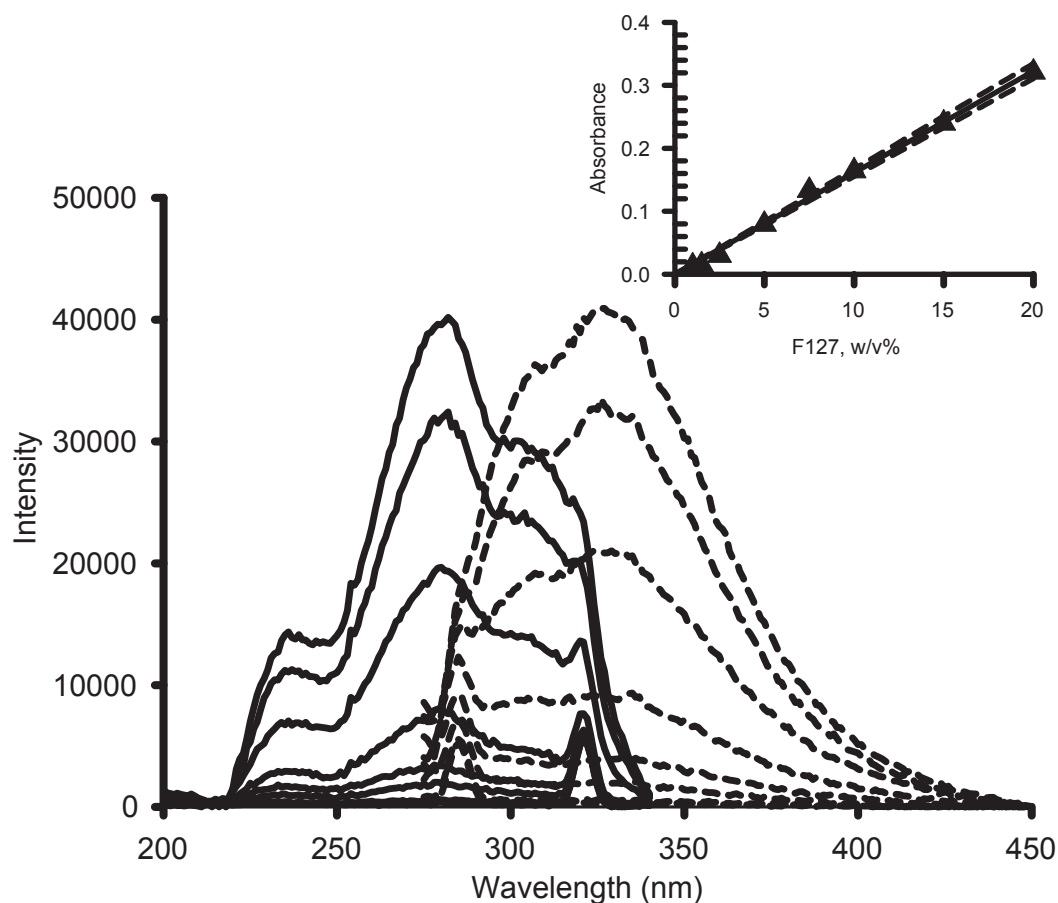
Figure 2.2 Inner filter corrected excitation (solid lines) and emission (dotted lines) spectra of Pluronic F127 taken at 37°C, monitored at λ_{em} = 360 nm, and λ_{ex} = 260 nm at % w/v concentrations: 0.01, 0.1, 0.5, 1, 2, 5, 8, 10 in 10 mM PBS. Observed peaks at $\approx$ 321 nm (excitation) and 285 nm (emission) are from the Raman scatter of water. The inset is the Beer-Lambert plot at λ_{abs} = 279 nm, with the dotted lines being the 95% confidence intervals. For 100 ppm BHT in F127, the calculated weight-volume % absorption coefficient was $(1.60 \pm 0.05) \times 10^{-2}$ (w/v%)$^{-1}$ cm^{-1}.
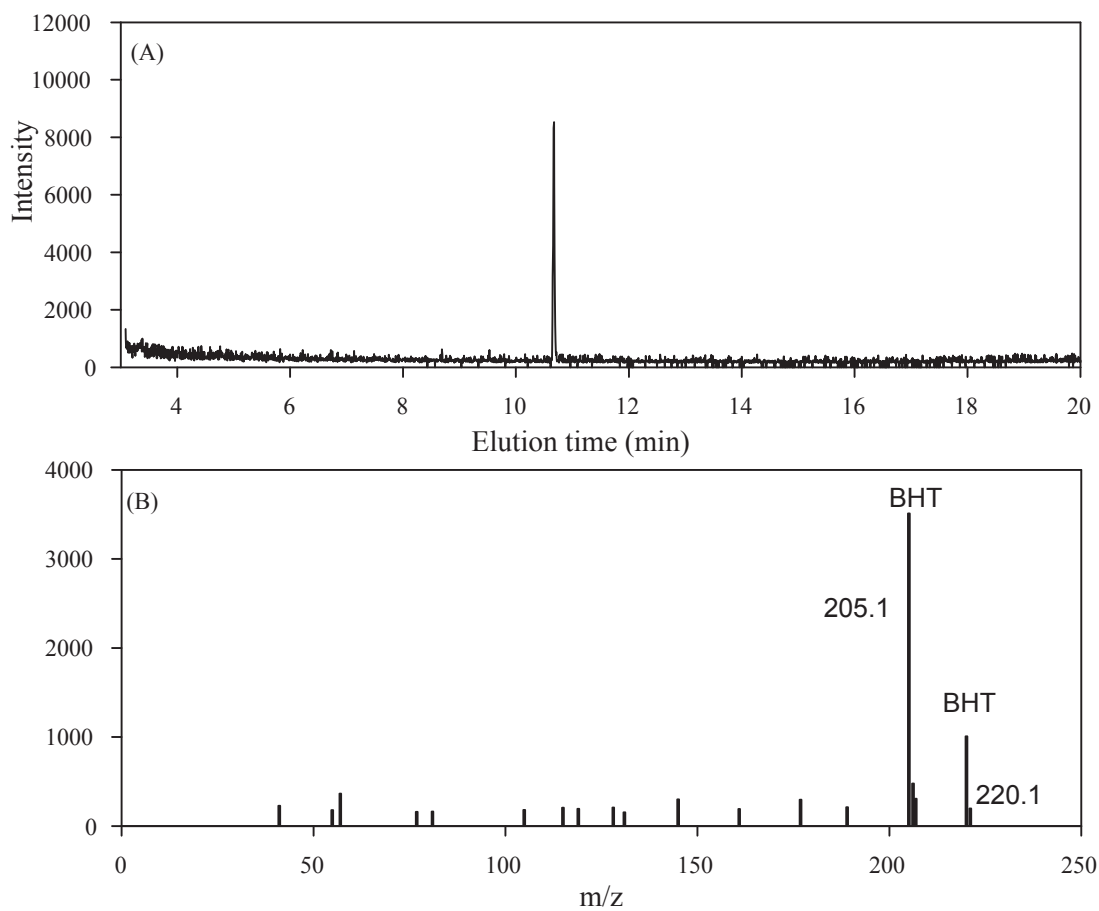
Figure 2.3 GC-MS chromatogram (A) and (B) MS using a 1 μl aliquot of the hexane extract used to wash 5 g Pluronic F127 that was characterized by MALDI-TOF (Figure 2.1) and fluorescence spectroscopy. The 205.1 m/z species is BHT after the fragmentation of a -CH$_3$ group.
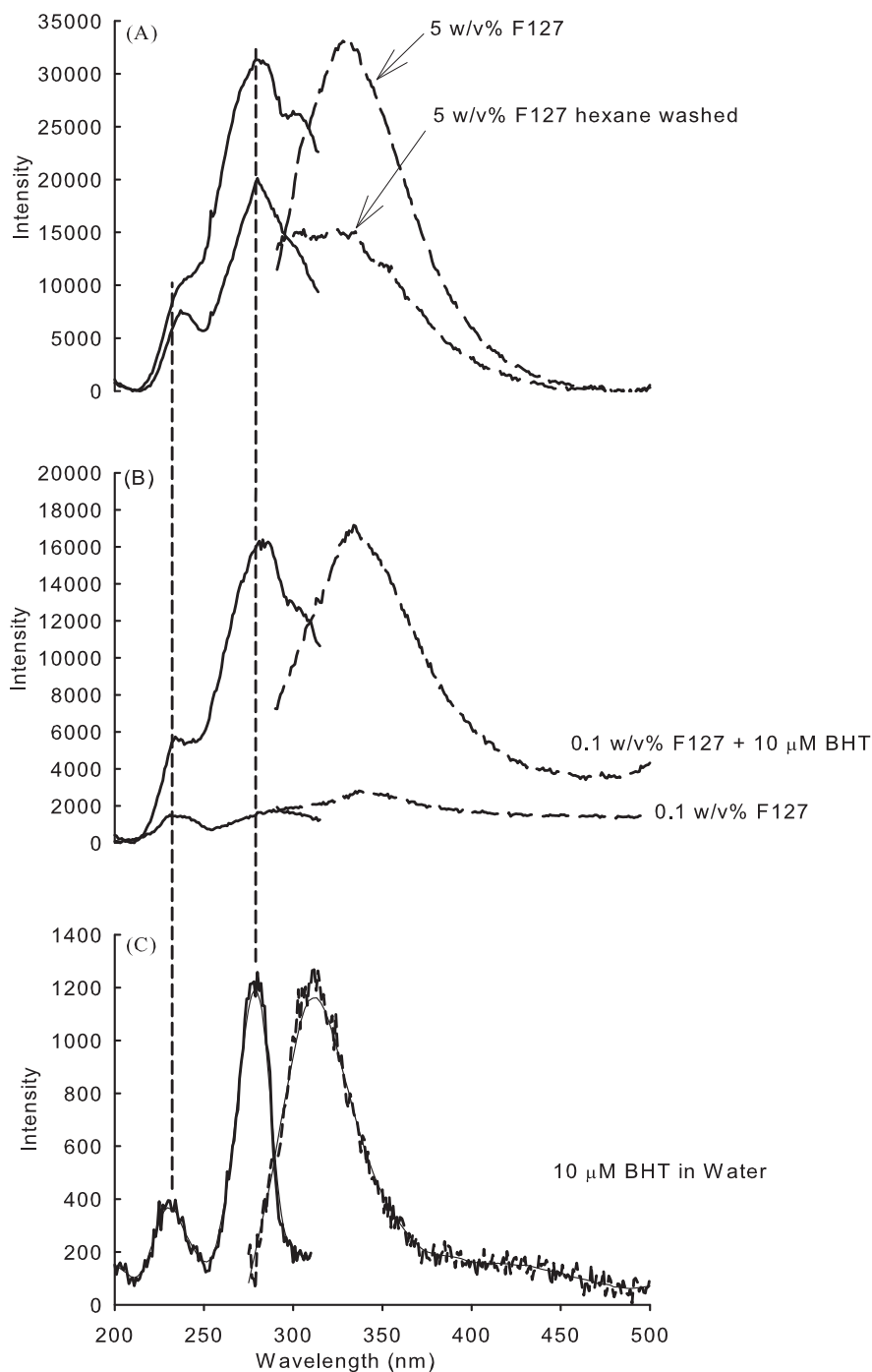
Figure 2.4 (A) Excitation and emission spectra of various fractions of Pluronic F127 taken at 25°C, monitored at λ_{em} = 360 nm, and λ_{ex} = 260 nm. (A) Comparison 5% F127 as received and washed in hexanes. (B) Comparison 0.1% F127 as received and with 10 μM BHT added. (C) A Spectrum of 10 μM BHT in water.
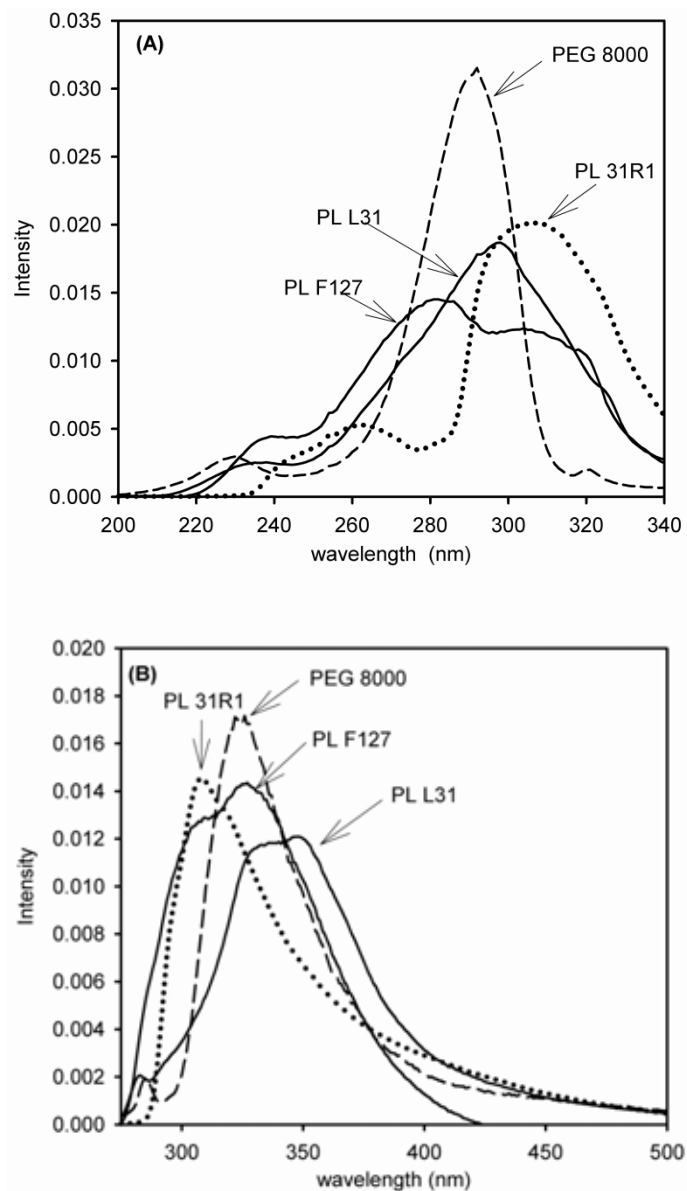
Figure 2.5 Excitation and emission spectra taken at 25 °C of the Pluronics F127, L31, 31R1 and poly(ethylene) glycol 8000 each at 10 wt% concentration that have been normalized to the area of the spectral region. (A) Excitation spectra monitored at λ_{em} = 360 nm. (B) Emission spectra monitored at λ_{ex} = 260 nm. The peaks at 320 nm and 285 nm respectively are due to the Raman scattering from the water.
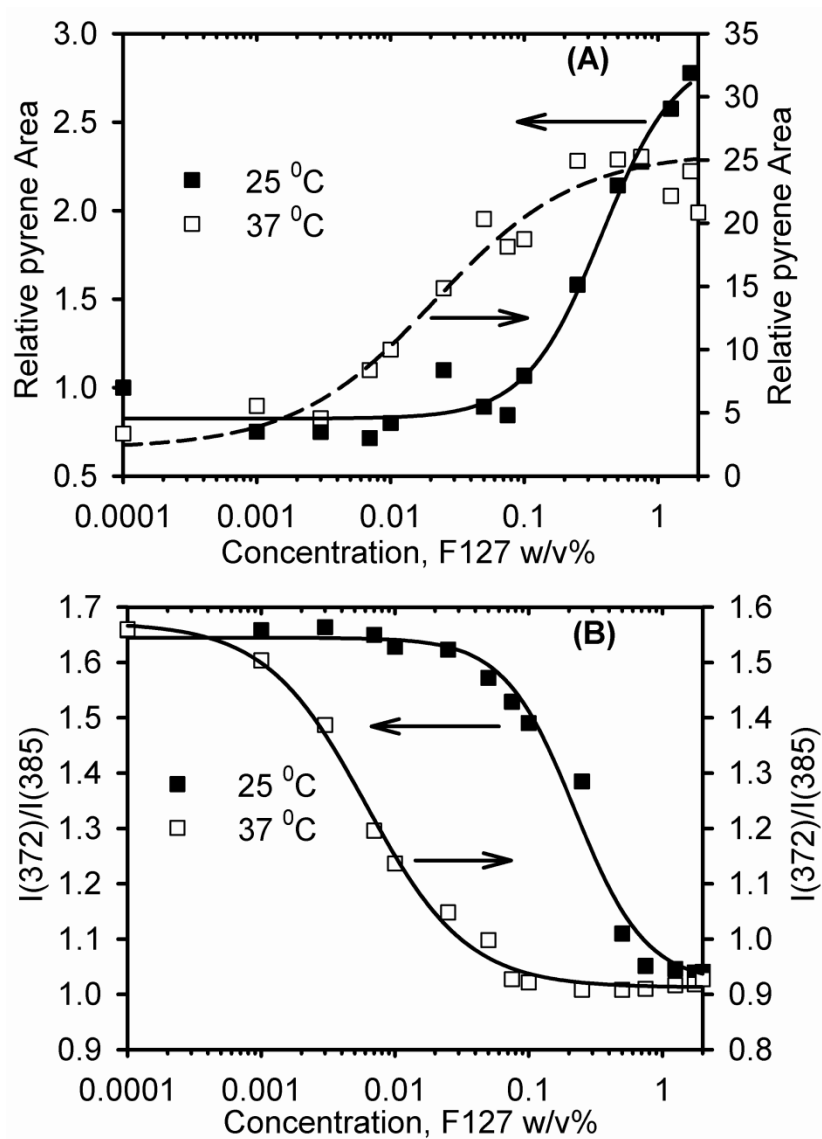
Figure 2.6 This figure shows the variations in pyrene fluorescence intensity against F127 w/v% concentration at 25 and 37°C, monitored at λ_{ex} = 335 nm. (A) Integrated pyrene intensities (350-500 nm). (B) The (I_{385}/I_{372}) ratios of the pyrene.

Below the CMC and CMT, the I_1/I_3 ratios correspond to a polar environment and when the concentration increases, this ratio decreases as the environment around the pyrene becomes more hydrophobic.[24, 25b]

Figure 2.7 shows how the BHT excitation and emission peak intensities change with F127 concentration. Figure 2.7(A) had 10 μM BHT added to each F127 concentration at 25ºC so that the intensity baseline was above the noise level. At low F127 concentration, the BHT is in a polar aqueous microenvironment. The fluorescence intensity of BHT increases significantly upon aggregation. This is evidenced by the sharp break around ~ 0.1% w/v of F127 where the fluorescence from the added 10 μM BHT dominates the signal. Moreover, analogous to the changes in the pyrene I_1/I_3 intensity ratios, we can plot the fractional BHT intensity (peak height/spectral region area) against Pluronic F127 concentration and recover the same micellization transition. This is because the concentration of BHT will increase in proportion to the concentration of F127 but the *fraction* of BHT relative to F127 will remain the same.

Latz and Hurtubise[26] showed that the luminescence properties of BHT are dependent on the solvent polarity. They found that the BHT fluorescence intensity was significantly higher in ethanol than chloroform with the emission maxima being 330 and 350 nm in chloroform and ethanol, respectively. This large difference in intensity may be due partially to the heavy atom effect of chlorine, resulting in an increase in the rate of inter-system crossing from the singlet to the triplet state of the molecule.[27] As the solvent polarity increases, the extent of solvent relaxation is greater resulting in emission at lower energies and longer wavelengths.[21]
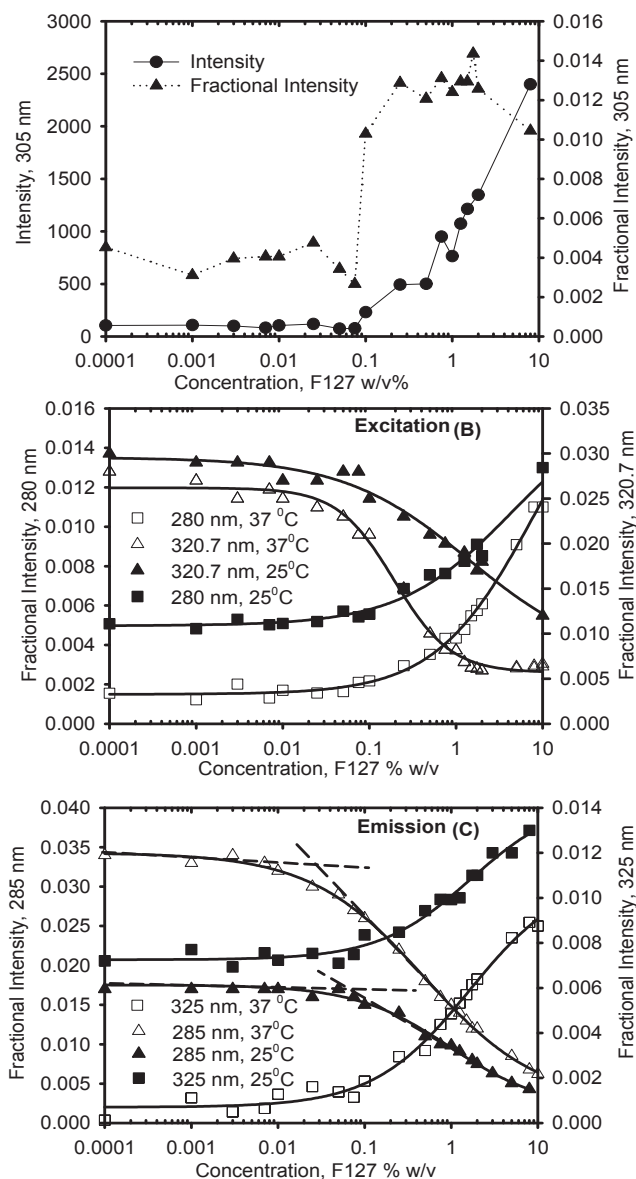
Figure 2.7 (A) Plots of the absolute and fractional fluorescence intensities (peak intensity/spectral area between 275- 400 nm) of the 305 nm peak at 25°C originating from F127 and 10 μM added BHT. (B) Plots of the excitation fractional intensities (peak intensity/spectral area between 200- 340 nm) of the 280 nm (BHT - squares) and 320.7 nm (Raman - triangles) peaks at 25 (black) and 37°C (white). (C) Plots of the fractional fluorescence intensities (peak intensity/spectral area between 275- 400 nm) of the 285 nm (Raman - triangles) and 325 nm (BHT -squares) peaks at 25 and 37°C. Values of CMC are determined from the intersection of the dotted lines or the inflection of the sigmoid fit. The original spectra were corrected for the inner filter effect.

46

The relative contributions of the peak components in the excitation and emission spectra in the *absence* of added BHT that are normalized to the spectral region areas at 25 and 37°C are shown in Figure 2.7(B) and (C). Between the 0.01 and 1% w/v F127 concentration, the changes in the excitation (280 and 313 nm) and emission (305 and 325 nm) spectra are a result of the sensitivity in the n $\rightarrow \pi^*$ transitions to the polarity of the BHT microenvironment. Analysis of the UV-Vis data above 250 nm shows that the absorbance is < 0.05 below 5% w/v F127 indicating that inner filter effects are insignificant below this concentration.

We used these changes in fractional peak intensities to follow the changes in the microenvironment around the BHT. The CMC values determined from the inflection points decrease with higher temperature. Using the inflection points from the Raman signals provides a more reliable way to determine the polarity changes around BHT because extrapolating to the break points in the BHT signals is limited by the low signal-to-noise below 0.1% w/v F127. The Raman signals decrease with higher F127 concentration as its contribution relative to BHT in the spectral profile decreases. Figure 2.7 points to the feasibility of using the electronic transitions in the Pluronic excitation and emission spectra as a probe of polymer aggregation.

The CMC values obtained at 25°C from the inflection points agree within an order-of-magnitude of the published values obtained from surface tension, DLS, and dye probe techniques (Table 2.1). At 37°C the BHT signal-to-noise will be too low for an accurate determination of the CMC.

Table 2.1 Summary of the measured CMC (% w/v) values determined for Pluronic F127 at 25 and 37[o]C.

Probe	37°C	25°C	Lit. 37 °C	Lit. 25°C
[c] 320.7 nm excitation Raman peak	[a] 0.19 ± 0.02	[a]1.4 ± 0.6	0.001 (dye)[23a]	1 [18a] (surface Tension)
			0.0035 (dye)[23b]	0.7 [16](dye)
			0.025 (dye)[11b]	0.26 ± 0.03[13b] (DLS)
				0.09 [23a] (dye)
[d] 285 nm Fluorescence Raman peak	[a] 0.50 ± 0.04	[a] 0.97 ± 0.03		
	0.030 ± 0.005	0.060 ± 0.005		
Static Light Scattering	[b] 0.020 ± 0.005	0.50 ± 0.05		
	[b] 0.15 ± 0.05			
Pyrene I(372)/I(385)	[a] 0.011 ± 0.002	[a] 0.25 ± 0.02		
Pyrene I(350 – 450 nm)	[a] 0.028 ± 0.005	[a] 0.46 ± 0.05		

[a] Values obtained from the inflection of a sigmoid fit. Values mean ± SD.
[b] Values for breaks 1 and 2.
[c] Normalized with respect to spectral range.
[d] Normalized with respect to spectral range (position of the break).

We note that the pyrene probe technique will be more sensitive than using BHT because the pyrene extinction coefficient is $\sim 10^4$ M^{-1} cm^{-1} compared to $\sim 10^3$ M^{-1} cm^{-1} for BHT; however, our approach can be used reliably for polymers where the CMC values are known *a priori* to be above 0.1 w/v% for 100 ppm added BHT. For example, the Pluronics L64, F68, and P85 have CMC values above 1 w/v% at room temperature.[13b] These Pluronics have found application in drug delivery.[1c, d]

The static light scattering results in Figure 2.8 at 25 and 37°C show a 3 to 10-fold decrease in the aggregation concentration. We note that the mixtures were left to equilibrate at 37°C for at least 10 hours to minimize relaxation processes of BHT during its incorporation in the Pluronic micelles that will cause artifacts in the intensity versus concentration plots.[2] The broad micellization transition that spans a ten fold concentration range at 37°C suggests different micellization stages. This step-wise process of micellization has been reported.[28] The first break (~0.01) may correspond to initial micelle formation (nucleation), but the interpretation of the second break is less definitive. There are two plausible explanations. The broad micellization transition may correspond to the coalescence of micelles forming non-spherical shapes, or could originate from PPO blocks from the diblock copolymer components being incorporated into the micelles. Batsberg *et al.*[29] analyzed Pluronic P85 by differential scanning calorimetry and concluded that the diblock components are not incorporated into the micelle.
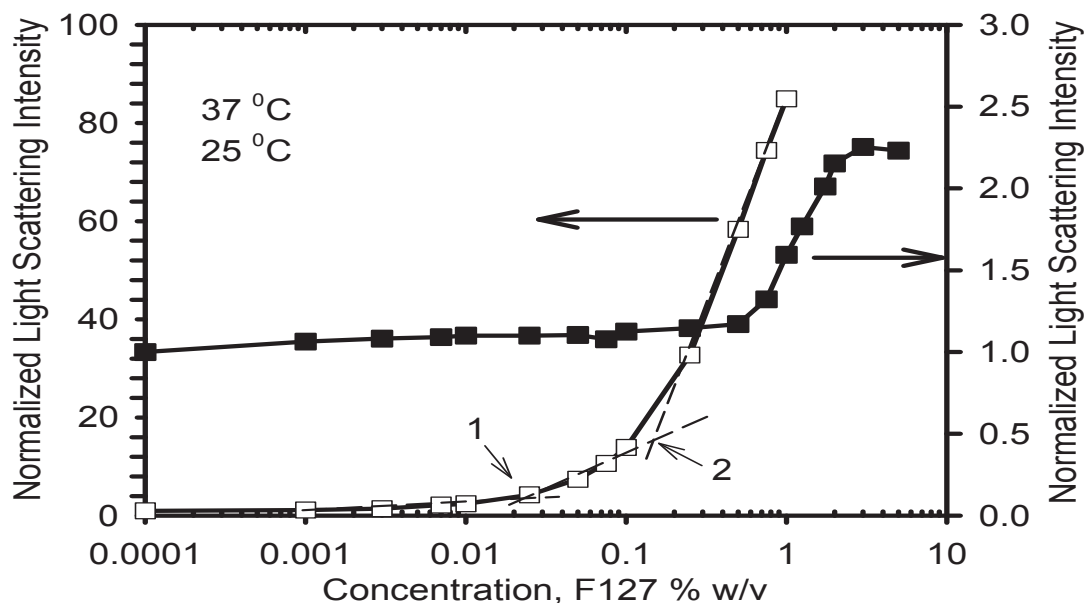
Figure 2.8 Static light scattering intensity as a function of F127 concentration at 25 and 37°C; the numbers correspond to the two breaks at 37°C.

Chromatography data by Mortensen *et al.*[13a] on Pluronic F127 indicate also that the diblock copolymer is not incorporated into the micelles, but their small angle neutron scattering (SANS) implicated some degree of association with the micelle corona. Booth and coworkers[30] showed that the aggregation behavior of the fractionated compounds and the unfractionated samples of Pluronic F127 did not differ significantly.

The micellization process is a complex phenomenon rather than a single stage event. This being the case, it is not unreasonable to expect that particular approaches will be more sensitive to certain aspects of the electronic transitions involved. Different agents, with characteristic affinities, will then have the potential to highlight particular components of micellization. Although light scattering and pyrene dye methods are more

sensitive in detecting the earlier stages of micellization, the additional attractiveness of using the BHT probe is that there is no need to add an external dye decreasing the time needed for sample preparation. Nevertheless, there are caveats to using this method to estimate the CMC: (1) the CMC must be in the Pluronic concentration range where the BHT signals have sufficient signal-to-noise; (2) if an additional probe molecule is present, there should be minimal spectral overlap; (3) correction for inner filter effects may be necessary at high Pluronic concentrations ($> 5\%$ w/v).

The partition coefficients of pyrene and BHT were determined from non-linear least squares fits of plots of α against C_{pl} (Table 2.2). To evaluate α, Equation 2(a) was applied to pyrene intensities and 2(b) to the pyrene I_1/I_3 ratios and BHT relative Raman (285 nm) intensities, respectively. Comparison of the partition coefficients between BHT and pyrene shows that the partition coefficient increases $\sim$ 40-fold for pyrene taking the measurements from the I_1/I_3 ratios compared to $\sim$ 2 fold for BHT when the temperature was increased from 25 to 37°C. Indeed, our calculated value of the partition coefficient for pyrene at 37°C using the I_1/I_3 ratios is in good agreement with the published value of $\approx 2 \times 10^4$.[23] Figure 2.9 shows an example plot comparing BHT and pyrene at 37°C. At F127 0.1 % w/v the fractional uptake, the values for pyrene and BHT are > 0.8 and ~ 0.1, respectively, indicating that the extent of partitioning of BHT in the micelle core may be influenced by the unfavorable steric interactions from its *tert*-butyl groups with the PEO segments and the incorporated water molecules.[23b]

Tables 2.1 and 2.2 show that there are discrepancies in the calculated CMC, P and Hx values determined from the pyrene signals between absolute and relative I_1/I_3. The CMC values are consistently lower from I_1/I_3 measurements suggesting that this ratio is

more sensitive than the intensity to the onset of aggregation. Moreover, the lower

partition coefficients determined from the pyrene intensities may be due to the partial

fluorescence quenching from the water present in the micellar core and intermediate

regions. In contrast, one would anticipate uniform quenching of the fluorescence in the

pyrene vibronic fine-structure and thus, this effect would be compensated by using the

I_1/I_3 ratio. The intensity changes in the fluorescence signals with increasing Pluronic

concentration are the result of the changes in the microenvironment around the BHT as it

partitions preferentially into the PPO core. Figures 2.2 and 2.7 show the feasibility of

using the BHT electronic transitions in the Pluronic excitation and emission spectra as a

probe of polymer aggregation where the difference in the CMC values between 25 and

37°C observed in the Raman scatter is driven thermodynamically by the larger entropy

contribution in the free energy.
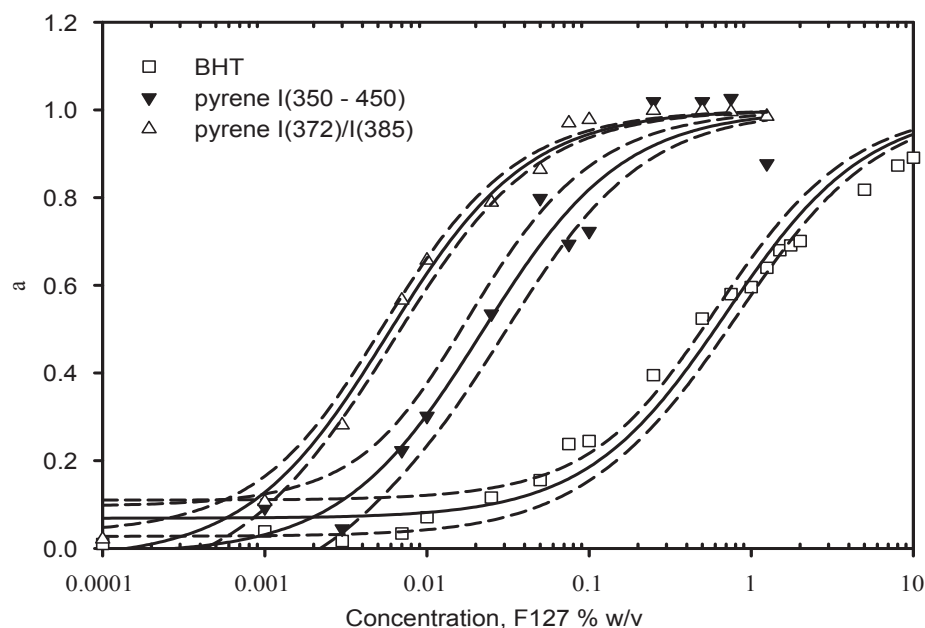
Figure 2.9 Example <u>plots of the extent of probe partitioning</u>, α, of pyrene and BHT against F127 concentration at 37°C. The solid lines are non-linear least-squares fits using equation 3 and the dotted lines are the calculated 95% confidence intervals. Curve fits were done using SigmaPlot 11.

Table 2.2 BHT and pyrene micelle - water partition coefficients and concentrations determined from α versus F127 % w/v at 25 and 37°C.

Probe	Partition Coefficient (P)		Hx % w/v	
	37°C	25°C	37°C	25°C
BHT	$(1.79 \pm 0.05) \times 10^2$	$(1.04 \pm 0.03) \times 10^2$	$(5.42 \pm 0.04) \times 10^{-1}$	1.05 ± 0.02
Pyrene	$(3.7 \pm 0.06) \times 10^3$	$(2.6 \pm 0.1) \times 10^2$	$(3.00 \pm 0.02) \times 10^{-2}$	$(4.4 \pm 0.5) \times 10^{-1}$
Pyrene I_{372}/I_{385}	$(1.94 \pm 0.02) \times 10^4$	$(5.0 \pm 0.1) \times 10^2$	$(6.08 \pm 0.01) \times 10^{-3}$	$(2.40 \pm 0.05) \times 10^{-1}$

Values mean ± SD determined from the fitted parameters.

Previous studies show that higher temperatures leads to a sharp CMC decrease along with increases in aggregation number, micelle size, and the fraction of polymer molecules in micelle form[11a, 18a] and that the preferential dehydration of PPO segments is responsible for micellization.[9a, 9c, 16, 25a] These studies provide support for a model of micellization, where structural reorganization occurs as a result of the replacement of hydrogen bonds between water and polymer with the intra- and intermolecular hydrogen bonds between methylene hydrogens and the oxygen component of PO-CH$_2$- of a hydrophobic PPO core. During latter stages of micellization, the cleavage of the coiled *gauche* conformations in PPO segments due to intra-molecular (C-H)$^{\cdots}$ O attractions are attributed to the formation of thermodynamically stable stretched *trans* conformations upon micellization.[9a] Detailed NMR studies support the interpretation of further Pluronic intermolecular hydrogen bond interactions, where a new resonance signal at ~ 3.42 from the PO-CH$_2$- protons above the CMT has been assigned to the breakdown of the intramolecular hydrogen bonding between the methylene protons and the ether oxygen's of the PPO segments.[9a, 9c]

Temperature Dependence of the BHT Fluorescence in Pluronic F127

Having demonstrated that the 305 nm and 325 nm electronic transitions of BHT associated with F127 are sensitive to the microenvironment, we investigated the effect of temperature on the BHT fluorescence wavelength and intensity transitions in water. The decrease in the BHT (305 nm) peak intensity in water with increasing temperature is consistent with the increased fluorescence collisional quenching by oxygen in the water (Figure 2.10).
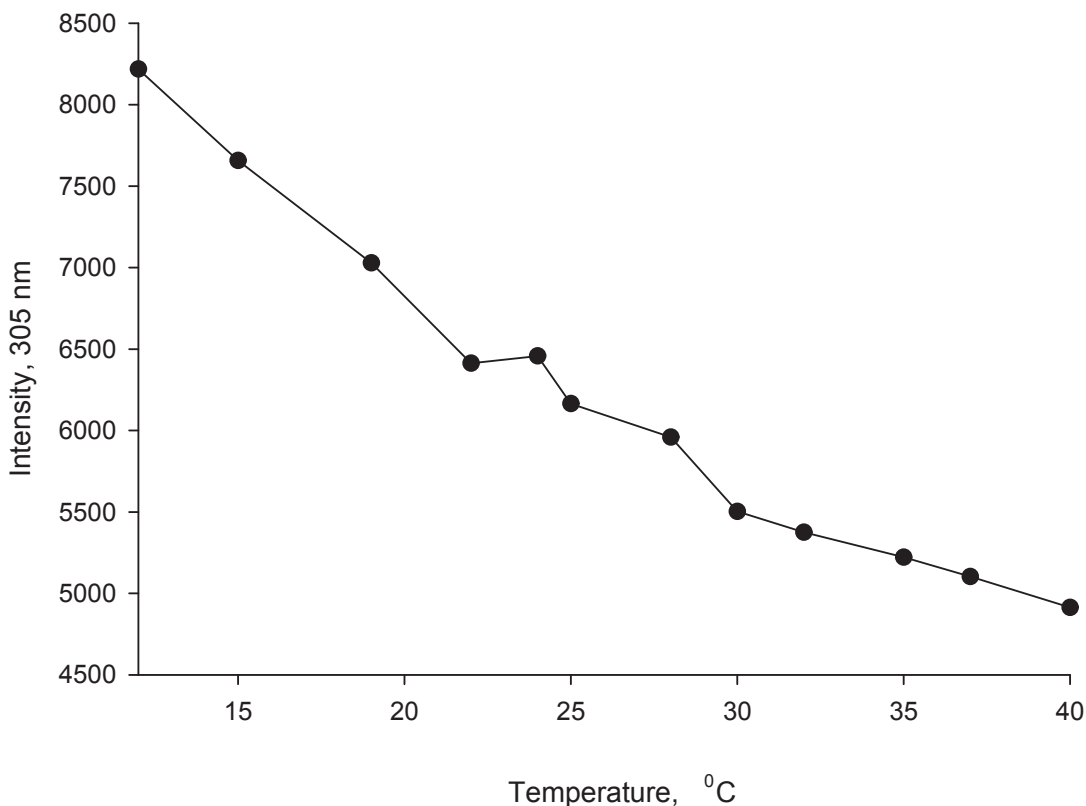
Figure 2.10 Plot of the 305 nm peak against temperature.

For oxygen in water at 25°C, its diffusion coefficient is 2.5 x 10^{-5} cm^2s^{-1}; assuming a diffusion coefficient ~ 10^{-5} cm^2s^{-1} for BHT and a collision radius of 5 Å, yields a bimolecular rate constant of ~ 10^{10} $M^{-1}s^{-1}$.[21] The quenching efficiency is effectively unity making fluorescence quenching proportional to the bimolecular quenching constant; this accounts for the pseudo-first order decay in the fluorescence intensity with higher temperature.

For BHT in F127, Figure 2.11(A) is an example of 2% w/v F127 fluorescence spectra with increasing temperature. We note that the positions of the peak maxima will vary by polymer batch and extent of BHT degradation. In contrast to BHT in water, the

total intensity of the fluorescence signal increases, with the most prominent intensity increases occurring in the 285 and 305 nm peaks. Moreover, we found that using commercial purified Poloxamer 407 (diblock impurity removed) at 1 % w/v showed the same thermo-reversible behavior (not shown). This supports the conclusions by Batsberg *et al.*[29] and Booth *et al.*[30] that the diblock impurities do not influence polymer aggregation.

Figure 2.11(B) shows that the integrated intensity between 15 and 37°C can be used to estimate the CMT. At the CMT the fluorescence intensity sharply increases as the BHT becomes associated with the aggregated polymer. In a few samples, data was collected as the mixture was cooled. The results were identical to when the sample was heated, confirming no hysteresis in the measurements consistent with equilibrium in our systems. In separate experiments where F127 was incubated at 37ºC for 48 hours and there was BHT degradation as determined by UV-vis and fluorescence spectroscopy, we were still able to thermally cycle the fluorescence intensities.
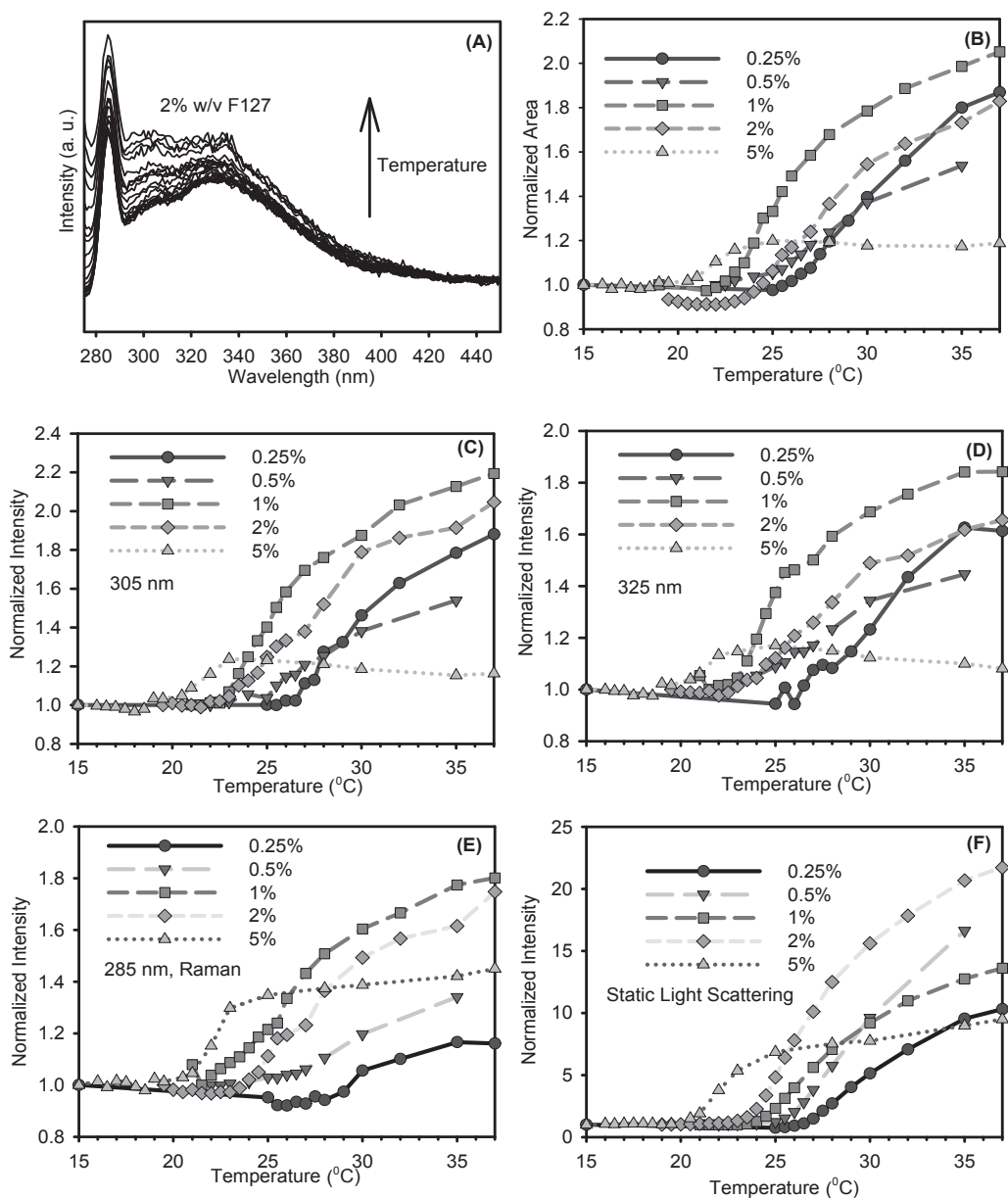
Figure 2.11 (A) Fluorescence intensity plots of 2% w/v F127 as function of temperature between 19 and 37°C. (B) Normalized fluorescence intensities of the 275 - 450 nm spectral region as a function of temperature for F127 concentrations 0.25, 0.5, 1, 2 and 5% w/v. The normalized fluorescence intensities as against temperature for F127 concentrations 0.25, 0.5, 1, 2 and 5% w/v monitored at (C) 305, (D) 325, and (E) 285 nm, respectively. (F) Static light scattering intensity as a function of temperature for F127 concentrations 0.25, 0.5, 1, 2 and 5% w/v.

Figure 2.11(C)-(E) examines the fluorescence intensities that were normalized to the temperature below aggregation. From the BHT (305 nm, 325 nm) and Raman (285 nm) intensities the CMT can be determined. The CMT values at 0.25% w/v (26°C), 0.5% w/v (25°C), 1% w/v (23°C), 2% w/v (22°C), and 5% w/v (19°C) are in good agreement with the literature[16, 25b] and static light scattering (Figure 2.11(F)).

Characterization of the Micelle Size Distribution

Temperature influences profoundly the phase separation of Pluronic copolymers. This phase separation was quantified by DLS measurements at 23, 25 and 37°C of 2% w/v F127 (Figure 2.12(A)). Upon increasing the temperature in the threshold CMT region from 23 to 25°C, the average diameter increases from 7.6 nm to a heterogeneous micelle size distribution that can be described by two Gaussian populations centered at 35 and 51 nm. The increase in core size agrees with the predictions of theoretical models.[18a, 31] We can infer from the differences in the hydrodynamic diameter between 23 and 25°C that micelle clusters are formed above CMT. Furthermore, the polydispersity of F127 decreases with temperature. At 37°C the distribution of F127 micelle size narrows and the average diameter decreases to 21 nm as more water is expelled from the increasing hydrophobic PPO core. This temperature dependence in the size distribution behavior for Pluronics was previously demonstrated for P104 and F108.[8b] Simulation results of P103 Yang *et al.*[31] also predict the decrease in polydispersity with temperature.
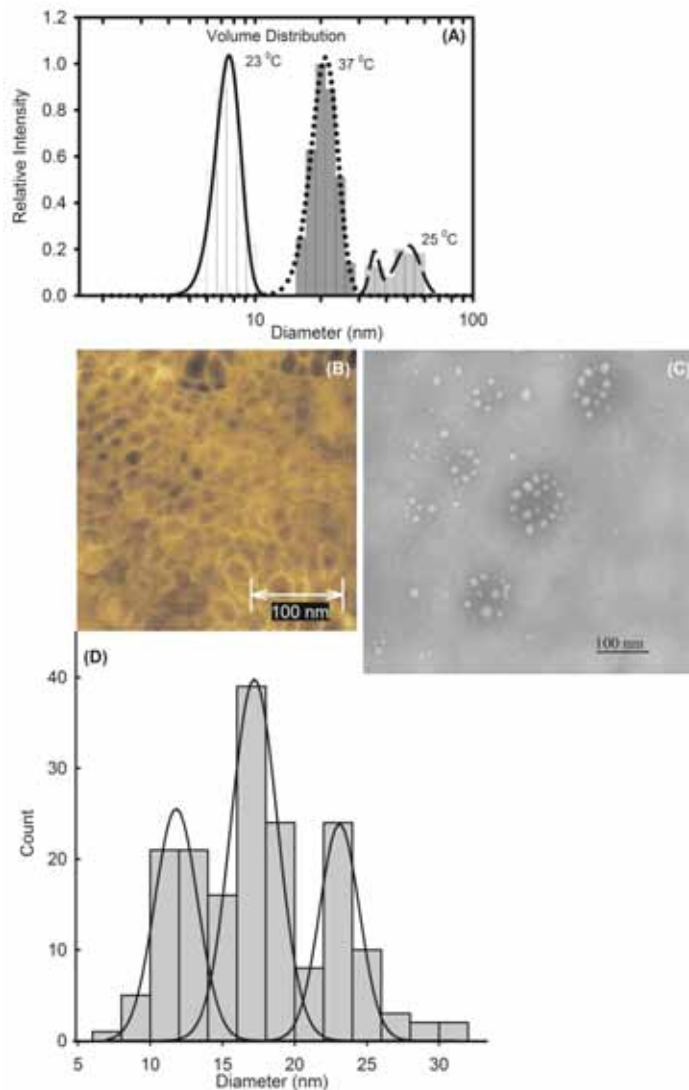
Figure 2.12 (A) Volume weighted DLS distributions for 2% w/v F127 at 23, 25, and 37°C. The lines are the Gaussian distributions centered at 7.6 nm (23°C), 21 (37°C), and at 35 and 51 (25°C) nm respectively. (B) AFM 300 x 300 nm^2 phase contrast image in tapping mode of 5% w/v Pluronic F127 air dried on a freshly cleaved mica substrate. (B) Typical TEM image of 5% w/v F127 stained with 2% w/v phosphotungstic acid. (D) A graph of the TEM size distribution for 5% w/v F127; this distribution is approximated by three Gaussians having means 11.8 ± 1.5 nm, 17.2 ± 1.6 nm, and 23.2 ± 1.4 nm (mean $\pm$ SD, n =176).

It is expected in the PEO backbone that with increasing temperature, there will be additional structural reorganization where the enthalpy cost of breaking ether-water hydrogen bonds is greater than the entropy gain associated with the break-up of ether-water hydrogen bonds and reduction in the structure of hydrating water with increasing temperature.[32] In contrast, the PPO segments undergo a higher degree of dehydration than the PEO segments excluding more water molecules, which is consistent with a water-insoluble liquid-like core created by the PPO blocks, during the micellization process.[11a, 14b, 15, 25a]

Room temperature (~23-25°C) TEM and AFM measurements were used to characterize the size distribution of 5% F127 (Figure 2.12(B)-(D)). The diameters determined from AFM and TEM measurements from air-dried F127 samples will be smaller than the values quantified by DLS because the micelles will collapse upon dehydration. The significant heterogeneity of the air-dried samples observed by AFM and TEM are consistent with our DLS results at 25°C for 2% w/v F127.

Lam *et al.*[6b] visualized the micelles of Pluronic L64 and F127 between 5 and 10% w/v by cryogenic TEM. In their vitrified samples, there was an increase in the degree of order between 5 and 10% w/v Pluronic F127 samples as well as the mean size of micelle core from 6 to 10.8 nm in diameter. In contrast to ours, their size distribution was found to be bimodal. They argued that this micelle bimodal size distribution reflected the bimodal molecular weight distribution in the polymer. However, in addition to the molecular weight as a potential determining factor, the observed heterogeneous micelle size distribution may also be the result of the concentration dependent aggregate formation, which is characteristic of a multi-step micellization process.[19, 31]

Discussion

In this work we present a novel approach to characterize temperature-dependent micellization using the fluorescence in commercial F127 samples from antioxidant molecules like BHT. The fluorescence of BHT is sufficiently sensitive to its microenvironment to be used as a reliable marker of temperature induced micellization. This sensitivity of BHT to the microenvironment polarity is shown by the fluorescence intensity increase in the presence of F127 with higher temperature (Figure 2.11). In the absence of F127, there is collisional quenching of the BHT fluorescence with higher temperature. We compared in sections 3.1 and 3.2 the BHT fluorescence method for determining the concentration and temperature dependent Pluronic F127 aggregation. In section 3.1 we noted that for a reliable determination of CMC, its value must be in the F127 concentration range of good BHT fluorescence signal-to-noise ratio and below where inner filter effects become significant. Because of the variations in polymer batches, the BHT fluorescence method would provide researchers a convenient way to characterize polymer aggregation, without having to add an external dye. An important application of our novel method is the *in-situ* characterization of the temperature-dependent aggregation of commercial Pluronic batches. Furthermore, this approach to determine the CMC and CMT can be applied to any copolymer system that contains phenolic antioxidants such as BHT.

Above the CMT, light scattering results suggest the coalescence of micelles, PPO core dehydration, and decreased heterogeneity in micelle size distributions. The electronic BHT transitions are directly impacted by the local environment where the partitioning in the micelle is influenced by steric and hydrogen bonding interactions with

the PEO and PPO segments. This is the case when comparing the changes in the

fluorescence intensities with increasing temperature. Higher fluorescence intensity values

with increasing temperature implies greater accommodation to the PPO environment,

reflecting the higher quantum yield of BHT in the micelle interior. Furthermore, light

scattering, AFM, and TEM data show high micellar heterogeneity around the CMT,

lending support to a multi-step model of aggregation. The earliest stage likely involves

the transition between unimers and low aggregation number micelles, while the second is

thought to be associated with micellar clusters and the beginning of coalescence into

larger aggregates.

References

1.   (a) Rösler, A.; Vandermeulen, G. W. M.; Klok, H.-A., Advanced drug delivery devices via self-assembly of amphiphilic block copolymers *Adv. Drug Deliv. Rev.* **2001,** *53*, 95-108; (b) Kabanov, A. V., Polymer genomics: An insight into pharmacology and toxicology of nanomedicines. *Adv. Drug Deliv. Rev.* **2006,** *58* (15), 1597-1621; (c) Kabanov, A. V.; Batrakova, E. V.; Alakhov, V. Y., Pluronic® block copolymers for overcoming drug resistance in cancer. *Adv. Drug Deliv. Rev.* **2002,** *54* (5), 759-779; (d) Batrakova, E. V.; Kabanov, A. V., Pluronic block copolymers: Evolution of drug delivery concept from inert nanocarriers to biological response modifiers. *J. Controlled Rel.* **2008,** *130* (2), 98-106.

2.   Kabanov, A. V.; Nazarova, I. R.; Astafieva, I. V.; Batrakova, E. V.; Alakhov, V. Y.; Yaroslavov, A. A.; Kabanov, V. A., Micelle Formation and Solubilization of Fluorescent Probes in Poly(oxyethylene-b-oxypropylene-b-oxyethylene) Solutions. *Macromolecules* **1995,** *28* (7), 2303-2314.

3.   Chiappetta, D. A.; Sosnik, A., Poly(ethylene oxide)-poly(propylene oxide) block copolymer micelles as drug delivery agents: Improved hydrosolubility, stability and bioavailability of drugs. *Eur. J. Pharm. Biopharm.* **2007,** *66* (3), 303-317.

4.   Holland, R. J.; Parker, E. J.; Guiney, K.; Zeld, F. R., Fluorescence Probe Studies of Ethylene Oxide/Propylene Oxide Block Copolymers in Aqueous Solution. *J. Phys. Chem.* **1995,** *99* (31), 11981-11988.

5.   Alexandridis, P.; Holzwarth, J. F., Differential Scanning Calorimetry Investigation of the Effect of Salts on Aqueous Solution Properties of an Amphiphilic Block Copolymer (Poloxamer). *Langmuir* **1997,** *13* (23), 6074-6082.

6.   (a) Mortensen, K.; Talmon, Y., Cryo-TEM and SANS Microstructural Study of Pluronic Polymer Solutions. *Macromolecules* **1995,** *28* (26), 8829-8834; (b) Lam, Y.-M.; Grigorieff, N.; Goldbeck-Wood, G., Direct visualisation of micelles of Pluronic block copolymers in aqueous solution by cryo-TEM. *Phys. Chem. Chem. Phys.* **1999,** *1*, 3331 - 3334.

7.   (a) Glatter, O.; Scherf, G.; Schillen, K.; Brown, W., Characterization of a Poly(ethylene oxide)-Poly(propylene oxide) Triblock Copolymer (EO_{27}-PO_{39}-EO_{27}) in Aqueous Solution. *Macromolecules* **1994,** *27* (21), 6046-6054; (b) Hvidt, S.; Joergensen, E. B.; Brown, W.; Schillen, K., Micellization and Gelation of Aqueous Solutions of a Triblock Copolymer Studied by Rheological Techniques and Scanning Calorimetry. *J. Phys. Chem.* **1994,** *98* (47), 12320-12328.

8.   (a) Jorgensen, E. B.; Hvidt, S.; Brown, W.; Schillen, K., Effects of Salts on the Micellization and Gelation of a Triblock Copolymer Studied by Rheology and Light Scattering. *Macromolecules* **1997,** *30* (8), 2355-2364; (b) Alexandridis, P.; Nivaggioli, T.; Hatton, T. A., Temperature Effects on Structural Properties of

Pluronic P104 and F108 PEO-PPO-PEO Block Copolymer Solutions. *Langmuir* **1995,** *11* (5), 1468-1476.

9.   (a) Ma, J.; Guo, C.; Tang, Y.; Wang, J.; Zheng, L.; Liang, X.; Chen, S.; Liu, H., Microenvironmental and conformational structure of triblock copolymers in aqueous solution by 1H and 13C NMR spectroscopy. *J. Colloid Interface Sci.* **2006,** *299* (2), 953-961; (b) Causse, J.; Lagerge, S.; de Menorval, L. C.; Faure, S., Micellar solubilization of tributylphosphate in aqueous solutions of Pluronic block copolymers - Part II. Structural characterization inferred by H-1 NMR. *J. Colloid Interface Sci.* **2006,** *300* (2), 724-734; (c) Ma, J.-h.; Guo, C.; Tang, Y.-l.; Liu, H.-z., 1H NMR Spectroscopic Investigations on the Micellization and Gelation of PEO-PPO-PEO Block Copolymers in Aqueous Solutions. *Langmuir* **2007,** *23* (19), 9596-9605.

10.   Lopes, J. R.; Loh, W., Investigation of Self-Assembly and Micelle Polarity for a Wide Range of Ethylene Oxide−Propylene Oxide−Ethylene Oxide Block Copolymers in Water. *Langmuir* **1998,** *14* (4), 750-756.

11.   (a) Wanka, G.; Hoffmann, H.; Ulbricht, W., Phase Diagrams and Aggregation Behavior of Poly(oxyethylene)-Poly(oxypropylene)-Poly(oxyethylene) Triblock Copolymers in Aqueous Solutions. *Macromolecules* **1994,** *27* (15), 4145-4159; (b) Alexandridis, P.; Athanassiou, V.; Fukuda, S.; Hatton, T. A., Surface Activity of Poly(ethylene oxide)-block-Poly(propylene oxide)-block-Poly(ethylene oxide) Copolymers. *Langmuir* **1994,** *10* (8), 2604-2612.

12.   Degtyarev, Y. N.; Schlick, S., Diffusion Coefficients of Small Molecules as Guests in Various Phases of Pluronic L64 Measured by One-Dimensional Electron Spin Resonance Imaging. *Langmuir* **1999,** *15* (15), 5040-5047.

13.   (a) Mortensen, K.; Batsberg, W.; Hvidt, S., Effects of PEOâˆ’PPO Diblock Impurities on the Cubic Structure of Aqueous PEO-PPO-PEO Pluronics Micelles: fcc and bcc Ordered Structures in F127. *Macromolecules* **2008,** *41* (5), 1720-1727; (b) Sharma, P. K.; Bhatia, S. R., Effect of anti-inflammatories on Pluronic® F127: micellar assembly, gelation and partitioning. *Int. J. Pharm.* **2004,** *278* (2), 361-377.

14.   (a) Su, Y.-l.; Liu, H.-z.; Wang, J.; Chen, J.-y., Study of Salt Effects on the Micellization of PEO-PPO-PEO Block Copolymer in Aqueous Solution by FTIR Spectroscopy. *Langmuir* **2002,** *18* (3), 865-871; (b) Su, Y.-l.; Wang, J.; Liu, H.-z., FTIR Spectroscopic Investigation of Effects of Temperature and Concentration on PEO-PPO-PEO Block Copolymer Properties in Aqueous Solutions. *Macromolecules* **2002,** *35* (16), 6426-6431.

15.   Guo, C.; Wang, J.; Liu, H.-z.; Chen, J.-y., Hydration and Conformation of Temperature-Dependent Micellization of PEO-PPO-PEO Block Copolymers in Aqueous Solutions by FT-Raman. *Langmuir* **1999,** *15* (8), 2703-2708.

16. Alexandridis, P.; Holzwarth, J. F.; Hatton, T. A., Micellization of poly(ethylene oxide)-poly(propylene oxide)-poly(ethylene oxide) triblock copolymers in aqueous solutions: thermodynamics of copolymer association. *Macromolecules* **1994,** *27* (9), 2414-2425.

17. (a) Hurter, P. N.; Scheutjens, J. M. H. M.; Hatton, T. A., Molecular modeling of micelle formation and solubilization in block copolymer micelles. 1. A self-consistent mean-field lattice theory. *Macromolecules* **1993,** *26* (21), 5592-5601; (b) Hurter, P. N.; Scheutjens, J. M. H. M.; Hatton, T. A., Molecular modeling of micelle formation and solubilization in block copolymer micelles. 2. Lattice theory for monomers with internal degrees of freedom. *Macromolecules* **1993,** *26* (19), 5030-5040.

18. (a) Linse, P.; Malmsten, M., Temperature-dependent micellization in aqueous block copolymer solutions. *Macromolecules* **1992,** *25* (20), 5434-5439; (b) Linse, P., Phase behavior of poly(ethylene oxide)-poly(propylene oxide) block copolymers in aqueous solution. *J. Phys. Chem.* **1993,** *97* (51), 13896-13902; (c) Linse, P., Micellization of poly(ethylene oxide)-poly(propylene oxide) block copolymers in aqueous solution. *Macromolecules* **1993,** *26* (17), 4437-4449; (d) Wijmans, C. M.; Linse, P., Modeling of Nonionic Micelles. *Langmuir* **1995,** *11* (10), 3748-3756.

19. Lam, Y.-M.; Goldbeck-Wood, G., Mesoscale simulation of block copolymers in aqueous solution: parameterisation, micelle growth kinetics and the effect of temperature and concentration morphology. *Polymer* **2003,** *44* (12), 3593-3605.

20. Yang, Z.-Z.; Qi, S.-F.; Zhao, D.-X.; Gong, L.-D., Insight into Mechanism of Formation of C8 Adducts in Carcinogenic Reactions of Arylnitrenium Ions with Purine Nucleosides. *J. Phys. Chem. B* **2008,** *113* (1), 254-259.

21. Lakowicz, J. R., *Principles of Fluorescence Spectroscopy*. Kluwer Academic/

Plenum: New York, 1999.

22. Croy, S. R.; Kwon, G. S., The effects of Pluronic block copolymers on the aggregation state of nystatin. *J. Controlled Rel.* **2004,** *95* (2), 161-171.

23. (a) Bednarek, J.; Plonka, A.; Pacewska, B.; Pysiak, J., Dispersive kinetics of solid thermolysis. Decomposition of basic aluminium ammonium sulphate. *Thermochim. Acta* **1996,** *282–283* (0), 51-60; (b) Kozlov, M. Y.; Melik-Nubarov, N. S.; Batrakova, E. V.; Kabanov, A. V., Relationship between Pluronic Block Copolymer Structure, Critical Micellization Concentration and Partitioning Coefficients of Low Molecular Mass Solutes. *Macromolecules* **2000,** *33* (9), 3305-3313.

24. (a) Dong, D. C.; Winnik, M. A., Dao Cong Dong and Mitchell A. Winnik. *Can. J. Chem.* **1984,** *62* (11), 2560-2565; (b) Wilhelm, M.; Zhao, C. L.; Wang, Y.; Xu,

R.; Winnik, M. A.; Mura, J. L.; Riess, G.; Croucher, M. D., Poly(styrene-ethylene oxide) block copolymer micelle formation in water: a fluorescence probe study. *Macromolecules* **1991,** *24* (5), 1033-1040.

25.   (a) Alexandridis, P.; Athanassiou, V.; Hatton, T. A., Pluronic-P105 PEO-PPO-PEO Block Copolymer in Aqueous Urea Solutions: Micelle Formation, Structure, and Microenvironment. *Langmuir* **1995,** *11* (7), 2442-2450; (b) Bohorquez, M.; Koch, C.; Trygstad, T.; Pandit, N., A Study of the Temperature-Dependent Micellization of Pluronic F127. *J. Colloid Interface Sci.* **1999,** *216* (1), 34-40.

26.   Latz, H. W.; Hurtubise, R. J., Luminescence analysis of food antioxidants; determination of propyl gallate in lard. *J. Agric. Food Chem.* **1969,** *17* (2), 352-355.

27.   Kasha, M., Collisional Perturbation of Spin-Orbital Coupling and the Mechanism of Fluorescence Quenching. A Visual Demonstration of the Perturbation. *J. Chem. Phys.* **1952,** *20*, 71-74.

28.   Alexandridis, P.; Alan Hatton, T., Poly(ethylene oxide)---poly(propylene oxide)---poly(ethylene oxide) block copolymer surfactants in aqueous solutions and at interfaces: thermodynamics, structure, dynamics, and modeling. *Colloids and Surf., A* **1995,** *96* (1-2), 1-46.

29.   Batsberg, W.; Ndoni, S.; Trandum, C.; Hvidt, S., Effects of Poloxamer Inhomogeneities on Micellization in Water. *Macromolecules* **2004,** *37* (8), 2965-2971.

30.   Wang, Q.; Yu, G.-E.; Deng, Y.; Price, C.; Booth, C., Eluent gel permeation chromatography: Application to the association of block copolymer F127 in aqueous solution. *Eur. Polym. J.* **1993,** *29* (5), 665-669.

31.   Yang, S.; Zhang, X.; Yuan, S., Mesoscopic simulation studies on micellar phases of Pluronic P103 solution *J. Mol. Modeling* **2008,** *14*, 607-620.

32.   Smith, G. D.; Bedrov, D., Roles of Enthalpy, Entropy, and Hydrogen Bonding in the Lower Critical Solution Temperature Behavior of Poly(ethylene oxide)/Water Solutions. *J. Phys. Chem. B* **2003,** *107* (14), 3095-3097.

CHAPTER THREE

KINETICS OF GOLD NANOPARTICLE FORMATION

FACILITATED BY TRIBLOCK COPOLYMERS

Abstract

Concerns for the environmental and economic impact of organic solvents and detergents in gold nanoparticle (AuNP) solution synthesis have motivated the search for more environmentally benign alternatives. One approach is to synthesize AuNPs from tetrachloroauric (III) acid ($HAuCl_4$) using triblock copolymers (TBPs). However, a major challenge of using TBPs is the heterogeneous nature of the formed nanocrystals. Establishing control over AuNP size and shape requires a detailed mechanistic understanding of precursor reduction and nanoparticle growth. By using mixtures of TBPs (L31 and F68), we demonstrate a more flexible method for adjusting the hydrophobic/hydrophilic environment to tune the size and shape. We show that AuNP morphology and size can be changed by adjusting the TBP/Au(III) ratio. Kinetic models are used to rationalize why the addition of L31 slows the rate of AuNP formation and growth. Experimental evidence of sigmoidal growth kinetics, early time bimodal gold nanoparticle size distributions and polycrystallinity suggest that aggregative AuNP growth is an important mechanism.

Abbreviations

AFM	Atomic force microscopy
AuNP	Gold nanoparticle
CP	Cloud point
CTAB	Cetyltrimethylammonium bromide
DPD	Dissipative particle dynamics
FESEM	Field emission scanning electron microscopy
FWHM	Full width half maximum
$HAuCl_4$	Tetrachloroauric (III) acid
$HAuCl_4.3H_2O$	Tetrachloroaurate (III) Hydrate
HMW	High molecular weight
KJMA	Kolmogorov-Johnson-Mehl-Avrami
LMCT	Ligand-to-metal charge transfer
LMW	Low molecular weight
LSPRs	Localized surface plasmon resonances
PEG	Polyethylene glycol
PEO	Poly-ethylene oxide
PPO	Poly-propylene oxide
PVDF	Polyvinylidene fluoride
SERS	Surfance-enhanced Raman scattering
STEM	Scanning transmission electron microscopy
TBP	Triblock copolymers
XRD	X-ray diffraction

Introduction

An important challenge in materials chemistry is to understand how the properties of nanomaterials scale with physical dimension because different physico-chemical properties vary in distinct ways with shape and size.[1] Various anisotropic gold nanoparticles (AuNPs) have attracted much attention due to their ability to maximize electromagnetic-field enhancement which finds applications in surface-enhanced Raman scattering (SERS) detection and other spectroscopic fields.[1e, 2] The local interactions between plasmonic nanoparticles and electromagnetic wave radiation are described by localized surface plasmon resonances (LSPRs) which are charge density oscillations that produce intense local electric fields within a few nanometers of the particle's surface.[3] This effect can increase Raman scattering cross-sections of molecules adsorbed on the surface.[1c] The shape dependence of this phenomenon can be exploited to tailor the spectral response by controlling the topology of the nanoparticles.[4]

Solution based synthesis of AuNPs typically involves the reduction of precursor gold ions.[5] The synthesis of anisotropic AuNPs in solution requires that nucleation and growth deviate from a thermodynamic to a kinetically controlled pathway by slowing down precursor decomposition or reduction via a weak reducing agent or by Ostwald ripening.[6] A common approach to anisotropic nanoparticle synthesis is the seed methodology where a small amount of gold precursor is added to a solution. This method has been used to synthesize nanoprisms.[7] It has been shown that triangular/hexagonal and smaller pseudo-spherical AuNPs can be synthesized from $HAuCl_4$ using salicylic acid,[8] aspartic acid,[9] UV-vis irradiation,[10] gamma irradiation in a reaction medium containing

gold (I), and ascorbic acid in the presence of cetyltrimethylammonium bromide (CTAB).[11]

The LaMer mechanism[12] (classical nucleation and growth) is commonly used to describe the growth of nanoparticles.[13] This mechanism supposes a burst of nucleation producing a number of nuclei viable for growth. After initial nucleation, the nuclei grow into particles by the molecular addition of nutrient species on the surface of the particles known as Ostwald ripening. In this model, the particles will be mostly monodisperse. This classical model of nucleation burst has been challenged in the case of citrate reduction where the polydispersity and size are influenced by pH, temperature and concentration of the reducing agent.[14] Furthermore, it has been noted that the LaMer mechanism does not account for the aggregation of small nanocrystallites.[15] An alternative model called the aggregative nanocrystal model has been used successfully to describe Au nanocrystal growth.[14c, 15] In this model, the initial nucleation and growth result from a number of critically sized aggregates of smaller nanocrystallites in a *non-classical* aggregative nucleation step.[15] Nanoparticle growth is then achieved by the coalescence of these aggregates and is characterized by polycrystallinity of the developing particles,[15-16] bimodal size distributions in the early stages of growth[15, 17] and sigmoidal growth kinetics.[15, 18]

Concerns for the environmental and economic impact of organic solvents and detergents such as CTAB have motivated the search for more environmentally benign alternatives.[19] Recently, several groups have reported the use of nontoxic TBPs that allow the single-step formation of AuNPs.[20] Triblock non-ionic copolymers contain blocks of poly-ethylene oxide (PEO) and poly-propylene oxide (PPO) in the sequence PEO-PPO-

70

PEO and are known as poloxamers or commercially as Pluronics. These TBPs reduce the hydrogen tetrachloroaurate (III) hydrate (HAuCl$_4$.3H$_2$O) into AuNPs and subsequently suspend and stabilize them in solution. It has been shown that the size of the gold nanocolloids can be controlled on the basis of the structures of amphiphilic block copolymers.[20c, d, 21] For example, Alexandridis and coworkers used TBPs in synthesis of AuNPs[21a, 21c, 22] and Khullar *et al.*[20c] studied the micellar TBPs F68 and P103 in reducing HAuCl$_4$. The latter study also examined the effects of temperature when comparing hydrophobic and hydrophilic TBPs. The conditions used in the Khullar study involved isotropic micellar behavior as is shown in the F68-water phase diagram.[23] They proposed that the extent of hydration of the surface cavities is the rate-determining step and that the mechanism of Au(III) reduction involves sequential redox reactions on the surface of the PEO ether backbone. Their findings indicate that particle size could be controlled by varying EO/PO ratio, solvent, and temperature. In addition they noted that the shape can be influenced by the HAuCl$_4$ concentration.

The major challenge of using the TBP mediated approach to synthesize AuNPs is the heterogeneous nature of the formed nanocrystals.[21-22] Furthermore, establishing control over AuNP size and shape requires a detailed understanding of the mechanism and kinetics of precursor reduction and particle growth.[14b] We demonstrate a more flexible method for adjusting the hydrophobic/hydrophilic environment in order to control the growth kinetics of the AuNPs by using mixtures of TBPs. Our method involves mixtures of low molecular weight (LMW) hydrophobic (PO: EO ratio > 0.5) and high molecular weight (HMW) hydrophilic (PO: EO ratio <0.5) PEO-PPO-PEO block co-polymers. We show that the yield of nanoprisms can be manipulated via

changes in gold and surfactant concentrations. We also show that the growth kinetics can be more adequately described by an aggregative nucleation and growth model. The uniqueness of our approach is that we can modify the kinetics of particle growth and morphology through optimizing the phase behavior of aqueous block copolymers mixtures.

Materials And Methods

Materials

The Pluronics® L-31 (EO$_2$-PO$_{16}$-EO$_2$ MW $\approx$ 1100; Batch #: 01631MH), and F68 (EO$_{78}$-PO$_{30}$-EO$_{78}$ MW $\approx$ 8400; Batch #: 018K0029) along with hydrogen tetrachloroaurate (III) trihydrate (HAuCl$_4$.3H$_2$O) were used as received (Sigma Aldrich, Milwaukee, WI, USA). Water was purified with a Milli-Q (18 MΩ cm) water system.

Synthesis of Gold Nanostructures

The cloud point (CP) of stock L31/F68 mixtures can be reduced from above 100°C for aqueous F68 binary mixtures,[24] to $\approx$ 30°C by adding L31 (Figure 3.1). In a typical stock solution preparation, 10 mL of 50% w/v F68 and 10 mL L31 were added to 100 mL water (8 mM:4 mM; L31/F68). This mixture corresponds to an EO:PO molar ratio $\approx$ 0.7. Gold nanostructures were prepared by adding 2 to 5 x 10^{-2} M HAuCl$_4$ to the TBP aqueous polymer mixtures at the required dilutions followed by vigorous mixing for 10 seconds. HAuCl$_4$ reduction was performed at $\approx$ 25°C where the end-point was estimated by the plateau in the 540 nm UV-vis absorbance peak. For Au(III)

concentrations below 5 x 10^{-4} M the reaction was complete within 2-3 hours while at 1 x

10^{-3} M initial Au(III) concentration.
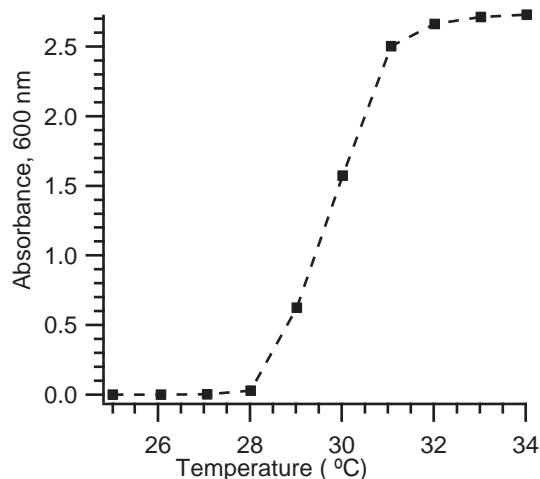
Figure 3.1 A plot of the absorbance at 600 nm against temperature for L31:F68 (8 mM: 4mM) 2:1 mixture. The inflection point gives an estimate of the CP.

The reaction was complete within 12 hours. In UV-vis experiments $HAuCl_4$ was

added to 1 mL of L31/F68 aqueous solutions followed by 10 cuvette inversions to

thoroughly mix the reagents. For longer studies of two or three days (Figures 1 and 2), we

incubated the mixtures in a water bath at 25°C before characterization by UV-vis

spectroscopy and electron microscopy to ensure that $HAuCl_4$ reduction was complete.

Synthesis of Au Citrated Seeds

Citrated gold nanoparticles, between ~10-30nm, were prepared by refluxing 150

mL of 2.2 mM sodium citrate aqueous solution in a three-necked round bottom flask for

15 min as previously described.[25] Then 1mL of 25 mM of $HAuCl_4$ was injected and

allowed to react, approximately 10 min., until the solution turned soft pink. A 5 mL

aliquot was removed and placed aside for further characterization. In the same vessel, the

reaction was cooled to 90°C and 4 mL of sodium citrate (15 mM) and 1 mL HAuCl$_4$

(25mM) were injected sequentially. After additional refluxing (30 min.), aliquots of 5 mL

were extracted and placed aside for further characterization. This process (injection of 4

mL of sodium citrate (15 mM) and 1 mL HAuCl$_4$ (25 mM)) was repeated until 14

generations of gold nanoparticles of progressively larger gold nanoparticles were

synthesized.

Synthesis of Seeded TBP Coated Gold Nanoparticles

The first (~6 nm), seventh (~16 nm), and fourteenth (~23 nm) generations of the

Au citrate nanoparticles were used to seed the growth of the polymer coated Au

nanoparticle. In a typical stock solution preparation, 10 mL of 50% w/v F68 and 10 mL

L31 were added to 100 mL water (8 mM:4 mM; L31/F68). 1 mL of L31/F68 solution

was seeded with 0-100 µL of Au citrate seed and incubated at 25°C for ~15 min before

1×10^{-3} M HAuCl$_4$ was added to the reaction and monitored for 15 min.

UV-vis/Dynamic Light Scattering (DLS)

The reduction of HAuCl$_4$ and the formation of gold nanoparticles were monitored

by observing the changes in the absorption spectra using a UV-vis spectrometer (Varian

Cary 300 and 500) fitted with temperature control at 25 ± 1 °C. The AuCl$_4^-$ concentration

was estimated from the absorption bands at 240 nm and 320 nm by the use of extinction

coefficients 9823 M^{-1}cm^{-1} and 5400 M^{-1}cm^{-1}, respectively.[26]

Turbidity measurements were taken via the absorbance of the mixtures using a Cary 300 UV-vis spectrometer at $\lambda = 600$ nm. DLS experiments measurements were made with a model NICOMP 370 submicron particle sizer (Particle Sizing Systems, Santa Barbara CA, USA) at a He-Ne laser wavelength of 632 nm with a power output of 60 mW. For DLS measurements, samples were centrifuged (10,000 rpm) to remove excess surfactant and suspended in water.

Gold Nanoparticle Characterization

Samples were prepared for electron microscopy measurements by centrifuging (10,000 rpm) twice to remove excess polymer and suspended in water. Field emission scanning electron microscopy (FESEM) analysis was carried out on a Zeiss Gemini FIB/FESEM instrument with scanning transmission electron microscopy (STEM) capabilities (at an operating voltage of 20 kV). Digital TEM images were obtained using a Philips Tecnai 12 instrument operating at 80 kV and fitted with a Gatan camera. The samples were prepared for TEM and STEM by mounting a drop of a solution on a carbon-coated Cu grid (Ted Pella 200 mesh) and allowed to dry in the air.

Atomic force microscopy (AFM) images were generated with a Multimode 8 scanning probe microscope (Bruker, Santa Barbara CA) in the peak force^{TM} tapping mode and using ScanAsyst^{TM} ($k = 0.4$ Nm^{-1}, $f = 70$ kHz) air probes. Automated feedback parameter optimization was achieved using ScanAsyst^{TM}. The peak force^{TM} tapping mode modulates the cantilever at *ca* 2 kHz at each pixel of the image where the feedback is based on the interaction force each time the tip taps the sample.

To image nanoprisms, 1 mL aliquots of the reaction mixture were filtered using 0.1 μm polyvinylidene fluoride (PVDF) membrane (Millipore) centrifuge tubes in order to remove particles smaller than 100 nm which include the spherical gold particles and smaller gold prisms. After filtration, the retentate was collected by adding 1 mL water and sonicating for 20 seconds. A 5 μL aliquot of the retentate was placed upon a gold coated mica sheet (10 mm x 10 mm) to dry prior to AFM imaging. X-ray diffraction (XRD) was performed with a Siemens D500 diffractometer.

Sample preparation for AFM imaging of the primary nanocrystallites was performed by taking 100 μL aliquot of a reaction mixture at different times after Au(III) addition and adding this aliquot to 900 μL of water. This slows the reaction rate so that it is negligible on the time-scale of sample preparation. A 1 mL solution was centrifuged at 13,000 rpm for 5 minutes. Then a 5 μL aliquot of this solution was dropped onto a freshly cleaved mica surface and allowed to dry. The mica surface is washed to remove excess polymer by dropping ~10-20 μL of water on the dried spot and allowing the water to drain onto a dry cloth. AFM post-acquisition image processing and analyses were performed using Nanoscope Analysis by Bruker, ImageJ (http://rsbweb.nih.gov/ij), and Gwyddion (http://gwyddion.net/) software suites.

Analysis of Growth Kinetics

AuNP growth was monitored using the 540 nm UV-vis peak. The Kolmogorov–Johnson–Mehl–Avrami (KJMA) model has been shown in some cases to fit the sigmoidal nanoparticle growth profile.[14c, 15] However, we found that the simple KJMA model was unable to fit the rising slope at later times. Instead, a modified logistic equation that

includes a second term to account for Ostwald ripening provided a reasonable fit to the data.[18a] The absorbance, $A(t)$, being proportional to the volume fraction data was fitted by a modified exponential function.[14c, 18a]

$$A(t) = c(1 - e^{-k_g t^n}) + \frac{b(t - t_{OR})}{1 + e^{-w(t - t_{OR})}}$$

(1)

This equation consists of two terms having proportionality constants c and b. The first term is the standard KJMA term to fit nucleation and growth, where k_g (min^{-1}) is a rate parameter and n is the Avrami exponent. The rate constant, k_g, is considered an indicator of the relative growth rates.[15] The second term provides a linear increase in mean volume to account for Ostwald ripening.[18a] The rate parameter, b, is multiplied by a logistic function to activate Ostwald ripening at time, t_{OR}. The width of the turn on function, w, was set to unity. We note that values of w greater than unity (e.g., 2 minutes) did not statistically improve the quality of the fitting. The Ostwald ripening onset time, t_{OR}, of the second growth regime was estimated visually or by plotting the derivative of the absorbance against time. The time, t_{OR}, was estimated from the sum of the position of the peak maximum and half of the full width at half maximum (FWHM). We found that the latter approach was useful at initial Au(III) concentrations above 2×10^{-4} M where the sloping background prevents clear visual designation of the Ostwald growth regime (Figure 3.3). Initial guesses for c, k_g and n were obtained by fitting the first term in equation 1 up to t_{OR}. These parameters were used as initial guesses of the least-squares fit

of equation 1, with the parameter, t_{OR}, fixed. Peak fitting and post-acquisition spectral analysis was done using Igor Pro (Wavemetrics) and mathcad 15 (PTC).

Results

Gold Nanoparticle Characterization

UV-vis Spectroscopy

Figure 3.2 shows spectra with initial Au(III) concentrations between 1 x 10^{-3} and 1 x 10^{-5} M. Figure 3.2A is in 4.5 mM F68 solutions and Figure 3.2B is in L31/F68 (8 mM: 4 mM) solutions. Spectra were not recorded above 1400 nm because of the strong water absorption above 2 μm.[27] The observation of peaks associated with the Au(III) salt at 10^{-3} M indicates a limiting condition in the number of reducing PEO equivalents. The estimated 240 nm reduction in absorbance of ~ 10 to ~ 2 represents a 5-fold change of ~ 80% Au(III) reduction.

The transitions above 500 nm are due to the LSPR bands of gold while the peaks below 400 nm (216 nm and 320 nm) are assigned to ligand-to-metal charge transfer (LMCT) ($\pi \rightarrow \sigma^*$) Cl $p_\pi \rightarrow$ 5d $_{x^2-y^2}$ bands of the various chlorohydroxoaurate species $AuCl_xOH_{4-x}^-$ that may be present depending on the solution pH.[28,29]

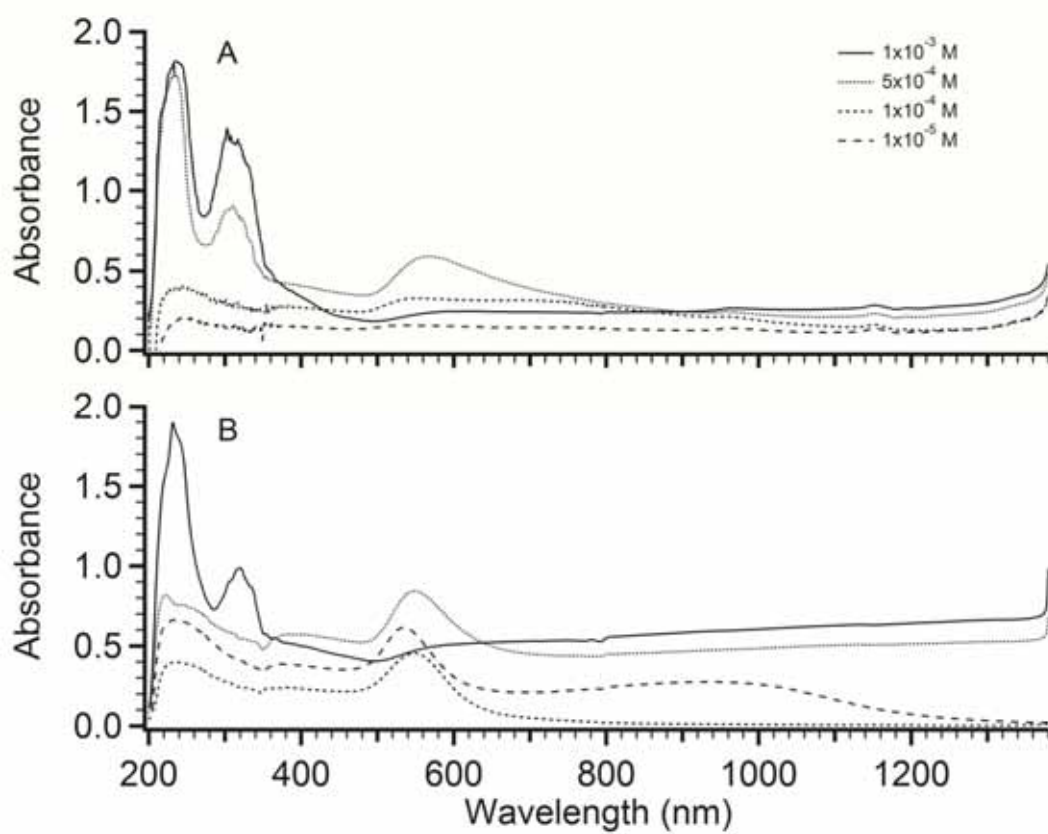Figure 3.2 UV-vis spectra of samples incubated at 25°C for two days with initial Au(III) concentrations between 1 x 10^{-3} and 1 x 10^{-5} M. The polymer concentrations are (A) 4.5 mM F68; and (B) L31/F68 (8 mM: 4 mM).
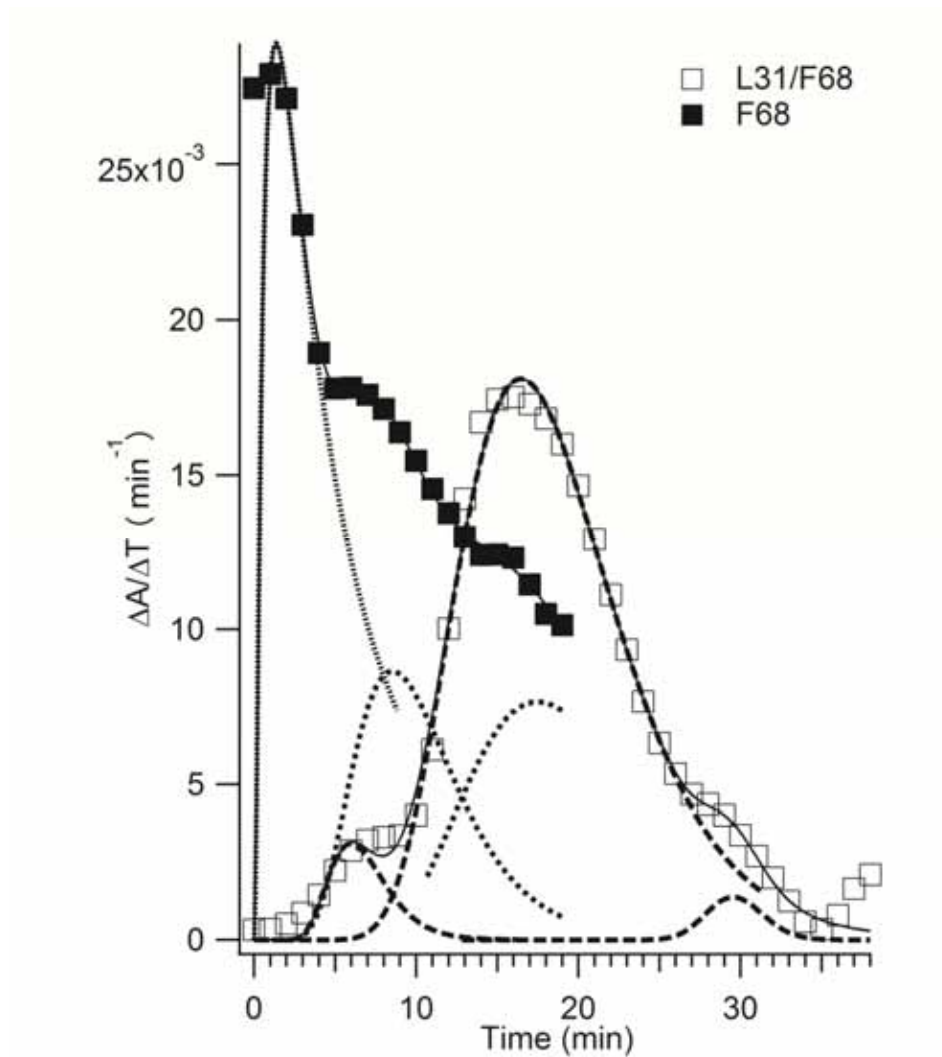
Figure 3.3 Example plot of 10^{-4} M initial Au(III) concentration of the first derivative of the absorbance. The white and black squares are the L31 4.5 mM and L31/F68 8 mM/4 mM solutions, respectively; the dotted and solid lines are the Gaussian single peak and composite fits to the data, respectively. We can estimate Ostwald ripening time, t_{OR}, in equation 1 from the sum of the position of the peak maximum and half of the full width at half-maximum (fwhm) of the first Gaussian peak.

Khullar *et al.*[20d] observed a peak at 290 nm in L64 aqueous solutions that was red-shifted with increasing solution temperature to 320 nm for Au(III) reduction. This red-shift was attributed to the energy relaxation caused by the structural reorganization in the copolymer aggregates. Aqueous $AuCl_4^-$ solutions exhibit peaks at 217 and 287 nm (Figure 3.4). Thus it is likely that any red-shift to $\approx$ 320 nm upon $AuCl_4^-$ addition to TBP solutions is due to the hydrogen bonding interactions of TBPs with water that will reduce the extent of water solvation around $AuCl_4^-$ and the subsequent rate of Au-Cl substitution by OH^-.

At 1×10^{-3} M initial Au(III) concentration, the longer wavelength 700 – 1400 nm intensities are assigned to in-plane dipole and out-of-plane quadrupole resonance absorptions of nanoplates.[30] Both experimental[7a, 31] and theoretical[30a,30b] results show linear correlations between increasing resonance absorption band wavelengths and the edge lengths of gold nanoplates. Larger nanoplates with sizes comparable to the excitation wavelength will have a greater scattering contribution to absorption than small nanoparticles. Moreover, the absorbance intensities above 700 nm are the highest for L31/F68 solutions at 25°C (Figure 3.2B), which is double for L31/F68 than F68 alone (Figure 3.2A). This infers that the average edge lengths of the gold nanoplates in the L31/F68 aqueous mixture are larger compared to those in the F68 aqueous mixture. At lower Au (III) concentrations ($< 5 \times 10^{-4}$ M), the higher intensities in the ~ 540-600 nm region relative to absorption above 700 nm indicate smaller nanoparticles below 50 nm. We note that solutions of L31 did not reduce Au(III) below 70°C which is consistent with previous work.[20d]
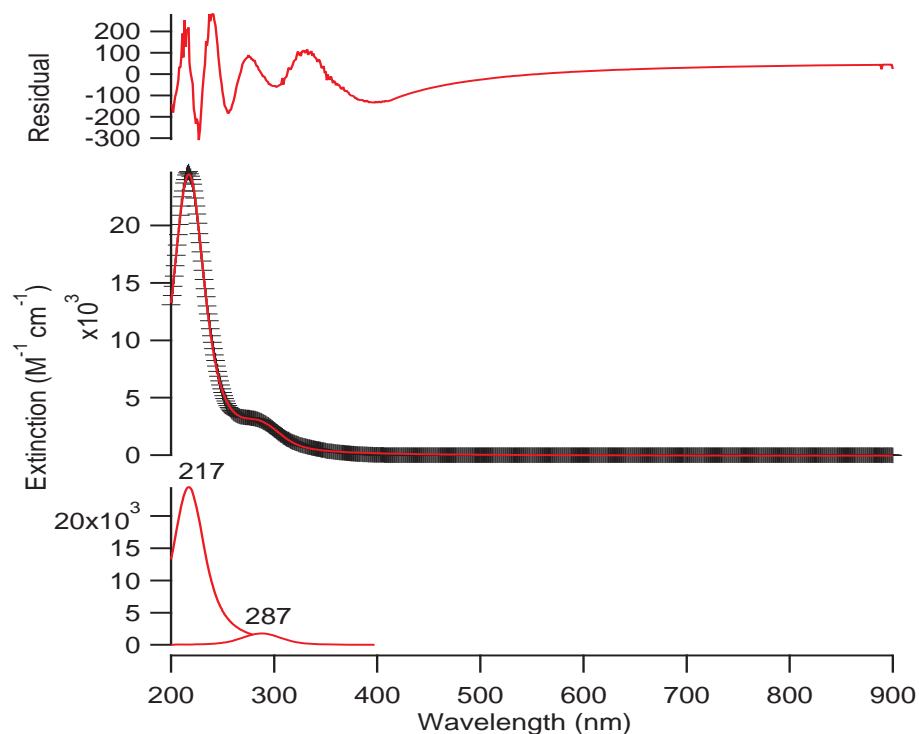
Figure 3.4 The measured UV-vis spectrum of the <u>extinction coefficient</u> of Au(III) in DI water at room temperature. The extinction coefficient was determined by using solutions at different Au (III) concentrations. (A) Residual of the Gaussian fits. (B) Fitted and measured spectra. (C) Deconvoluted peaks at 217 and 287 nm.

Dynamic Light Scattering

Measurements taken with DLS confirm the smaller average particle sizes for

Au(III) reduction in aqueous F68 (~ 300 nm) versus L31/F68 (~ 1400 nm) solutions

(Figure 3.6). This is consistent with the higher absorbance background above 700 nm

associated with larger nanoplates in the L31/F68 mixture. We note that DLS gives a

qualitative measure of the relative sizes because the standard DLS model assumes

spherical particles and the absence of multiple elastic scattering.[32]

FESEM

Figure 3.5A and B show representative FESEM images of the formed gold nanostructures which were characterized by UV-vis spectroscopy (Figure 3.2) with initial Au(III) concentration 1 x 10^{-3} M. The nanoparticles prepared from Au(III) reduction in an aqueous F68 mixture consists of a heterogeneous mix of irregular and nanoprism shaped nanoparticles on a length scale of 0.1 – 3 μm (see STEM Figure 3.7). Nanoplates are formed from Au(III) reduction in L31/F68 aqueous mixtures (Figure 3.5B). The plates are dominated by distinctive triangular and hexagonal shapes several microns in length interspersed with smaller plates and irregular icosahedral shaped nanostructures below 500 nm (see STEM/FESEM Figure 3.8). Figure 3.5C and D show that with 10-fold lower (10^{-4} M) Au(III) concentration sub 50 nm Au nanoparticles are formed, which are embedded within the polymer matrix. Our results are similar to published results at 40°C where TEM shows small Au nanoparticle aggregates embedded within the F68 polymer matrix.[20c]
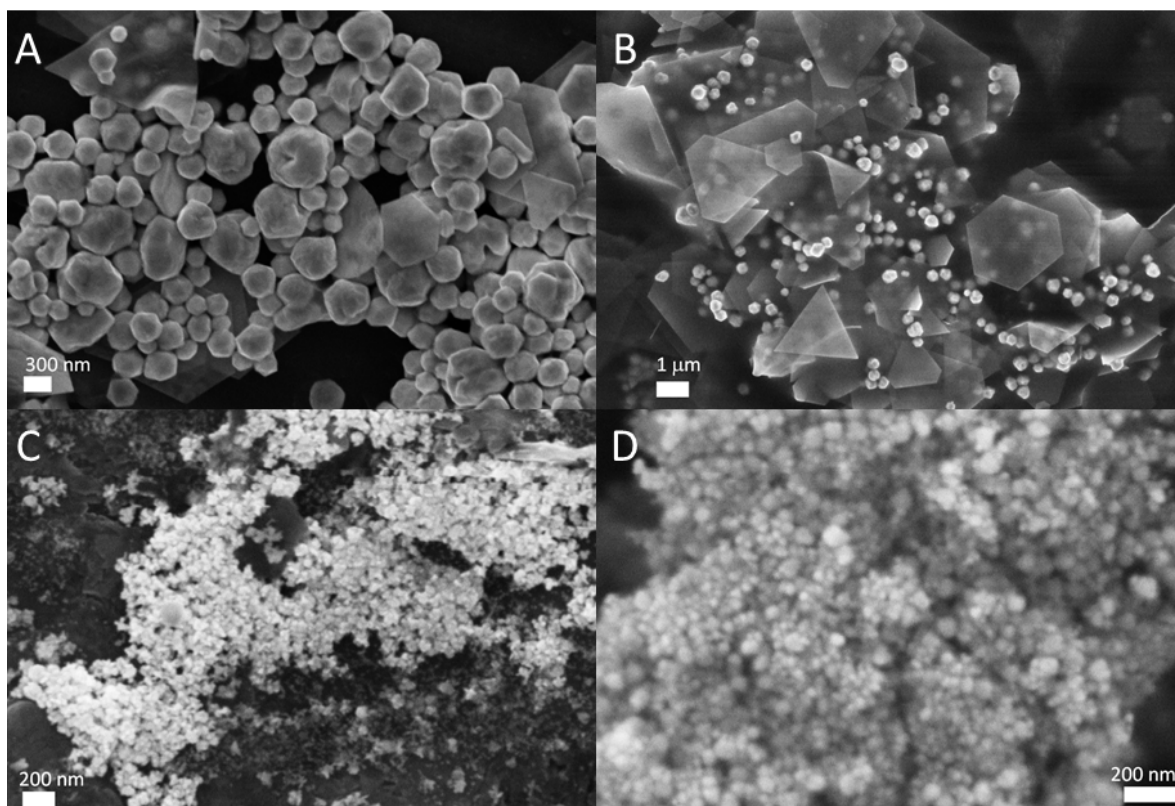
Figure 3.5 FESEM images (A) – (B) after three day incubation at 25°C with 1×10^{-3} M initial Au (III) concentration; (A) 4.5 mM F68 and (B) L31/F68 (8 mM: 4 mM) solutions. FESEM images (C) – (D) after three day incubation at 25°C with 1×10^{-4} M initial Au(III) concentration; (C) 4.5 mM F68 and (D) L31/F68 (8 mM: 4 mM) solutions.

(A)
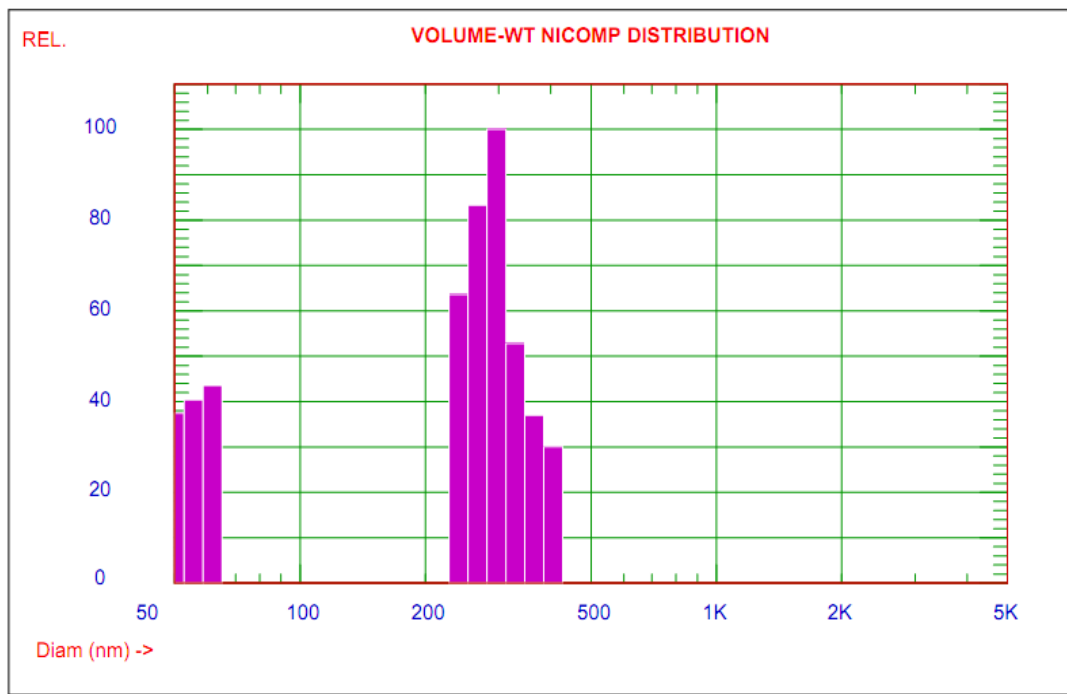
(B)
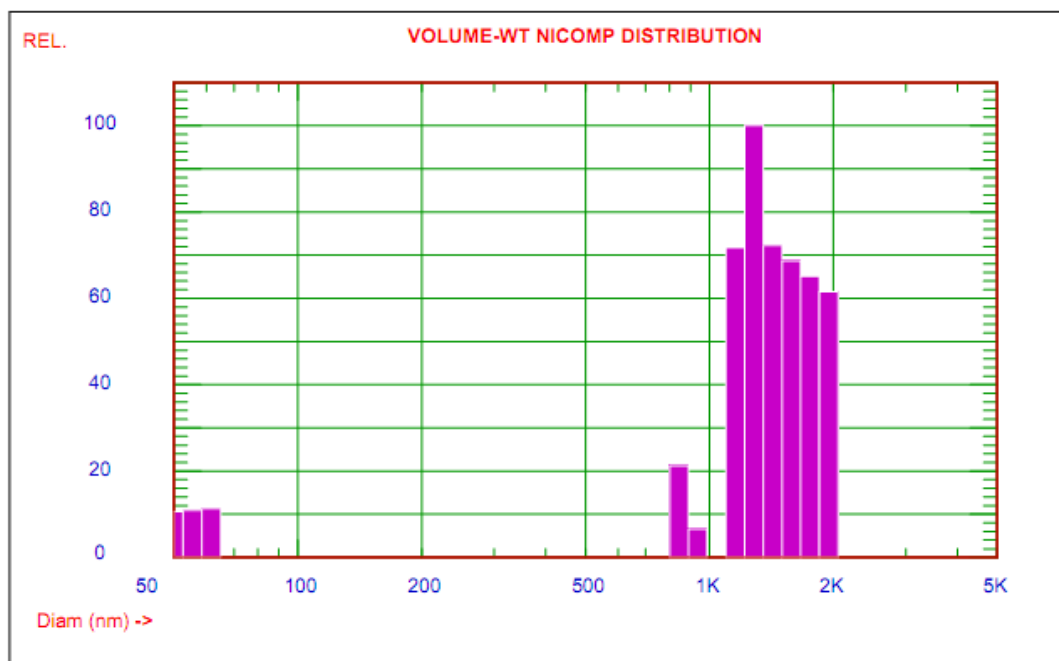
Figure 3.6 DLS volume-WT distribution for initial 10^{-3} M Au(III) concentration after 3 days. (A) F68 ≈ 4.5 mM; and (B) L31:F68/(8 mM: 4 m,M) mixtures.

Figure 3.7 STEM image with initial 10^{-3} M Au(III) concentration after 3 days for F68 ≈ 4.5 mM aqueous solution.

A)

B)

Figure 3.8 (A) STEM image with initial 10^{-3} M Au(III) concentration after 3 days for L31:F68/(8 mM: 4 mM) aqueous solution. (B) FESEM image of Au nanoprisms with initial 10^{-3} M Au(III) concentration reduced in a L31:F68/(8 mM: 4 mM) aqueous solution.
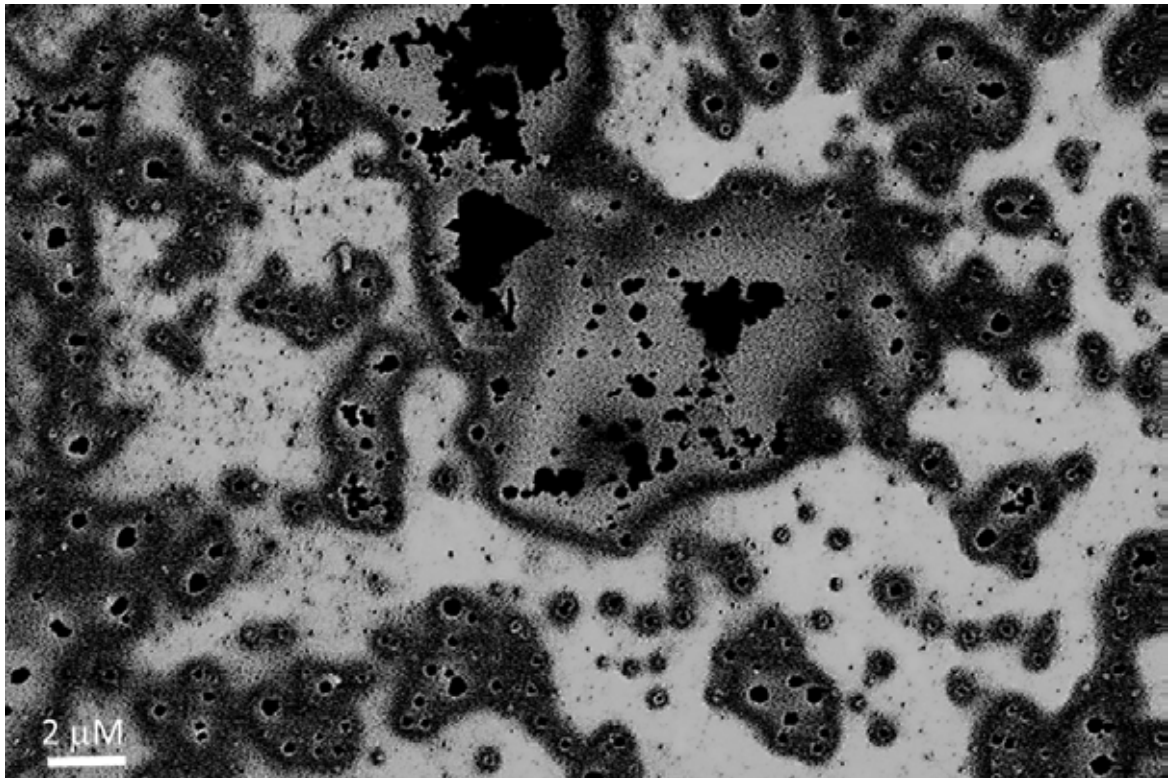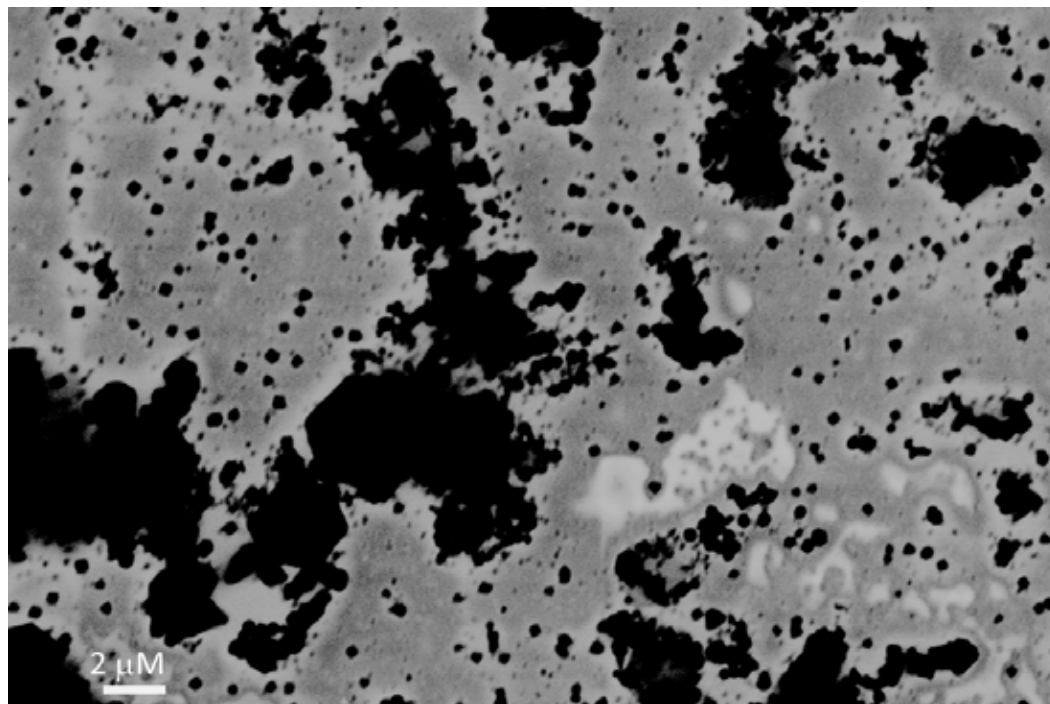
Atomic Force Microscopy

Figure 3.9A is a representative AFM image of a gold nanoplate step-edge. The measured thicknesses of the plates ranged from 15 to 25 nm. Some of the nanoplates had multiple step heights. Figure 3.9B shows an example of a nanoplate edge with step heights of 20 nm and 25 nm, respectively. Dotted on the surface of the nanoplates are bright features (Figure 3.9A and C) which we assign to absorbed TBP coated AuNPs. The X-ray diffraction (XRD) pattern of these nanoplates have (111) and (200) peaks characteristic of face-centered cubic structures (Figure 3.11). The dominance of the (111) peak indicates that the plates have {111} terraces.

Au(III) Reduction and TBP mediatednNanoparticle Growth Kinetics

The time evolution in the nanoparticle growth process was monitored by UV-vis spectroscopy of the Au(III) absorption peaks (Figure 3.10). Figure 3.10A shows example spectra (EO: PO ratio = 0.7) within 30 minutes of Au(III) addition. Upon the addition of Au(III) to the TBP mixture, the LMCT peak at 220 nm blue-shifts to 211 nm along with the concomitant resolution of the 245 nm peak and the appearance of LMCT peaks at 316 and 387 nm (Figure 3.10B). The origin of the additional 387 nm peak may be due to the reduction in the energy gap between $2e_u$ (π) $\rightarrow$ $2b_{1g}$ (σ^*) orbitals[33] caused by the complexation by the π-donor oxygen lone pairs of the PEO segments. We note that in the case of polyethylene glycol (PEG) a similar peak is observed at ~ 380 nm after 1 minute reaction.[34]

Figure 3.10C and D show the time evolution of 240, 320 and 540 nm peaks. There

is intensity loss for the 240 and 320 nm peaks. The 240 nm absorbance reaches a steady

state of 0.45 after 4 minutes (Figure 3.10C).
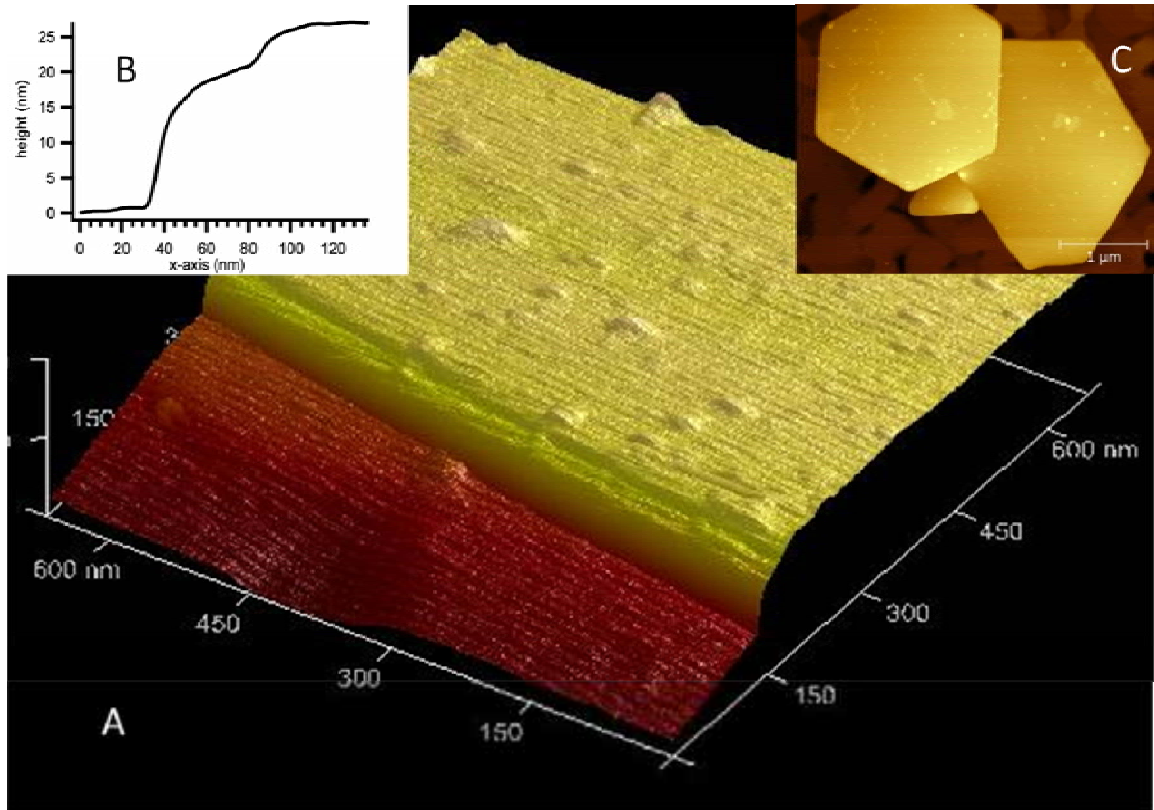
Figure 3.9 Representative AFM images of Au nanoplates (A)-(C); (A) nanoplate step-edge and; (B) the line profile of the nanoplate step-edge shown in (A). (C) An example AFM image of nanoprisms having dimensions of the order 1 μm.
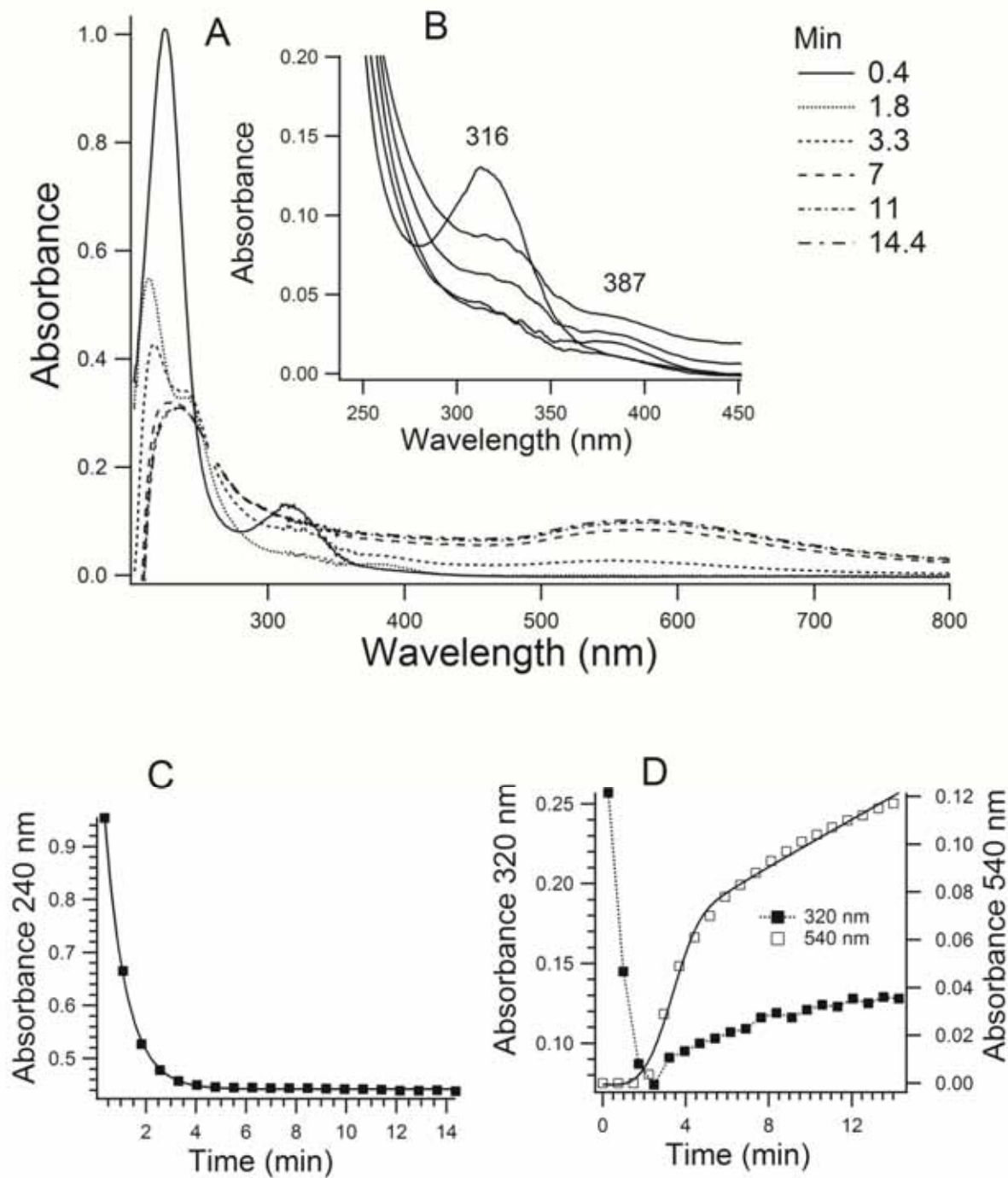
Figure 3.10 (A) Time evolution (15 minutes) UV-vis spectra of a L31/F68 8 mM: 4 mM F68 mixture with initial 10^{-4} M Au (III) concentration. (B) The evolution of the 316 and 387 nm peaks within the first 5 minutes of Au(III) addition. (C) Time evolution of the 240 nm peak. The first-order decay constant from the fit (solid line) is (1.95 ± 0.05) x 10^{-2} s^{-1}. (D) Time evolution in the 320 and 540 nm peaks. The solid line is the fit of equation 2 with n = 3; k_g = (8.1 ± 1.0) x 10^{-3} min^{-1}; t_{OR} = 8.02 ± 1.75 min.
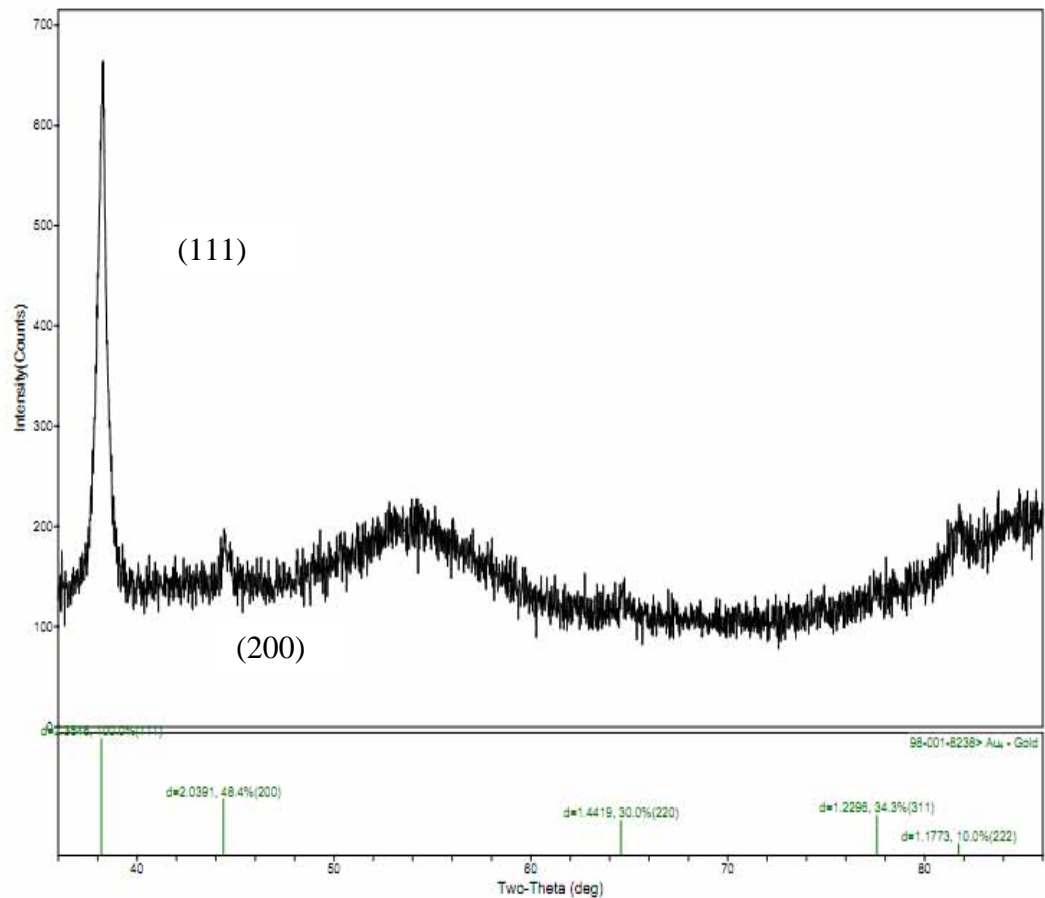
Figure 3.11 XRD spectrum for AuNPs made from an initial 10^{-3} M Au(III) concentration after 3 days in a of a solution of L31:F68 (8 mM: 4 mM).

The increase in the 320 nm peak intensity after 5 minutes is caused by the Au nanoparticle scattering contribution. Moreover, this 320 nm absorption increase correlates with the end of the induction period seen in the Au 540 nm surface plasmon peak.

Kinetics of Gold Nanoparticle Formation

An example of the effect of Au(III) concentration on the rate, R_{NP}, of nanoparticle formation is shown in Figure 3.12. This plot is constructed from the initial rate of loss in the 320 nm peaks. A comparison of ternary F68 + water + $HAuCl_4$ and quaternary L31/F68 + water + $HAuCl_4$ solutions show that the maximum rate is lower for L31/F68 mixtures. It is thought that the reduction of Au(III) proceeds via the oxidation of ethylene oxide groups in a pseudo-crown ether complex with $AuCl_4^-$ where the reduction of Au(III) follows the sequence Au(III) →Au(II)→Au(I) →Au(0).[21b, 34] The rate determining step is the reduction of Au(I)[34] ions which can migrate into micellar cavities resulting in disproportionation [$3\ Au(I) \longleftrightarrow 2\ Au + Au(III)$],[21a] followed by metal atom coalescence forming Au nanoclusters to yield primary nanocrystallites. Our observation that the maximum rate decreases when L31 is added suggests that the function of L31 is to inhibit the overall reduction rate of the Au(III). Based upon these observations, we constructed a kinetic model that is analogous to the Michaelis-Menten enzyme kinetics of mixed inhibition where the substrate is Au(III) and the active sites are the EO_x blocks of F68 (the derivation is found elsewhere).[35] In this model, L31 binds to F68 (L31:L68) and Au(III):F68 complexes to inhibit the reduction of Au(III). We show that R_{NP} is proportional to [Au(III)] and therefore $-R_{Au(III)}$ is proportional to Au(III) concentration.
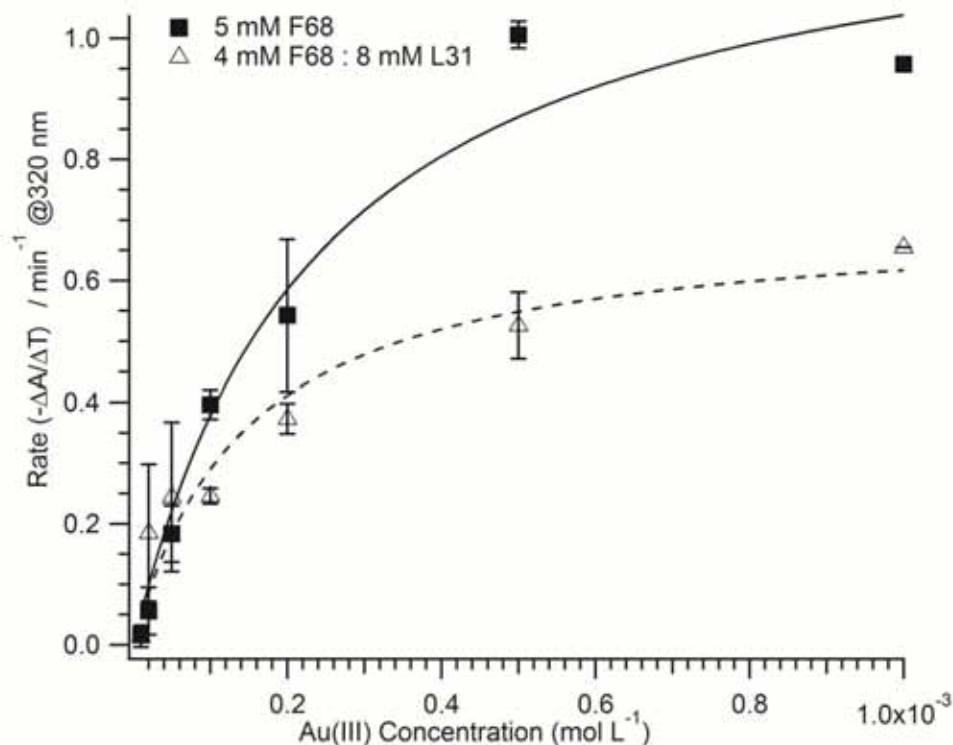
Figure 3.12 Rate of initial Au(III) loss (320 nm) against initial Au(III) concentration. The solid (—) and dashed (- -) lines are the fits to equation 2. Black squares are the initial rates in the 5 mM F68 and the open triangles are the initial rates for 4 mM F68: 8 mM L31 solutions. Least-squares fitting determined the values for R_{max} and K_m to be 0.01 Ms^{-1} and (2.4 ± 0.7) x 10^{-4} M, respectively. The calculated scaling parameters α and α' are $\approx$ 1.1 and $\approx$ 1.8 for the L31/F68 mixture giving values of $K_i =1.25\ K_m$ and $K_i' =10\ K_m$.

The initial rate of loss in the 320 nm peak is proportional to the rate of AuNP formation $(-R_{Au(III)} \propto R_{NP})$. The inhibition mechanism by L31 is assumed to occur by its interstitial occupation of micellar corona sites preventing the pseudo-crown conformations[21a, b] necessary for gold ion reduction.

This mixed inhibition process of Au(III) reduction can be modeled with a possible reaction mechanism shown in scheme 1 where F68 forms an equilibrium complex with Au(III) with a dissociation equilibrium constant of K_m. Meanwhile, the L31 interacts with

F68 (competitive inhibition) as well as complexing with F68:Au(III) (non-competitive

inhibition) with dissociation constants of K_i and K_i', respectively. The AuNP reaction

rate, R_{NP}, is

$$R_{NP} = \frac{R_{max}[Au(III)]}{\alpha \cdot K_m + \alpha'[Au(III)]} \qquad (2)$$

Here, the α term accounts for the competitive inhibition by L31 for F68 active sites and

α' for its noncompetitive inhibition when it interacts with the F68:Au(III) complexes

inducing conformational changes in the PEO backbone preventing redox reactions. In the

absence of L31, the terms α and α' are equal to one. The term R_{max} is the reaction rate in

the limit of high Au(III) concentration ([Au(III)] $\gg K_m$).

In this model, K_m, is the concentration at which the reaction rate is one-half R_{max}

and in the case of competitive inhibition by L31 is given by $\frac{K_m}{\alpha}$. In noncompetitive

inhibition by the L31, the maximum reaction rate is given by $\frac{R_{max}}{\alpha'}$. At the limit of high

Au(III) concentration, the reaction rate is $\frac{R_{max}}{\alpha'}$ and so the maximum rate will always be

less when L31 is present. In the high Au(III) concentration limit, varying the L31

concentration will have the most influence upon the reaction rate. In the low Au (III)

concentration limit, $R = \frac{R_{max} \cdot [Au(III)]}{\alpha \cdot K_m}$ provided that $\alpha K_m \gg \alpha'$[Au (III)]. Thus,

varying the Au(III) concentration will have the most influence upon the reaction rate. In

these two limiting concentration regimes, our model predicts that reaction conditions may

be optimized to maximize the yield of different Au NP sizes and shapes.

A relative measure of the reaction process number per unit time is the turnover number, k_{cat}, which is equal to $\frac{R_{max}}{[F68]}$ (min^{-1} or s^{-1}). The corresponding reaction time is equal to $\frac{1}{k_{cat}}$ and in the presence of L31, k_{cat} will be smaller resulting in longer reaction times. The ratio $\frac{k_{cat}}{K_m}$ ($M^{-1}s^{-1}$) is the effective second-order rate constant for the reduction between Au(I) and EO_x blocks of F68 as it is the rate determining step. This ratio is a quantitative measure of the reaction efficiency.

We determined the values of K_m and R_{max} from the F68 plot assuming α and α' are 1. The fitted value of K_m is (2.4 ± 0.7) x 10^{-4} M. The measured scaling parameters α and α' are ≈ 1.1 and ≈ 1.8 for the L31(8 mM)/F68 (4 mM) mixture giving values of K_i =1.25 K_m and K_i' =10 K_m. The calculated turnover number of the F68, k_{cat} is $\approx 10^{-3}$ s^{-1}; the efficiency or effective rate constant, k_{cat}/K_m, is ≈ 4 $M^{-1}s^{-1}$. We can estimate the reaction time to be equal to $\sim 1/k_{cat}$, which is $\approx 10^3$ s or ≈ 17 minutes. In the presence of L31 with α' ~ 2 our model accounts for the observation that R_{max} will be reduced by half (Figure 3.12).

$$Au^{III}$$

$$EO_x \;\underset{K_m}{\rightleftharpoons}\; EO_x\!:\!Au^{III} \longrightarrow EO_x\!:\!Au^{I}$$

$$+$$

$$PO_y \quad\quad\quad\quad PO_y \quad\quad\quad\quad \big\downarrow k_4$$

$$K_I \quad\quad\quad\quad K_I' \quad\quad\quad\quad EO_x\!:\!Au^{III}+nAu$$

$$Au^{III}$$

$$EO_x\!:\!PO_y \longrightarrow PO_x\!:\!PO_y\!:\!Au^{III} \quad\quad\quad Au_n$$
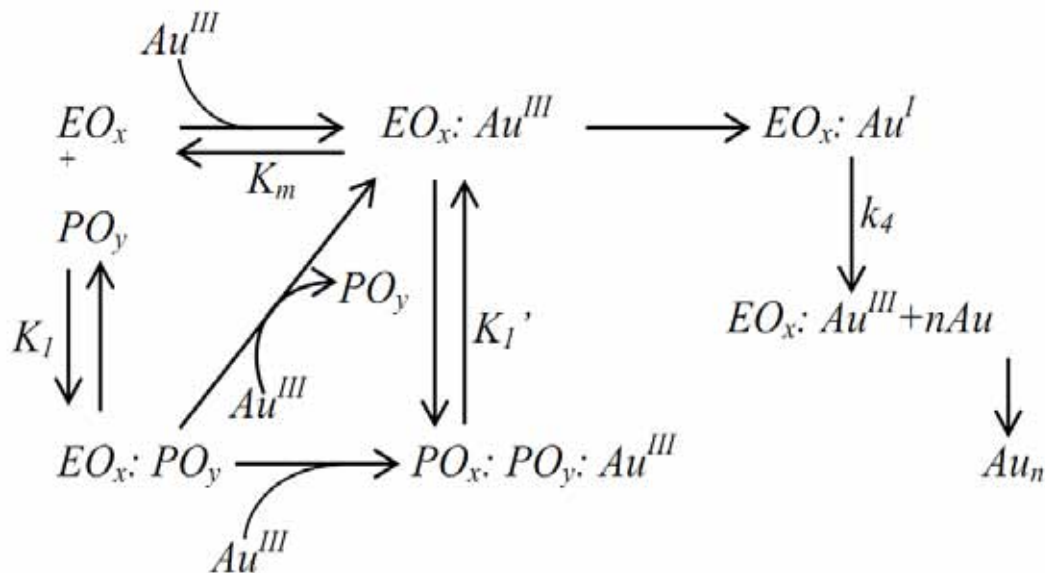
$$Au^{III}$$

Scheme 3.1 A proposed kinetic scheme of HAuCl$_4$ reduction by the EO$_x$ segments of F68. The equilibrium complexes EO$_x$:Au(III), EO$_x$:PO$_y$, and PO$_x$:PO$_y$:Au(III) are represented by the dissociation constants, K_m, K_I, and K_I' respectively.

In this kinetic model, the Au(III) reduction rate is proportional to the number density of the AuNP nanocrystal seeds. This correlates with the observation that AuNP size increases with higher Au/TBP ratio. In the limit of high Au(III) concentration the kinetics is pseudo-zeroth order. These primary nanocrystallites are between 1.5 – 2 nm in diameter (see Figure 3.15). At the limit of high Au(III) concentration, the number density of Au primary nanocrystallites will be higher in F68 than in L31/F68 aqueous mixtures. Based upon these arguments, it be expected that F68 solutions would grow larger AuNPs, which is not the case. Rather, the growth kinetics dominates where the extent of anisotropic growth is greater for L31/F68 quaternary mixtures. The presence of L31 serves likely to cap the AuNPs surfaces making growth along the edges the most probable mechanism. In contrast, for the Au(III) concentration linear regime ($< 2 \times 10^{-4}$ M), AuNP formation rates of F68 and L31/F68 are comparable within a 2-fold range.

This has implications for the growth phase, where at ~10^{-4} M Au(III) initial

concentration, both F68 and L31/F68 have similar primary nanocrystalline number

densities and K_m is of the order ~ Au(III) concentration. We observed mostly pseudo

spherical AuNPs (Figure 3.5C and D) as the case for initial 1 x 10^{-4} M Au(III)

concentration.

Kinetics of Gold Nanoparticle Growth

An example of the kinetic fitting using equation 1 within 15 minutes Au(III)

addition to F68 and L31:F68 mixtures is shown in Figure 6. The rate of AuNP growth is

slower for L31/F68 mixtures than for F68 alone. While the nucleation process of TBP-

facilitated Au(III) reduction occurs on a time-scale of seconds,[21b] nanoparticle growth is

detected in the UV-vis after an induction period of ~1 - 3 minutes (Figure 3.13).

Figure 3.13 (A) Plot of 10^{-3} M initial Au(III) concentration of the 540 nm absorbance and L31 (8 mM)/F68 (4 mM) (n = 2; k_g = (2.8 ± 0.9) x 10^{-2} min^{-1}; t_{OR} = 7.0 ± 5.2 min) and 4.5 mM F68 (n = 1.3 ± 0.2; k_g = 0.17 ± 0.02 min^{-1}; t_{OR} = 8.1 ± 2.5 min)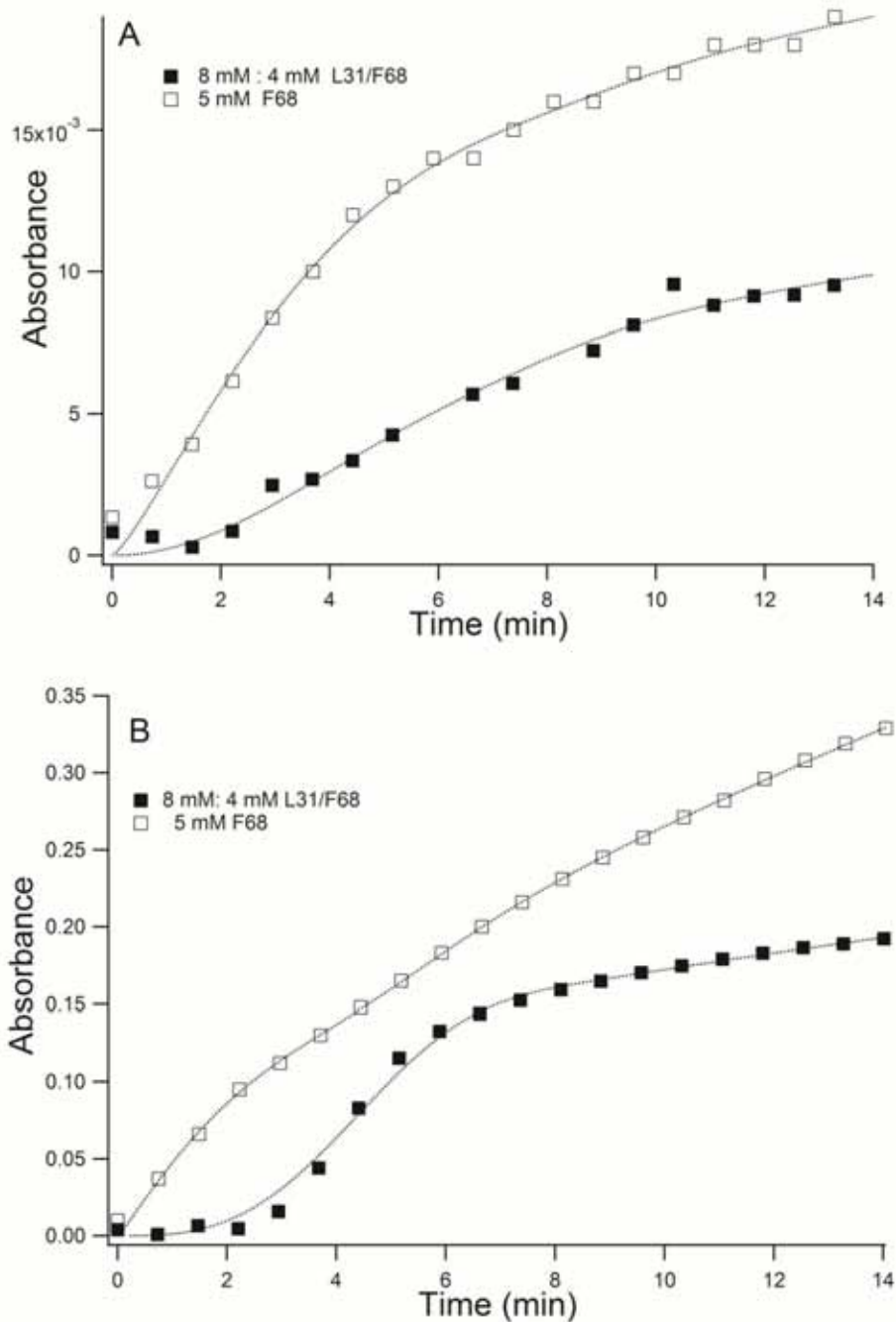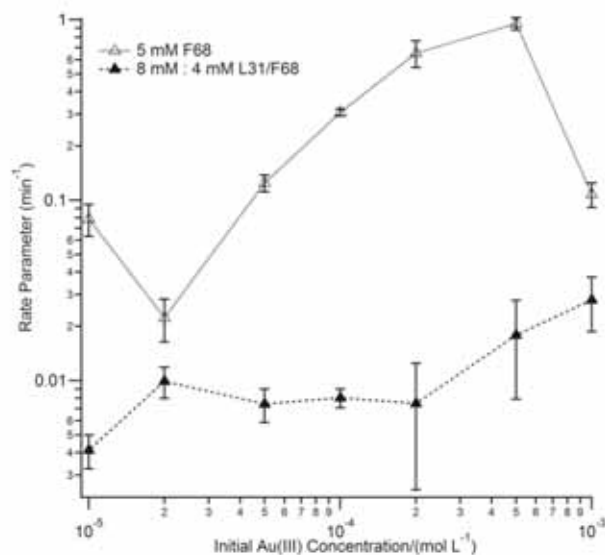. (B) Plot of 10^{-4} M initial Au(III) concentration of the 540 nm absorbance and L31 (8 mM)/F68 (4 mM) (n = 3; k_g = (7.7 ± 0.8) x 10^{-3} min^{-1}; t_{OR} = 8.0 ± 1.7 min) and 4.5 mM F68 (n = 1.0 ± 0.3; k_g = 0.30 ± 0.04 min^{-1}; t_{OR} = 4.4± 0.4).

Analysis of the peak fits between 10^{-3} M and 10^{-5} M indicate that onset of aggregative growth and the induction to the Ostwald growth regime occurs earlier for the F68 aqueous mixtures (Figures 3.15 and 3.16). The AuNP rate parameter, k_g, is higher for F68 alone than L31/F68 mixture. For example it is ~ 35-fold higher for F68 than for L31/F68 mixtures at initial 1 x 10^{-4} M Au(III) concentration (Figure 3.14A). For F68 solutions, this growth rate passes through a maximum presumably because the initial concentration of the Au primary nanocrystallites is low in the Au(III) concentration limits. The reduction of Au(III) is limited at low concentrations (1x10^{-5} M) by the availability of Au(III) and at high Au(III) (1x10^{-3} M) by the availability of redox sites on the TBP. The area under the nucleation function, $\Gamma(t)$, will be proportional to the particle number density.[36] According to our kinetic model, the ratio in the AuNP formation rates,

R_{high}(10^{-3}M)/R_{low}(10^{-5}M), with α ~1 and α'~ 2 is $\dfrac{\alpha K_m}{\alpha[Au(III)]_0} \approx \dfrac{1 \cdot 2 \cdot 10^{-4} M}{2 \cdot 1 \cdot 10^{-5} M} \approx 10$. This would

predict that $R_{high} > R_{low}$ if $\Gamma(t)$ is strongly associated with nucleation rates. However, we observe that $R_{high} < R_{low}$ (Figure 3.14B) in the active growth regime. Similar to the k_g parameters extracted from KJMA analysis,[14c, 15] $\Gamma(t)$ is associated strongly with growth rates and weakly to nucleation rates. The higher $\Gamma(t)$ value for F68 than L31/F68 mixtures indicates a greater particle number density in the former system. At high initial Au(III) concentration (10^{-3} M), the lower value of $\Gamma(t)$ indicates reduced AuNP number density, which may because of AuNP coalescence into larger anisotropic AuNPs. These larger AuNPs will have lower absorbance and scattering cross-sections at 540 nm. In contrast, at initial 10^{-4} M Au(III) concentration, $\Gamma(t)$ is higher having two peaks at ~ 7 and ~ 17 minutes.

A

B
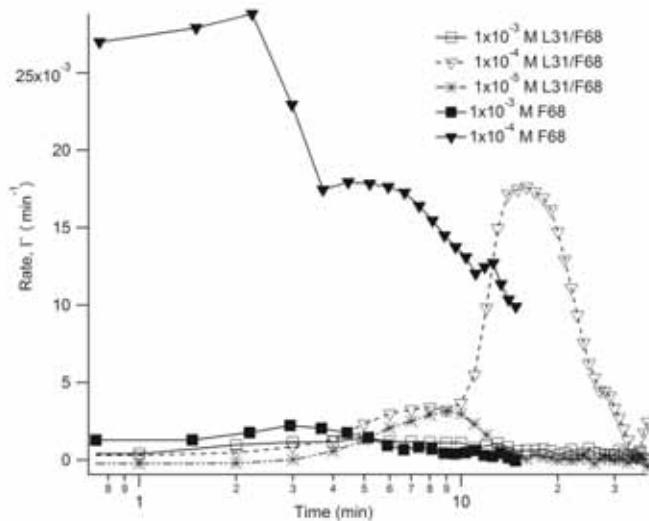
Figure 3.14 (A) Plot of the effective rate parameters, k_g, of L31 (8 mM)/F68 (4 mM) and F68 (4.5 mM) aqueous solutions against initial Au(III) concentration. (B) The aggregative nucleation rate, $\Gamma(min^{-1})$, against reaction time in the concentration range 10^{-3} to 10^{-4} M.
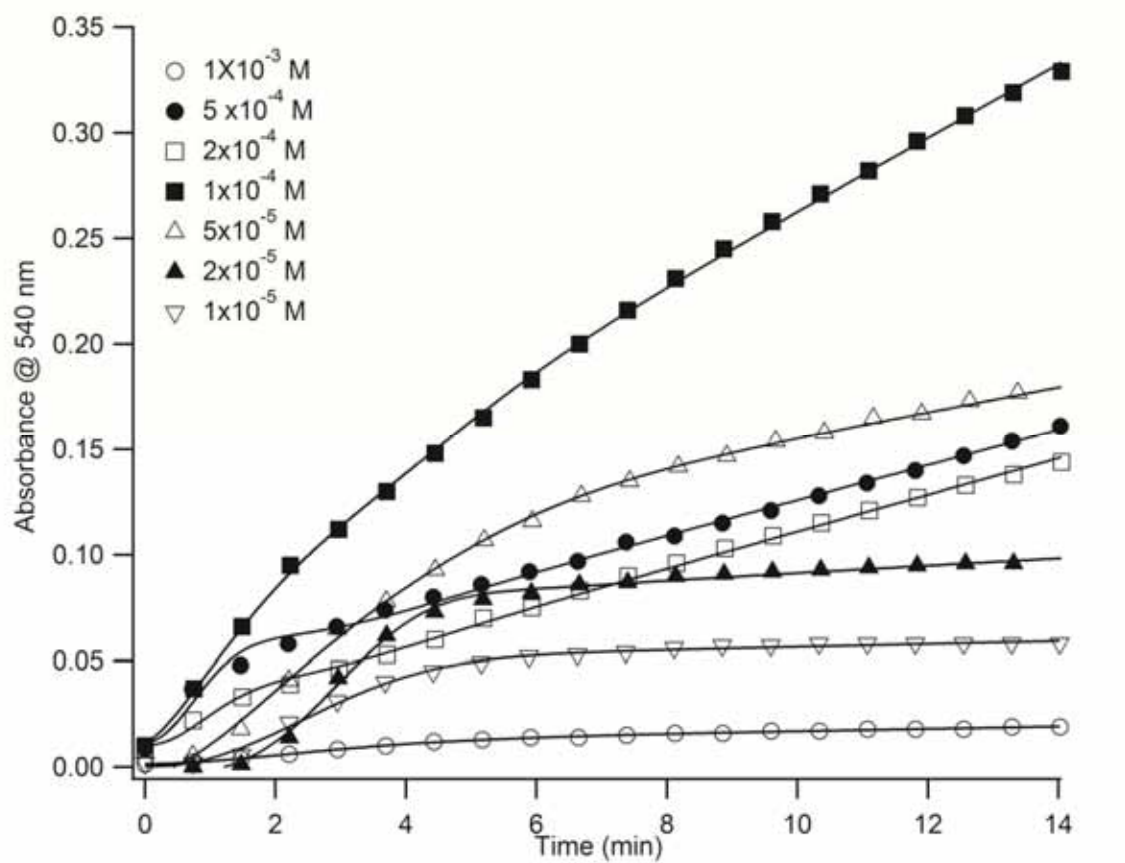
Figure 3.15 Plot of the UV-Vis 540 nm absorption against time for initial Au(III) concentrations between 10^{-3} M and 10^{-5} M. In all cases, Au(III) was added to 4.5 mM F68 aqueous solutions.
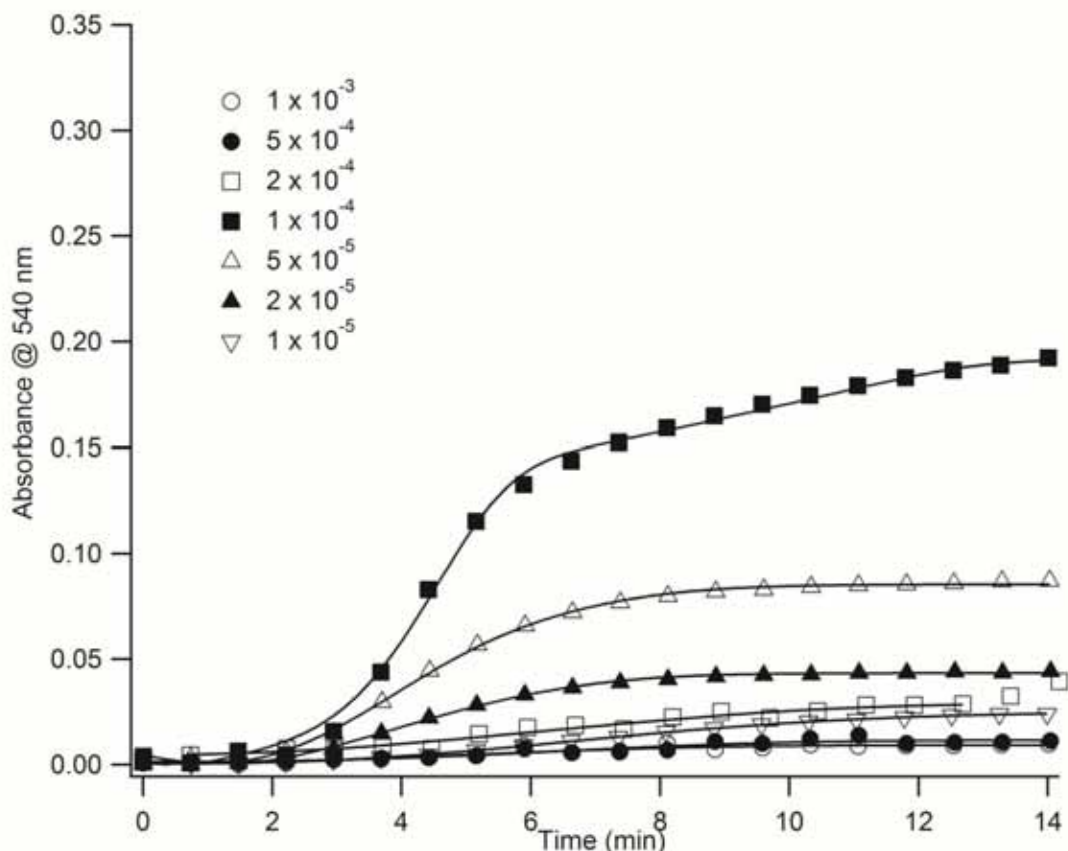
Figure 3.16 Plot of the UV-Vis 540 nm absorption against time for initial Au(III) concentrations between 10^{-3} M and 10^{-5} M. In all cases, Au(III) was added to L31/F68 (8 mM: 4 mM) aqueous solutions.

These multiple peaks will produce different size populations of AuNPs where the differences in the peak profiles between 10^{-3} and 10^{-4} M initial Au(III) concentrations is suggestive of aggregative nucleation processes that occur within ~ 30 minutes of reaction.

To confirm the presence of multiple populations of AuNPs, AFM images within the first 30 minutes of reaction were taken (Figure 3.17). These AuNPs were assumed to be spherical, with the z heights being used to construct the size distributions. Initial

washing with water was necessary to remove the excess copolymers. Suitable sampling

statistics were achieved by taking multiple AFM images on several different regions of

the mica surface. The height distributions show early time course bimodal size

distributions with diameters ~2 and ~5 nm within the first three minutes of Au(III)

addition. This was followed by formation of ~ 10 nm AuNPs after five minutes. After 30

minutes two distinct populations consisting of ~2 nm and larger ~ 20 nm AuNPs were

observed. A comparison of AFM height distributions with Γ (Figure 3.14B), shows

congruence with the ~7 and ~ 17 min peaks with the ~ 6 nm and ~ 20 nm mean

diameters. Thus, we have identified three AuNP populations: 1) the primary

nanocrystalline seeds of ~2 nm, 2) critical aggregates 5-10 nm, and 3) the larger AuNPs

(~ 20 nm). The DLS measurements (Figure 3.18) after 30 minutes show two distinct

hydrodynamic diameter populations due to AuNPs and a second larger population, which

are aggregates of these smaller AuNPs. Thus the existence of a bimodal distribution in

the early stages of nanoparticle growth is important experimental evidence to support an

aggregative growth model.
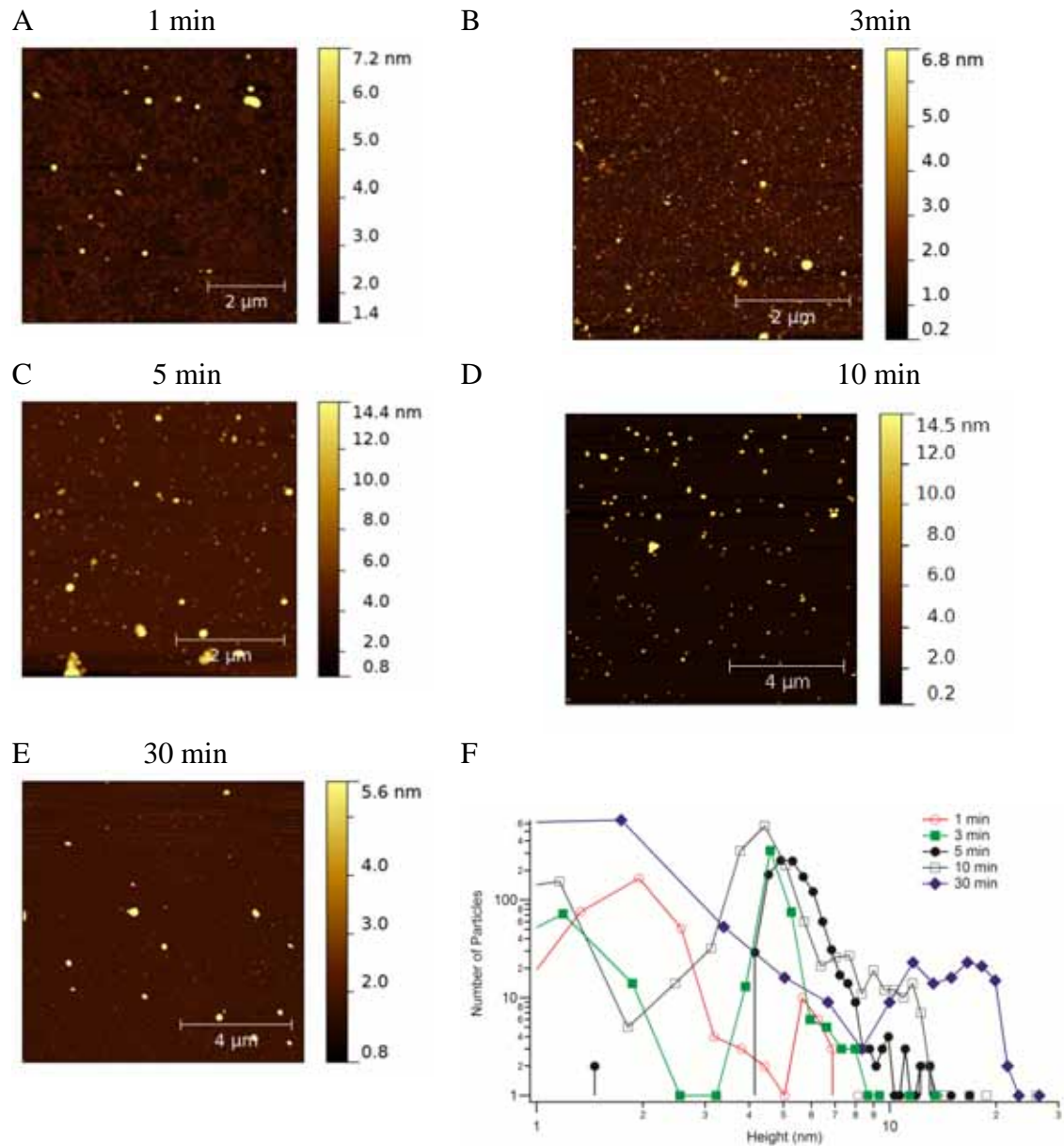
Figure 3.17 AFM images after 10^{-4} M Au(III) addition. (A) - (E) representative AFM images of AuNPs produced within the 1, 3, 5, 10 and 30 minutes of Au(III) addition, respectively. (F) Particle height distributions from processed AFM images at reaction times 1 min (N = 327), 3 min (N = 530), 5 min (N = 1166), 10 min (N = 1646) and 30 min (N = 1363).
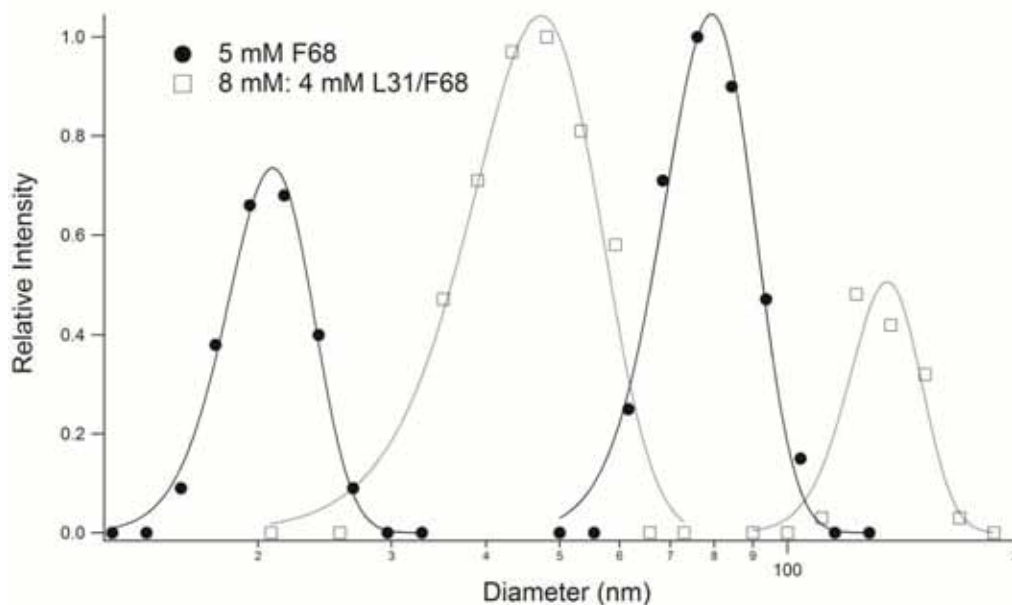
Figure 3.18 DLS volume-weighted AuNP size distributions in 5 mM F68 (black squares) and 8 mM l31: 4 mM F68 (open squares) solutions 30 minutes after adding 1 x 10^{-4} M Au(III).

The detailed Morphologies of the nanoparticles grown were further examined. Figure 3.19 shows a representative TEM image for a sample from the growth process after 60 minutes. The particles are irregular in shape and had twinned structures as evidenced by the small triangular prisms. The observation of the multiple crystal grain boundaries is characteristic of the polycrystalline nature for the nanoparticles as a result of interparticle coalescence. We note that previous TEM studies of TBP facilitated AuNP synthesis also show evidence of polycrystallinity.[20c, d] This serves as an important piece of evidence in support of the aggregative growth mechanism.

A
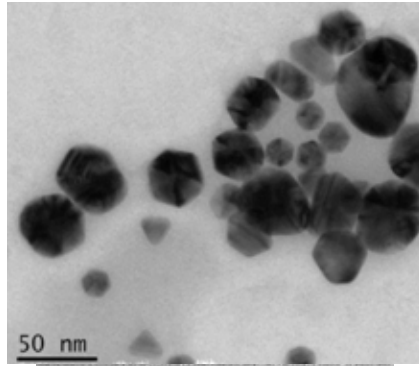
B
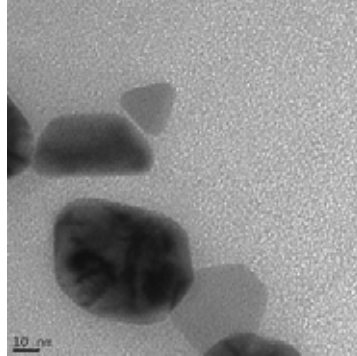
Figure 3.19 TEM images sampled after 60 minutes reaction. The images show (A,B) the polycrystalline nature of these nanoparticles.

Synthesis of Seeded TBP Coated Gold Nanoparticles

The seeded addition to precursor gold salts has been used to produce monodisperse Au NPs with a standard deviation of the size distribution of less than 10%. The concept of seeded addition involves having monomer Au NPs present in the solution before the reduction of precursor gold salts. Upon reduction of the precursor salts, there are two competing growth processes: 1) the faster growth of the smaller Au NPs and; 2) the dissolution of the smaller Au NPs and the molecular addition to monomers to the larger Au NPs (Ostwald growth). In the former case, the rate of the Au NP growth is inversely related to the diameter. Consequently, the smaller particles will grow faster decreasing the standard deviation in the nanoparticle sizes. This is termed *size focusing*.

In contrast, when the concentration of the monomers are low and/or the precursor ions are depleted, the second growth process becomes competitive, where the smaller Au NPs < 5 nm dissolve at the expense of the larger ones. This will increase the standard deviation in the nanoparticle sizes. This is termed *size defocusing*. We show in the following section that sufficient size focusing can be achieved by optimizing the parameters of citrated Au NP seed size and concentration.

We used a previously described method to synthesize citrated Au NPs of various sizes.[25] Figure 3.20 shows the plot of the UV-vis absorbance ratio against Au NP size determined by AFM. The particle sizes ranged from 6- 25 nm. Initially, the monomer concentration is high and size focusing dominates. In contrast, the subsequent additions of larger seeded nanoparticles will be in lower concentrations, such that nucleation and growth will mostly occur in the bulk solution.
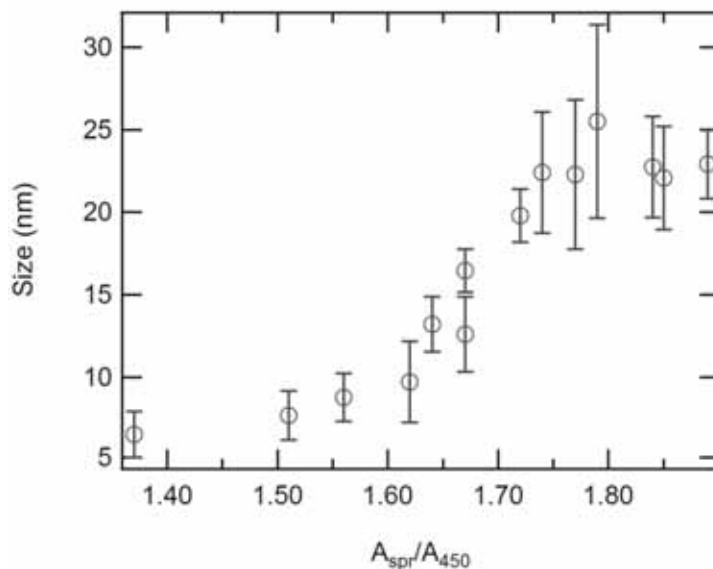
Figure 3.20 A plot of the ratio of the citrated AuNP size as measured by AFM against the ratio of the surface plasmon resonance absorbance maximum to the 450 nm peak as a function of seeded addition of citrated AuNPs.
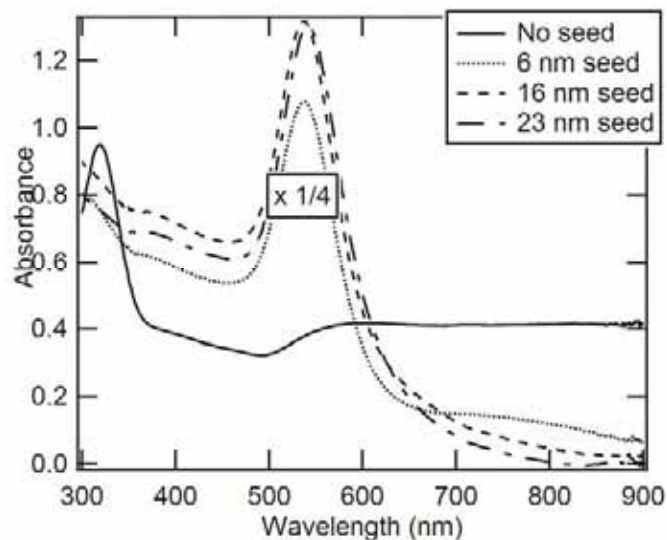
Figure 3.21 Representative UV-Vis spectra illustrating the effect of seeding with different sizes of citrated (50 µL added in each case) AuNPs to 1 mM Au(III) aqueous solution.

Figure 3.21 shows the effect of seeding with citrated AuNPs for 1 mM Au(III). The presence of monomer significantly changes size distribution of the nanoparticles. This is illustrated in the UV-vis spectra where the broad absorbance profile characteristic of larger anisotropic AuNPs is transformed in to a single SPR profile ~ 540 nm diagnostic of polyhedral AuNPs. The size distributions were further characterized by DLS (Figure 3.22) and SEM (Figure 3.23) that show that the 6 nm and 23 nm seed solutions were dominated by a single population of AuNPs. The TBP coated particles seeded with the smallest citrated AuNPs had the smallest size.
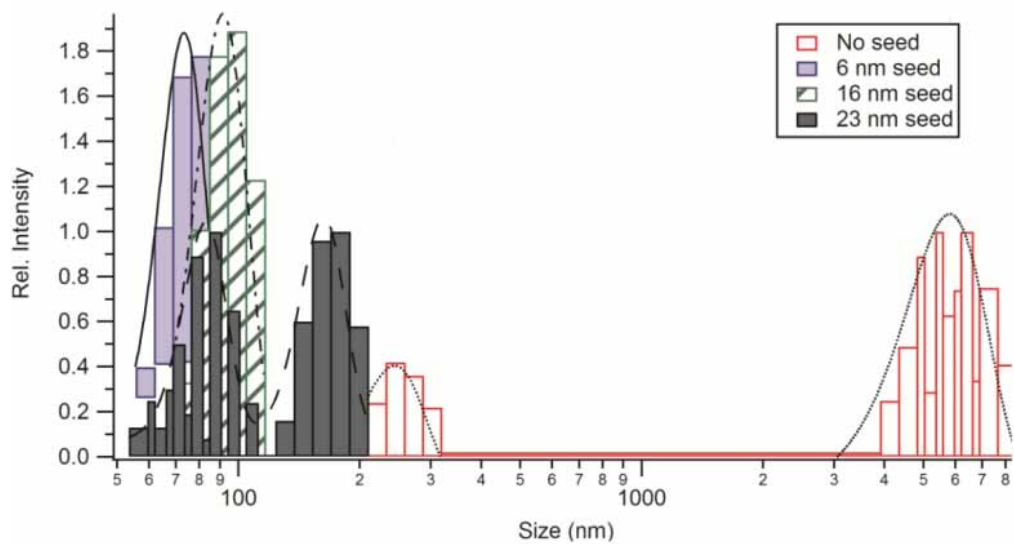
Figure 3.22 DLS of samples of AuNPs grown in the presence of TBP, incubated for 24 hrs at 25°C, seeded with 50 μL of citrate AuNPs, in 8 mM:4 mM of L31:F68 aqueous solutions.
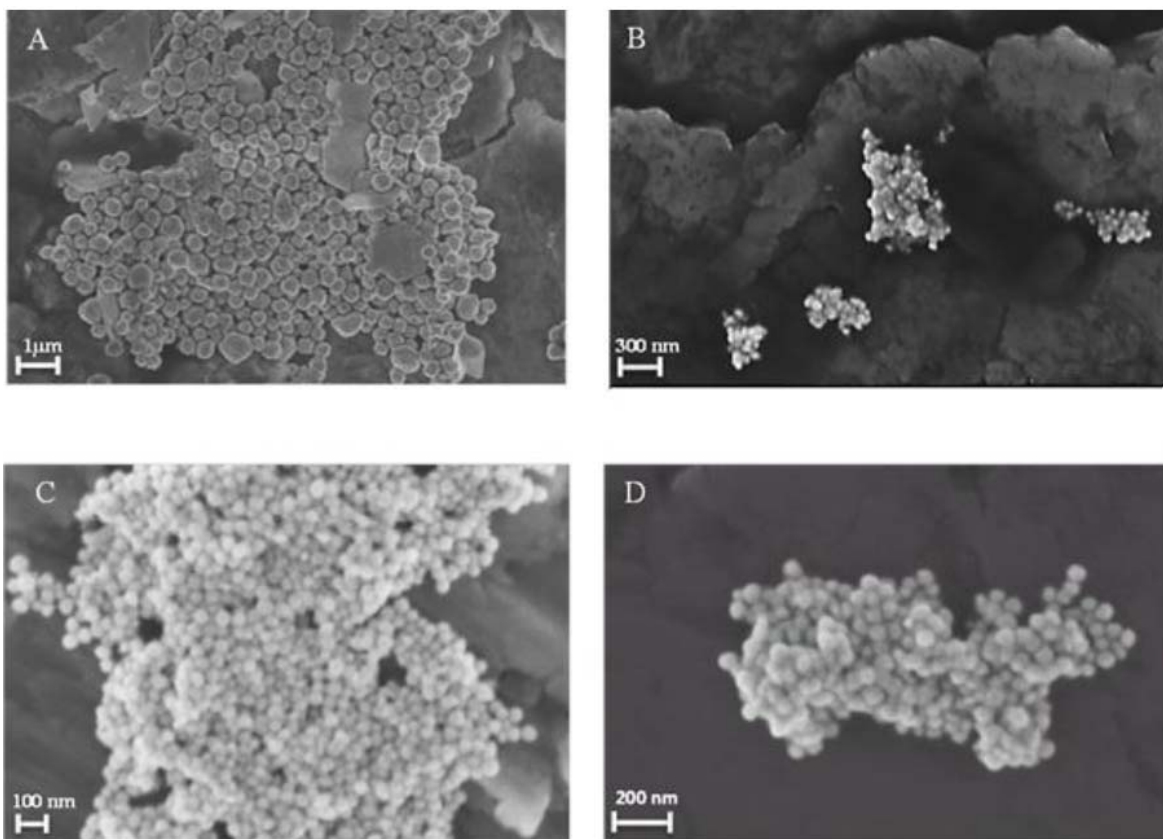
Figure 3.23 SEM images of TBP coated AuNPs incubated in 8 mM:4 mM; L31/F68 for 24 hrs at 25°C with A) no citrate seed, B) 50 μL of 6nm citrate seed , C) 50 μL of 16 nm citrate seed, D) 50 μL of 23 nm citrate seed.

Discussion

The nucleation and growth of anisotropic gold nanoparticles was accomplished using non-ionic TBPs. Kinetic control was achieved by varying the Pluronic/Au(III) ratio. The yields and sizes of anisotropic nanoparticles are higher in L31/F68 solutions than in F68 alone (Figures 3.2 and 3.5). The presence of the L31 inhibited the rate of primary nanocrystal formation and subsequent growth. Our simple kinetic model includes noncompetitive inhibition where L31 induces changes in the F68 conformation that prevents F68 EO_x units from binding to gold ions. The role of the L31 in the growth

phase producing higher energy nanostructures having larger surface areas may be caused by the inhibition of growth on certain crystallographic faces.

In general, larger gold particles are produced by Pluronics having shorter PEO blocks because the rate of metal ion reduction appears to be limited by reduction on the gold surface instead of in the bulk solution.[21] Furthermore, published results of TBP facilitated Au(III) reduction suggest that the interdependence of block copolymer adsorption on different facets of the growing crystal and crystal growth kinetics (rate of metal ion reduction) could determine nanoparticle shape.[22b, 37]

Dissipative particle dynamics (DPD) simulations of gold nanoparticles in PEO-PPO-PEO micelles indicates that gold atoms are wrapped by the copolymer and form spherical particles inside the micelles.[38] The hydrophobic PO segments are adsorbed on the surface of AuNPs whereas the hydrophilic EO segments are exposed to water forming stable Pluronic-gold colloids with two-layer structures. This simulated dynamic process suggests that the morphology and size of gold nanoparticles depend on the competition between the aggregation of gold clusters and stabilization by block copolymer micelles.

High yields of microplates were achieved by Sakai and Alexandridis using a TBP with PO: EO ratio of 0.9 in Pluronic L64 (EO_{13}-PO_{30}-EO_{13}).[22b] They argued that more anisotropic particles were produced at this PO:EO ratio because reduction on the PEO ether backbone becomes the rate limiting step. They further attributed the origin of the plate morphology to $AuCl_4^-$ reduction on the facets instead of the shape-directing action of the polymeric lyotropic liquid crystals as "soft" templates.

We used two models to describe AuNP growth kinetics. The first model describes the formation of the primary nanocrystals while the second KJMA model describes the

subsequent aggregative growth and Ostwald ripening processes. The rate of primary

nanocrystal formation is described by eqn. 2. In the modified KJMA model, the rate of

aggregative nucleation, $\Gamma(t)$ is proportional to the AuNP number density. The paradox of

high AuNP formation rate and slower growth rate in the high concentration limit is

rationalized by the coalescence of the nanocrystals reducing the number density and

hence the aggregative nucleation rate $\Gamma(t)$.

In the active growth regime the 540 nm UV-vis absorbance can be fit to a KJMA

model describing aggregative growth (Figure 3.13). Furthermore, AFM height

distribution data indicate multiple AuNP populations (Figure 3.17). Another experimental

piece of evidence for this mechanism is the observation of polycrystalline AuNPs (Figure

3.19). Based upon these observations, we propose a refinement of the AuNP growth

model in the presence of TBPs.[41, 47-48] The growth kinetics will be dominated by

aggregative processes since the initial nucleation events to form seeds occur rapidly. The

components of a refined model include: 1) reduction of metal ions by the TBPs to

produce seeds of different morphologies (primary nanocrystals $\approx$ 1-2 nm) depending on

TBP PO:EO ratios and the local microenvironment around the nanocrystals 2) initial

self-assembly of these seeds to critical aggregates in a non-classical nucleation step and

3) aggregative growth accomplished by the addition of primary crystals as described in 1)

to the critical aggregates. Finally, additional Ostwald ripening can occur by the TBP

facilitated Au(III) reduction on the nanoparticle surface.

Our model of aggregated growth is summarized in Schemes 3.2 and 3.3 where the

growth kinetics of step 1 and 2 can be controlled by the $EO_x/Au(III)$ ratio. The growth

can be described by relating nanocrystallite growth and aggregative growth to the rate

112

parameters k_4' and k_g. The rate of the AuNP seed formation is proportional to both EO_x and Au(III) concentrations. In the UV-vis induction period (< 3 minutes), AuNP seeds are the dominant species. At the onset of aggregative growth, the growth rate is assumed to be proportional to the AuNP seed concentration (number density). The slower growth behavior in the limit of high Au(III) concentration is accounted in our model by AuNP seeds forming critical aggregates that grow anistropically via the "soft-templating" of the TBP at the edges of AuNP surfaces. The presence of L31 in the aqueous mixture will reduce the concentration of primary nanocrystals and the decrease in AuNP growth rate because of the preferential adsorption of L31 on certain crystallographic faces blocks growth in these directions. This "soft templating" by the L31 and the preferential reduction of Au(III) on the lower coordination edge atoms may account for the larger AuNP sizes.

Our kinetic model can be extended as an empirical tool to quantify the effect of reaction conditions on AuNP size and shape. At the limit of low initial Au(III) concentration, the rate of nanocrystal seed formation is proportional to Au(III) concentration. In this regime, we predict that the particle sizes will be proportional to Au(III) concentration. When $K_m \sim$ Au(III) concentration, the AuNPs produced are polydisperse with multiple size populations (Figure 3.14). At the limit of high Au(III) concentration, R_{NP} is constant giving an upper limit of AuNP number density and hence an upper limit of AuNP size.

The utility of our approach is that the kinetics of gold growth can be modified through optimizing the phase behavior of quaternary mixtures of hydrophobic (mostly PPO) and hydrophilic (mostly PEO) block copolymers with water and Au(III). Our

results suggest that the yield of nanoplates may be further optimized via changes in ion/seed concentration, temperature and block copolymer binary mixture composition. The development of alternative synthetic routes leading to both high monodispersity and versatile surface chemistry is still a challenge above 40 nm. This is particularly the case for triblock copolymers where establishing control over AuNP size and shape requires a detailed understanding of the mechanism and kinetics of precursor reduction and particle growth. Our preliminary results shows that the seeding methodology provides promise in controlled the TBP AuNP heterogeneity.
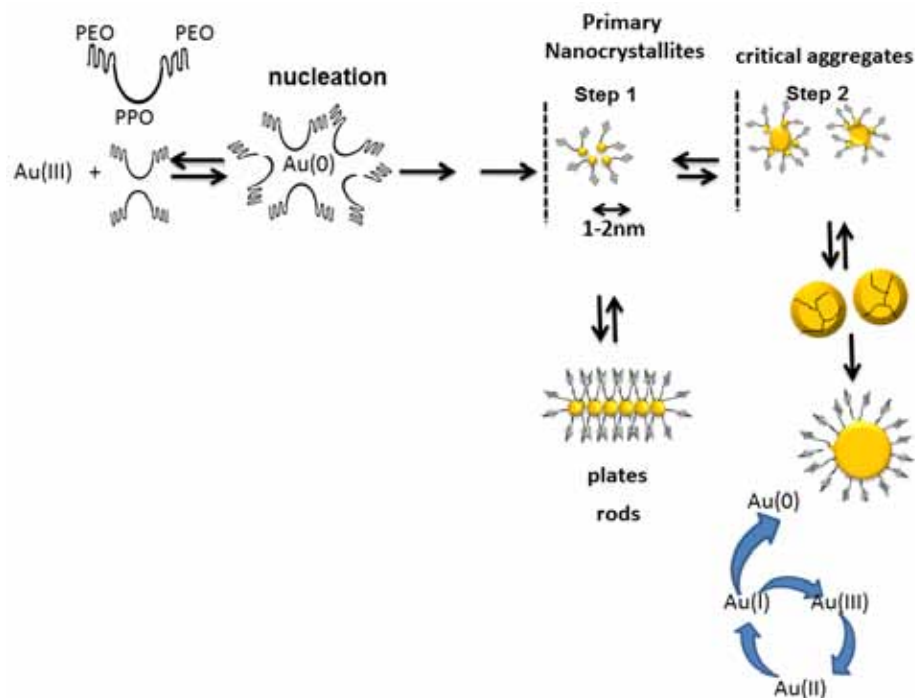
Scheme 3.2 The proposed model of Au nanoparticle growth facilitated by TBPs.

References

1.   (a) Link, S.; El-Sayed, M. A., Size and temperature dependence of the plasmon absorption of colloidal gold nanoparticles. *J. Phys. Chem. B* **1999,** *103* (21), 4212-4217; (b) Murray, C. B.; Kagan, C. R.; Bawendi, M. G., Synthesis and Characterization of Monodisperse Nnaocrystals and Close-Packed Nanocrystal Assemblies. *Annual Review of Materials Science* **2000,** *30* (1), 545-610; (c) Kelly, K. L.; Coronado, E.; Zhao, L. L.; Schatz, G. C., The Optical Properties of Metal Nanoparticles: The Influence of Size, Shape, and Dielectric Environment. *J. Phys. Chem. B* **2003,** *107* (3), 668-677; (d) Grassian, V. H., When Size Really Matters: Size-Dependent Properties and Surface Chemistry of Metal and Metal Oxide Nanoparticles in Gas and Liquid Phase Environments. *J. Phys. Chem. C* **2008,** *112* (47), 18303-18313; (e) Burda, C.; Chen, X.; Narayanan, R.; El-Sayed, M. A., Chemistry and Properties of Nanocrystals of Different Shapes. *Chem. Rev.* **2005,** *105*, 1025-1102; (f) Emory, S. R.; Haskins, W. E.; Nie, S., Direct Observation of Size-Dependent Optical Enhancement in Single Metal Nanoparticles. *J. Am. Chem. Soc.* **1998,** *120* (31), 8009-8010.

2.   (a) Jain, P. K.; Lee, K. S.; El-Sayed, I. H.; El-Sayed, M. A., Calculated Absorption and Scattering Properties of Gold Nanoparticles of Different Size, Shape, and Composition: Applications in Biological Imaging and Biomedicine. *J. Phys. Chem. B* **2006,** *110* (14), 7238-7248; (b) Lee, K. S.; El-Sayed, M. A., Gold and Silver Nanoparticles in Sensing and Imaging: Sensitivity of Plasmon Response to Size, Shape, and Metal Composition. *J. Phys. Chem. B* **2006,** *110* (39), 19220-19225; (c) Millstone, J. E.; Hurst, S. J.; Métraux, G. S.; Cutler, J. I.; Mirkin, C. A., Colloidal Gold and Silver Triangular Nanoprisms. *Small* **2009,** *5* (6), 646-664; (d) Stiles, P. L.; Dieringer, J. A.; Shah, N. C.; Van Duyne, R. P., Surface-Enhanced Raman Spectroscopy. *Annu. Rev. Anal. Chem.* **2008,** *1* (1), 601-626.

3.   Willets, K. A.; Van Duyne, R. P., Localized Surface Plasmon Resonance Spectroscopy and Sensing. *Annu. Rev. Phys. Chem.* **2007,** *58* (1), 267-297.

4.   Schmucker, A. L.; Harris, N.; Banholzer, M. J.; Blaber, M. G.; Osberg, K. D.; Schatz, G. C.; Mirkin, C. A., Correlating Nanorod Structure with Experimentally Measured and Theoretically Predicted Surface Plasmon Resonance. *ACS Nano* **2010,** *4* (9), 5453-5463.

5.   Daniel, M.-C.; Astruc, D., Gold Nanoparticles: Assembly, Supramolecular Chemistry, Quantum-Size-Related Properties, and Applications toward Biology, Catalysis, and Nanotechnology. *Chem. Rev.* **2004,** *104*, 293-346.

6.   Xia, Y.; Xiong, Y.; Lim, B.; Skrabalak, S. E., Shape-Controlled Synthesis of Metal Nanocrystals: Simple Chemistry Meets Complex Physics? *Angewandte Chemie International Edition* **2009,** *48* (1), 60-103.

7. (a) Millstone, J.; Métraux, G.; Mirkin, C., Controlling the Edge Length of Gold Nanoprisms via a Seed-Mediated Approach. *Adv. Funct. Mater.* **2006,** *16* (9), 1209-1214; (b) Millstone, J. E.; Park, S.; Shuford, K. L.; Qin, L.; Schatz, G. C.; Mirkin, C. A., Observation of a Quadrupole Plasmon Mode for a Colloidal Solution of Gold Nanoprisms. *J. Am. Chem. Soc.* **2005,** *127* (15), 5312-5313.

8. Malikova, N.; Pastoriza-Santos, I.; Schierhorn, M.; Kotov, N. A.; Liz-Marzán, L. M., Layer-by-Layer Assembled Mixed Spherical and Planar Gold Nanoparticles: Control of Interparticle Interactions. *Langmuir* **2002,** *18* (9), 3694-3697.

9. Tan, Y. N.; Lee, J. Y.; Wang, D. I. C., Aspartic Acid Synthesis of Crystalline Gold Nanoplates, Nanoribbons, and Nanowires in Aqueous Solutions. *J. Phys. Chem. C* **2008,** *112* (14), 5463-5470.

10. Kim, J.-U.; Cha, S.-H.; Shin, K.; Jho, J. Y.; Lee, J.-C., Preparation of Gold Nanowires and Nanosheets in Bulk Block Copolymer Phases under Mild Conditions. *Adv. Mater.* **2004,** *16* (5), 459-464.

11. Biswal, J.; Ramnani, S. P.; Shirolikar, S.; Sabharwal, S., Synthesis of rectangular plate like gold nanoparticles by in situ generation of seeds by combining both radiation and chemical methods. *Radiat. Phys. Chem.* **2011,** *80* (1), 44-49.

12. (a) LaMer, V. K.; Dinegar, R. H., Theory, Production and Mechanism of Formation of Monodispersed Hydrosols. *J. Am. Chem. Soc.* **1950,** *72* (11), 4847-4854; (b) Mer, V. K. L., Nucleation in Phase Transitions. *Industrial & Engineering Chemistry* **1952,** *44* (6), 1270-1277.

13. (a) Saunders, A. E.; Sigman, M. B.; Korgel, B. A., Growth Kinetics and Metastability of Monodisperse Tetraoctylammonium Bromide Capped Gold Nanocrystals. *J. Phys. Chem. B* **2003,** *108* (1), 193-199; (b) Drofenik, M.; Kristl, M.; Žnidaršič, A.; Hanžel, D.; Lisjak, D., Hydrothermal Synthesis of Ba-Hexaferrite Nanoparticles. *J. Am. Ceram. Soc.* **2007,** *90* (7), 2057-2061; (c) Robb, D. T.; Privman, V., Model of Nanocrystal Formation in Solution by Burst Nucleation and Diffusional Growth. *Langmuir* **2007,** *24* (1), 26-35; (d) Zheng, H.; Smith, R. K.; Jun, Y.-w.; Kisielowski, C.; Dahmen, U.; Alivisatos, A. P., Observation of Single Colloidal Platinum Nanocrystal Growth Trajectories. *Science* **2009,** *324* (5932), 1309-1312.

14. (a) Ji, X.; Song, X.; Li, J.; Bai, Y.; Yang, W.; Peng, X., Size Control of Gold Nanocrystals in Citrate Reduction: The Third Role of Citrate. *J. Am. Chem. Soc.* **2007,** *129* (45), 13939-13948; (b) Polte, J. r.; Ahner, T. T.; Delissen, F.; Sokolov, S.; Emmerling, F.; Thunemann, A. F.; Kraehnert, R., Mechanism of Gold Nanoparticle Formation in the Classical Citrate Synthesis Method Derived from Coupled In Situ XANES and SAXS Evaluation. *J. Am. Chem. Soc.* **2010,** *132* (4), 1296-1301; (c) Njoki, P. N.; Luo, J.; Kamundi, M. M.; Lim, S.; Zhong, C.-J., Aggregative Growth in the Size-Controlled Growth of Monodispersed Gold Nanoparticles. *Langmuir* **2010,** *26* (16), 13622-13629.

15.   Shields, S. P.; Richards, V. N.; Buhro, W. E., Nucleation Control of Size and Dispersity in Aggregative Nanoparticle Growth. A Study of the Coarsening Kinetics of Thiolate-Capped Gold Nanocrystals. *Chem. Mater.* **2010,** *22* (10), 3212-3225.

16.   (a) Bisson, L.; Boissiere, C.; Nicole, L.; Grosso, D.; Jolivet, J. P.; Thomazeau, C. c.; Uzio, D.; Berhault, G.; Sanchez, C. m., Formation of Palladium Nanostructures in a Seed-Mediated Synthesis through an Oriented-Attachment-Directed Aggregation. *Chem. Mater.* **2009,** *21* (13), 2668-2678; (b) Huang, F.; Zhang, H.; Banfield, J. F., Two-Stage Crystal-Growth Kinetics Observed during Hydrothermal Coarsening of Nanocrystalline ZnS. *Nano Lett.* **2003,** *3* (3), 373-378; (c) Turkevich, J., Colloidal gold. Part I. *Gold Bull.* **1985,** *18* (3), 86-91.

17.   Drews, T. O.; Katsoulakis, M. A.; Tsapatsis, M., A Mathematical Model for Crystal Growth by Aggregation of Precursor Metastable Nanoparticles. *J. Phys. Chem. B* **2005,** *109* (50), 23879-23887.

18.   (a) Richards, V. N.; Rath, N. P.; Buhro, W. E., Pathway from a Molecular Precursor to Silver Nanoparticles: The Prominent Role of Aggregative Growth. *Chem. Mater.* **2010,** *22* (11), 3556-3567; (b) Hornstein, B. J.; Finke, R. G., Transition-Metal Nanocluster Kinetic and Mechanistic Studies Emphasizing Nanocluster Agglomeration: Demonstration of a Kinetic Method That Allows Monitoring of All Three Phases of Nanocluster Formation and Aging. *Chem. Mater.* **2003,** *16* (1), 139-150; (c) Besson, C.; Finney, E. E.; Finke, R. G., A Mechanism for Transition-Metal Nanoparticle Self-Assembly. *J. Am. Chem. Soc.* **2005,** *127* (22), 8179-8184; (d) Besson, C.; Finney, E. E.; Finke, R. G., Nanocluster Nucleation, Growth, and Then Agglomeration Kinetic and Mechanistic Studies: A More General, Four-Step Mechanism Involving Double Autocatalysis. *Chem. Mater.* **2005,** *17* (20), 4925-4938.

19.   (a) Takahashi, H.; Niidome, Y.; Niidome, T.; Kaneko, K.; Kawasaki, H.; Yamada, S., Modification of Gold Nanorods Using Phosphatidylcholine to Reduce Cytotoxicity. *Langmuir* **2005,** *22* (1), 2-5; (b) Murphy, C. J.; Gole, A. M.; Stone, J. W.; Sisco, P. N.; Alkilany, A. M.; Goldsmith, E. C.; Baxter, S. C., Gold Nanoparticles in Biology: Beyond Toxicity to Cellular Imaging. *Accounts of Chemical Research* **2008,** *41* (12), 1721-1730; (c) Alexandridis, P., Gold Nanoparticle Synthesis, Morphology Control, and Stabilization Facilitated by Functional Polymers. *Chem. Eng. Technol.* **2011,** *34* (1), 15-28.

20.   (a) Sakai, T.; Alexandridis, P., Single-step synthesis and stabilization of metal nanoparticles in aqueous Pluronic block copolymer solutions at ambient temperature. **2004,** *20* (20), 8426; (b) Goy-López, S.; Castro, E.; Taboada, P.; Mosquera, V. c., Block Copolymer-Mediated Synthesis of Size-Tunable Gold Nanospheres and Nanoplates. *Langmuir* **2008,** *24* (22), 13186-13196; (c) Khullar, P.; Mahal, A.; Singh, V.; Banipal, T. S.; Kaur, G.; Bakshi, M. S., How PEO-PPO-PEO Triblock Polymer Micelles Control the Synthesis of Gold Nanoparticles: Temperature and Hydrophobic Effects. *Langmuir* **2010,** *26* (13), 11363-11371;

(d) Khullar, P.; Singh, V.; Mahal, A.; Kaur, H.; Singh, V.; Banipal, T. S.; Kaur, G.; Bakshi, M. S., Tuning the Shape and Size of Gold Nanoparticles with Triblock Polymer Micelle Structure Transitions and Environments. *J. Phys. Chem. C* **2011**, *115* (21), 10442-10454.

21.   (a) Sakai, T.; Alexandridis, P., Single-Step Synthesis and Stabilization of Metal Nanoparticles in Aqueous Pluronic Block Copolymer Solutions at Ambient Temperature. *Langmuir* **2004,** *20* (20), 8426-8430; (b) Sakai, T.; Alexandridis, P., Mechanism of metal ion reduction, nanoparticle growth and size control in aqueous amphiphilic block copolymer solutions at ambient conditions. *J. Phys. Chem. B* **2005,** *109* (16), 7766–7777; (c) Sakai, T.; Alexandridis, P., Size- and shape-controlled synthesis of colloidal gold through autoreduction of the auric cation by poly(ethylene oxide)–poly(propylene oxide) block copolymers in aqueous solutions at ambient conditions. *Nanotechnology* **2005,** *16* (7), S344.

22.   (a) Sakai, T.; Alexandridis, P., Spontaneous Formation of Gold Nanoparticles in Poly(ethylene oxide)-Poly(propylene oxide) Solutions: Solvent Quality and Polymer Structure Effects. *Langmuir* **2005,** *21* (17), 8019-8025; (b) Sakai, T.; Alexandridis, P., High-Yield Synthesis of Gold Microplates Using Amphiphilic Block Copolymers: Are Lyotropic Liquid Crystals Required? *Macromol. Symp.* **2010,** *289* (1), 18-24.

23.   Wanka, G.; Hoffmann, H.; Ulbricht, W., Phase Diagrams and Aggregation Behavior of Poly(oxyethylene)-Poly(oxypropylene)-Poly(oxyethylene) Triblock Copolymers in Aqueous Solutions. *Macromolecules* **1994,** *27* (15), 4145-4159.

24.   Bahadur, P.; Li, P.; Almgren, M.; Brown, W., Effect of potassium fluoride on the micellar behavior of Pluronic F-68 in aqueous solution. *Langmuir* **1992,** *8* (8), 1903-1907.

25.   Bastús, N. G.; Comenge, J.; Puntes, V. c., Kinetically Controlled Seeded Growth Synthesis of Citrate-Stabilized Gold Nanoparticles of up to 200 nm: Size Focusing versus Ostwald Ripening. *Langmuir* **2011,** *27* (17), 11098-11105.

26.   (a) Caruso, R. A.; Ashokkumar, M.; Grieser, F., Sonochemical Formation of Gold Sols. *Langmuir* **2002,** *18* (21), 7831-7836; (b) Pacławski, K.; Fitzner, K., Kinetics of gold(III) chloride complex reduction using sulfur(IV). *Metallurgical and Materials Transactions B* **2004,** *35* (6), 1071-1085.

27.   Kou, L.; Labrie, D.; Chylek, P., Refractive indices of water and ice in the 0.l65-2.5 um spectral range. *Appl. Opt.* **1993,** *32*, 3531-3540.

28.   (a) Wang, L.; Chen, X.; Zhan, J.; Chai, Y.; Yang, C.; Xu, L.; Zhuang, W.; Jing, B., Synthesis of Gold Nano- and Microplates in Hexagonal Liquid Crystals. *J. Phys. Chem. B* **2005,** *109* (8), 3189-3194; (b) Mason, W. R.; Gray, H. B., Electronic structures of square-planar complexes. *J. Am. Chem. Soc.* **1968,** *90* (21), 5721-5729; (c) Torigoe, K.; Esumi, K., Preparation of colloidal gold by

photoreduction of tetracyanoaurate(1-)-cationic surfactant complexes. *Langmuir* **1992,** *8* (1), 59-63; (d) Vogler, A.; Kunkely, H., Photoreactivity of gold complexes. *Coord. Chem. Rev.* **2001,** *219-221*, 489-507; (e) Wang, S.; Qian, K.; Bi, X.; Huang, W., Influence of Speciation of Aqueous HAuCl4 on the Synthesis, Structure, and Property of Au Colloids. *J. Phys. Chem. C* **2009,** *113* (16), 6505-6510.

29.   Ojea-Jiménez, I.; Romero, F. M.; Bastús, N. G.; Puntes, V., Small Gold Nanoparticles Synthesized with Sodium Citrate and Heavy Water: Insights into the Reaction Mechanism. *J. Phys. Chem. C* **2010,** *114* (4), 1800-1804.

30.   (a) Shuford, K. L.; Ratner, M. A.; Schatz, G. C., Multipolar excitation in triangular nanoprisms. *J. Chem. Phys.* **2005,** *123* (11), 114713; (b) Hong, S.; Shuford, K. L.; Park, S., Shape Transformation of Gold Nanoplates and their Surface Plasmon Characterization: Triangular to Hexagonal Nanoplates. *Chem. Mater.* **2011,** *23* (8), 2011-2013.

31.   SUN, J.; GUAN, M.; SHANG, T.; GAO, C.; XU, Z., Synthesis and optical properties of triangular gold nanoplates with controllable edge length. *SCIENCE CHINA Chemistry* **2010,** *53* (9), 2033-2038.

32.   (a) Burchard, W., Static and dynamic light scattering from branched polymers and biopolymers. In *Light Scattering from Polymers*, Springer Berlin / Heidelberg: 1983; Vol. 48, pp 1-124; (b) Urban, C.; Schurtenberger, P., Characterization of Turbid Colloidal Suspensions Using Light Scattering Techniques Combined with Cross-Correlation Methods. *J. Colloid Interface Sci.* **1998,** *207* (1), 150-158.

33.   Isci, H.; Mason, W. R., Ligand-to-metal charge-transfer spectra of tetrahaloaurate(III) and trans-dicyanodihaloaurate(III) ions. *Inorg. Chem.* **1983,** *22* (16), 2266-2272.

34.   Longenberger, L.; Mills, G., Formation of Metal Particles in Aqueous Solutions by Reactions of Metal Complexes with Polymers. *The Journal of Physical Chemistry* **1995,** *99* (2), 475-478.

35.   Sabir, T. S.; Yan, D.; Milligan, J. R.; Aruni, A. W.; Nick, K. E.; Ramon, R. H.; Hughes, J. A.; Chen, Q.; Kurti, R. S.; Perry, C. C., Kinetics of Gold Nanoparticle Formation Facilitated by Triblock Copolymers. *J. Phys. Chem. C* **2012,** *116* (7), 4431-4441.

36.   Wette, P.; Schöpe, H. J.; Palberg, T., Microscopic investigations of homogeneous nucleation in charged sphere suspensions. *J. Chem. Phys.* **2005,** *123* (17), 174902.

37.   (a) Bakshi, M. S. K., Aman; Bhandari, Poonam; Kaur, Gurinder; Torigoe, Kanjiro; Esumi, Kunio, Synthesis of Colloidal Gold Nanoparticles of Different Morphologies in the Presence of Triblock Polymer Micelles. *J. Nanosci. Nanotechnol.* **2006,** *6*, 1405-1410; (b) Chen, S.; Guo, C.; Hu, G.-H.; Wang, J.;

Ma, J.-H.; Liang, X.-F.; Zheng, L.; Liu, H.-Z., Effect of Hydrophobicity inside PEO−PPO−PEO Block Copolymer Micelles on the Stabilization of Gold Nanoparticles: Experiments. *Langmuir* **2006,** *22* (23), 9704-9711; (c) Chen, S.; Guo, C.; Hu, G.-H.; Liu, H.-Z.; Liang, X.-F.; Wang, J.; Ma, J.-H.; Zheng, L., Dissipative particle dynamics simulation of gold nanoparticles stabilization by PEO–PPO–PEO block copolymer micelles *Colloid Polym. Sci.* **2007,** *285*, 1543-1552; (d) Rahme, K.; Gauffre, F.; Marty, J.-D.; Payré, B.; Mingotaud, C., A Systematic Study of the Stabilization in Water of Gold Nanoparticles by Poly(Ethylene Oxide)−Poly(Propylene Oxide)−Poly(Ethylene Oxide) Triblock Copolymers. *J. Phys. Chem. C* **2007,** *111* (20), 7273-7279.

38.   Chen, S.; Guo, C.; Hu, G.-H.; Liu, H.-Z.; Liang, X.-F.; Wang, J.; Ma, J.-H.; Zheng, L., Dissipative particle dynamics simulation of gold nanoparticles stabilization by PEO–PPO–PEO block copolymer micelles. *Colloid Polym. Sci.* **2007,** *285* (14), 1543-1552.
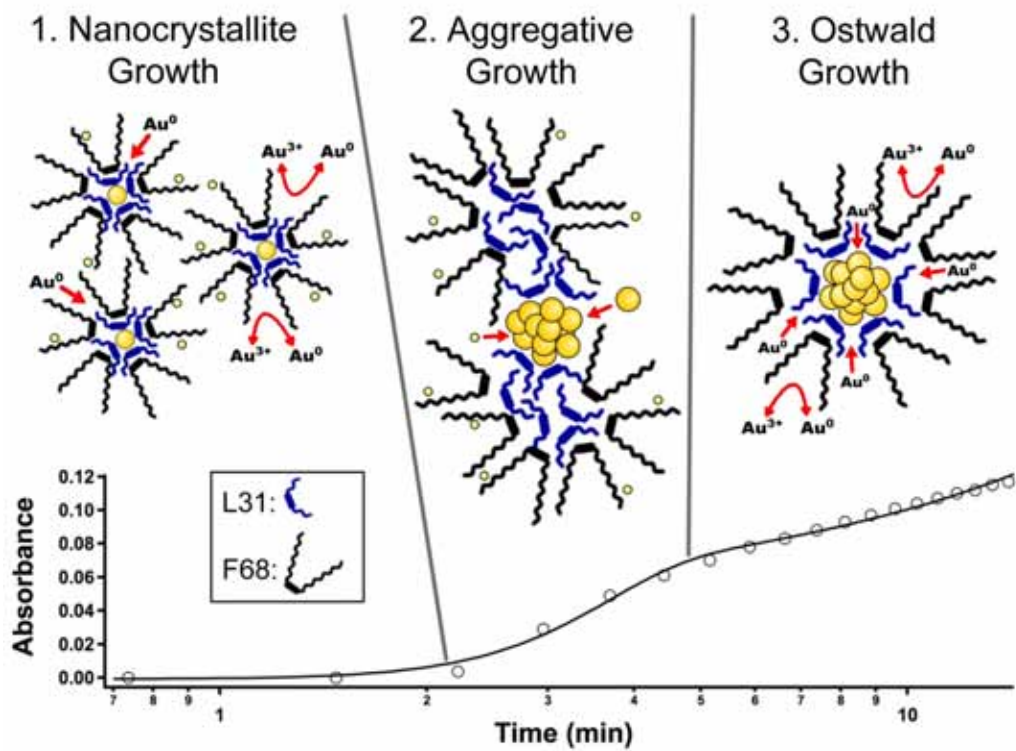
Scheme 3.3 Proposed TOC Graphic

CHAPTER FOUR

CONCLUSIONS

Block copolymers incorporating particular polymer blocks with specific

characteristics are attractive areas of pharmaceutical research. The physicochemical

properties of triblock copolymers (TBPs) can be tailored by varying the individual block

chain lengths.   Triblock copolymers, of various ethylene oxide (EO) and propylene

oxide (PO) block lengths, are explored in various drug delivery applications including the

delivery to the central nervous system (CNS) across the blood brain barrier (BBB),[1] oral

delivery of drugs,[2] and tumor-specific delivery of antineoplastic agents.[3] Moreover, it is

now realized that TBPs used for drug delivery cannot be considered only as inert

components that protect drugs from degradation and increase the circulation time.[4] TBPs

can induce gene expression through mechanisms that differ from the delivery of DNA

into a cell. Kabanov's group made significant contributions in the development of

Pluronic micelles as a tool for enhancing drug delivery to multidrug resistant cells.[5] Thus,

it is becoming increasingly evident that certain nanoparticles with particular properties

can circumvent several defense mechanisms, providing an alternative delivery vehicle.[6]

In the first part of the thesis, we used a novel approach to characterize the

temperature dependent aggregation behavior of commercial F127 samples based on

antioxidant molecules like BHT. We showed that the fluorescence of BHT is sufficiently

sensitive to its microenvironment to be used as a reliable marker of temperature-induced

micellization. In the absence of F127, collisional quenching of the BHT fluorescence is

observed associated with higher temperature. The BHT fluorescence method for determining the concentration and temperature dependent Pluronic F127 aggregation was described. Since trace levels of BHT are present in commercial F127 preparations as a preservative, the BHT fluorescence may provide researchers a convenient way to characterize polymer aggregation without having to add an external dye. An important application of this novel method is the *in-situ* characterization of the temperature-dependent aggregation of commercial Pluronic batches. Additionally, this approach to determine the CMC and CMT can be applied to any copolymer system that contains phenolic antioxidants such as BHT. With increasing temperature above the CMT, light scattering results suggest the coalescence of micelles, PPO core dehydration, and decreased heterogeneity in micelle size distributions. The electronic BHT transitions are directly impacted by the local environment where the partitioning in the micelle is influenced by steric and hydrogen bonding interactions with the PEO and PPO segments. This is the case when the changes in the fluorescence intensities with increasing temperature are compared. A higher fluorescence intensity value with increasing temperature implies greater accommodation to the PPO environment reflecting the higher quantum yield of BHT in the micelle interior. Furthermore, DLS, AFM and TEM data show high micellar heterogeneity around the CMT lending support to a multi-step model of aggregation.

We next explored the synthesis and characterization of the gold nanoparticles using environmentally benign and cost effective reagents. The concerns for the environmental and economic impact of organic solvents and detergents in gold nanoparticle (AuNP) synthesis increased recently.[7] These concerns motivated this

research for more environmentally benign alternatives. One approach is to synthesize AuNPs from tetrachloroauric (III) acid ($HAuCl_4$) using triblock copolymers (TBPs). However, a major challenge to using TBPs is the heterogeneous nature of the formed nanocrystals. Establishing control over AuNP size and shape requires a detailed mechanistic understanding of precursor reduction and nanoparticle growth. By using mixtures of TBPs (L31 and F68), a more flexible method for adjusting the hydrophobic/hydrophilic environment is demonstrated. This method also allows us to tune the size and shape. It is shown that adjusting the TBP/Au (III) ratio can change AuNP morphology and size. Kinetic models are used to rationalize why the addition of L31 slows the rate of AuNP formation and growth. Experimental evidence of sigmoidal growth kinetics, early time bimodal gold nanoparticle size distributions and polycrystallinity suggest that aggregative AuNP growth is an important mechanism.

The nucleation and growth of anisotropic gold nanoparticles were accomplished using nonionic TBPs. Kinetic control was achieved by varying the Pluronic/Au (III) ratio. The yields and sizes of anisotropic nanoparticles are higher in L31/F68 solutions than in F68 alone. The presence of the L31 inhibited the rate of primary nanocrystal formation and subsequent growth. Our simple kinetic model includes noncompetitive inhibition where L31 induces changes in the F68 conformation that prevents F68 EO_x units from binding to gold ions. The role of the L31 in the growth phase producing higher energy nanostructures having larger surface areas may be caused by the inhibition of growth on certain crystallographic faces.

The kinetic models presented here can be extended as an empirical tool to quantify the effect of reaction conditions on AuNP size and shape. At the limit of low

124

initial Au (III) concentration, the rate of nanocrystal seed formation is proportional to Au (III) concentration. In this regime, it is predicted that the particle sizes will be proportional to Au (III) concentration. When $K_m \sim$ Au (III) concentration, the AuNPs produced are polydisperse with multiple size populations. At the limit of high Au (III) concentration, rate of the nanoparticle growth is constant giving an upper limit of AuNP number density and hence an upper limit of AuNP size.

The usefulness of the approach presented in this work derives from the observation that the kinetics of gold growth can be modified through the optimization of the phase behavior of quaternary mixtures of hydrophobic (mostly PPO) and hydrophilic (mostly PEO) block copolymers with water and Au (III). The data suggest that the yield of nanoplates may be further optimized via changes in ion/seed concentration, temperature and block copolymer binary mixture composition. A dissipative particle dynamics simulation of gold nanoparticles in PEO−PPO−PEO micelles indicates that gold atoms are wrapped by the copolymer and form spherical particles inside the micelles.[8] The hydrophobic PO segments are adsorbed on the surface of AuNPs, whereas the hydrophilic EO segments are exposed to water forming stable Pluronic-gold colloids with two-layer structures. This simulated dynamic process suggests that the morphology (shape and size) of gold nanoparticles depend on the competition between the aggregation of gold clusters and stabilization by block copolymer micelles.

Sakai and Alexandridis using a TBP with a PO/EO ratio of 0.9 in Pluronic L64 ($EO_{13}-PO_{30}-EO_{13}$) achieved high yields of micro plates.[9] They argued that more anisotropic particles were produced at this PO/EO ratio because reduction on the PEO ether backbone becomes the rate-limiting step. They further attributed the origin of the

125

plate morphology to AuCl$_4$ reduction on the facets instead of the shape-directing action of the polymeric lyotropic liquid crystals as "soft" templates. In general, larger gold particles are produced by Pluronics having shorter PEO blocks because the rate of metal ion reduction appears to be limited by reduction on the gold surface instead of in the bulk solution.[10] Furthermore, published results of TBP facilitated Au (III) reduction suggest that the interdependence of block copolymer adsorption on different facets of the growing crystal and crystal growth kinetics (rate of metal ion reduction) could determine nanoparticle shape.[8-9, 11]

The importance of the desired shape and size in gold nanoparticles for pharmaceutical uses cannot be underestimated. The functional properties of gold nanoparticles to a large degree are dependent on their size and shape. Gold spherical nanoparticles have a greater efficiency of uptake compared to gold nanorods due to the thermodynamic driving forces for membrane wrapping and receptor kinetics.[12] Gold nanorods are reported to be more toxic compared to spherical particles,[13] but it is likely that the toxicity is due to the unbound CTAB surfactant.

Seeded growth route to synthesize monodisperse TBP stabilized AuNPs was made a further subject of this research. This was accomplished through the kinetic controls of the various reaction conditions. Three different aspects are very crucial in obtaining Au NPs with large size and good stability. First is the decrease in temperature of the solution. This allows a slowing down of the reaction mixture and prevention of secondary nucleation. Secondly, the control of the reaction pH further allows control of the reactivity of gold species. This is an important step in improving the monodispersity of the secondary particles. Thirdly, the number of Au atoms introduced in each growth

step permits the shifting of the system towards the focusing conditions. In this way the AuNP final distributions can narrow down resulting in the AuNPs with focused diameters. The ability to synthesize triblock copolymer-stabilized AuNPs with particular dimensions, with a controlled concentration and surface state, allows further expansion of the applicability of these NPs to biomedical applications.

The goal of this proposed research was to increase the mechanistic understanding of the nucleation and growth of gold nanoparticles (Au NPs) from tetrachloroauric (III) acid ($HAuCl_4$) using triblock non-ionic block copolymers (TBPs) of poly (ethylene oxide) (PEO) and poly (propylene oxide) (PPO). Our goals were accomplished by varying the TBP/Au (III) ratios. We learned that the Au NP shape and size can be optimized by adjusting the parameters of TBP/Au ratio and Au NP seed size and concentration. Furthermore, in the seeding methodology, Au NPs are present initially in the precursor solutions. We have shown that by varying the TBP/Au ratio and seed concentration, results in changing Au NP size and shape.

References

1. (a) Kabanov, A. V.; Batrakova, E. V.; Miller, D. W., Pluronic® block copolymers as modulators of drug efflux transporter activity in the blood–brain barrier. *Adv. Drug Delivery Rev.* **2003,** *55* (1), 151-164; (b) Spitzenberger, T. J.; Heilman, D.; Diekmann, C.; Batrakova, E. V.; Kabanov, A. V.; Gendelman, H. E.; Elmquist, W. F.; Persidsky, Y., Novel delivery system enhances efficacy of antiretroviral therapy in animal model for HIV-1 encephalitis. *J. Cereb. Blood Flow Metab.* **2006,** *27* (5), 1033-1042.

2. Batrakova, E. V.; Han, H.-Y.; Alakhov, V. Y.; Miller, D. W.; Kabanov, A. V., Effects of Pluronic Block Copolymers on Drug Absorption in Caco-2 Cell Monolayers. *Pharm. Res.* **1998,** *15* (6), 850-855.

3. Kabanov, A.; Alakhov, V., Pluronic block copolymers in drug delivery: from micellar nanocontainers to biological response modifiers. *Crit. Rev. Ther. Drug. Carr. Syst.* **2002,** *19* 1-72.

4. Hongrapipata, J.; Kopečkováa, P.; Prakongpan, S.; Kopečeka, J., Enhanced antitumor activity of combinations of free and HPMA copolymer-bound drugs *Int. J. Pharm.* **2008,** *351*, 259-270.

5. (a) Kabanov, A. V., Polymer genomics: An insight into pharmacology and toxicology of nanomedicines. *Adv. Drug Deliv. Rev.* **2006,** *58* (15), 1597-1621; (b) Kabanov, A. V.; Batrakova, E. V.; Alakhov, V. Y., Pluronic® block copolymers for overcoming drug resistance in cancer. *Adv. Drug Deliv. Rev.* **2002,** *54* (5), 759-779.

6. (a) Davis, S. S., Biomédical applications of nanotechnology — implications for drug targeting and gene therapy. *Trends Biotechnol.* **1997,** *15* (6), 217-224; (b) Kwon, G. S.; Okano, T., Polymeric micelles as new drug carriers. *Adv. Drug Delivery Rev.* **1996,** *21* (2), 107-116; (c) Panyam, J.; Labhasetwar, V., Biodegradable nanoparticles for drug and gene delivery to cells and tissue. *Adv. Drug Delivery Rev.* **2003,** *55* (3), 329-347; (d) Kataoka, K.; Harada, A.; Nagasaki, Y., Block copolymer micelles for drug delivery: design, characterization and biological significance. *Adv. Drug Delivery Rev.* **2001,** *47* (1), 113-131; (e) Xie, J.; Lee, S.; Chen, X., Nanoparticle-based theranostic agents. *Adv. Drug Delivery Rev.* **2010,** *62* (11), 1064-1079; (f) Ghosh, P.; Han, G.; De, M.; Kim, C. K.; Rotello, V. M., Gold nanoparticles in delivery applications. *Adv. Drug Delivery Rev.* **2008,** *60* (11), 1307-1315.

7. Alexandridis, P., Gold Nanoparticle Synthesis, Morphology Control, and Stabilization Facilitated by Functional Polymers. *Chem. Eng. Technol.* **2011,** *34* (1), 15-28.

8. Chen, S.; Guo, C.; Hu, G.-H.; Liu, H.-Z.; Liang, X.-F.; Wang, J.; Ma, J.-H.; Zheng, L., Dissipative particle dynamics simulation of gold nanoparticles stabilization by

PEO–PPO–PEO block copolymer micelles. *Colloid Polym. Sci.* **2007,** *285* (14), 1543-1552.

9. Sakai, T.; Alexandridis, P., High-Yield Synthesis of Gold Microplates Using Amphiphilic Block Copolymers: Are Lyotropic Liquid Crystals Required? *Macromol. Symp.* **2010,** *289* (1), 18-24.

10. (a) Sakai, T.; Alexandridis, P., Single-Step Synthesis and Stabilization of Metal Nanoparticles in Aqueous Pluronic Block Copolymer Solutions at Ambient Temperature. *Langmuir* **2004,** *20* (20), 8426-8430; (b) Sakai, T.; Alexandridis, P., Mechanism of metal ion reduction, nanoparticle growth and size control in aqueous amphiphilic block copolymer solutions at ambient conditions. *J. Phys. Chem. B* **2005,** *109* (16), 7766–7777; (c) Sakai, T.; Alexandridis, P., Size- and shape-controlled synthesis of colloidal gold through autoreduction of the auric cation by poly(ethylene oxide)–poly(propylene oxide) block copolymers in aqueous solutions at ambient conditions. *Nanotechnology* **2005,** *16* (7), S344.

11. Rahme, K.; Gauffre, F.; Marty, J.-D.; Payré, B.; Mingotaud, C., A Systematic Study of the Stabilization in Water of Gold Nanoparticles by Poly(Ethylene Oxide)−Poly(Propylene Oxide)−Poly(Ethylene Oxide) Triblock Copolymers. *J. Phys. Chem. C* **2007,** *111* (20), 7273-7279.

12. Chithrani, B. D.; Ghazani, A. A.; Chan, W. C. W., Determining the Size and Shape Dependence of Gold Nanoparticle Uptake into Mammalian Cells. *Nano Lett.* **2006,** *6* (4), 662-668.

13. Li, Y.-F.; Chen, C., Fate and Toxicity of Metallic and Metal-Containing Nanoparticles for Biomedical Applications. *Small* **2011,** *7* (21), 2965-2980.

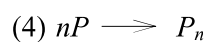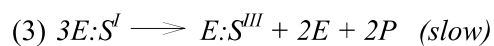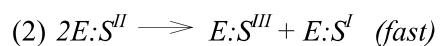APPENDIX

DERIVATION OF THE KINETIC EQUATION 2

Define EO_x blocks of F68 as *[E]* and $HAuCl_4$ as *[S]*. The inhibition of Au reduction is from the PO_y blocks of L31 labeled *[L]* we define *P* as *Au(0).*

S^{III}, S^{II}, S^I = *Au(III), Au(II), Au(I)*

E = EO_x blocks of *F68*

I = EO_y blocks of *L31*

P = *Au (0)*

    (1) S^{III} + *E* $\rightleftarrows$ *E:*S^{III} $\longrightarrow$ *E:*S^{II}

    (2) *2E:*S^{II} $\longrightarrow$ *E:*S^{III} + *E:*S^I *(fast)*

    (3) *3E:*S^I $\longrightarrow$ *E:*S^{III} + *2E* + *2P*   *(slow)*

    (4) *nP* $\longrightarrow$ P_n

Reactions (2) and (3) are disproportionation reactions

In the absence of inhibition:

E_T = *[E]* + *[E:S]* where

E is free EO_x blocks not bound to gold ions

E:S represents *EO*$_x$: gold complexes Au(III, II, I)

Part 1:

Use steady state approximation to prove $\frac{dP}{dt} \alpha [Au(III)]$

Rate of formation of gold:

$$\frac{dP}{dt} = k_4[E:S^I]^3$$

(5) $\frac{d[E:S^{II}]}{dt} = k_2[E:S^{III}] - k_3[E:S^{II}]^2$

(6) $\frac{d[E:S^I]}{dt} = k_3[E:S^{II}]^2 - k_4[E:S^I]^3$

$\frac{d[E:S^I]}{dt} \approx 0$ From equation 5

$k_3[E:S^{II}]^2 = k_2[E:S^{III}]$

$[E:S^{II}] \approx \sqrt{\frac{k_2[E:S^{III}]}{k_3}}$

(7) Define $k_3' \approx \sqrt{\frac{k_2}{k_3}}$

(8) Hence $[E:S^{II}] = k_3'[E:S^{III}]^{\frac{1}{2}}$

$$\frac{d[E:S^I]}{dt} = k_3[E:S^{II}]^2 - k_4[E:S^I]^3 \approx 0$$

Sub (8) into (6)

$$k_3 k_3'[E:S^{III}] - k_4[E:S^I]^3 \approx 0$$

Define $k_3'' = \left(\dfrac{k_3 k_3'}{k_4}\right)^{\frac{1}{3}}$

(9) $[E:S^I] = k_3''[E:S^{III}]^{\frac{1}{3}}$

(10) Thus $\dfrac{dP}{dt} = k_3 k_3''[E:S^{III}] = k_4'[E:S^{III}]$

(11) $[E_T] = [E] + [E:S^{III}]$ E_T = total concentration of EO_x block

$[E] = EO_x$ free (not bound to gold) – cannot be measured

$[E:S^{III}] = EO_x{:}Au^{III}$ complex

(12) $\dfrac{1}{K_m} = \dfrac{[S^{III}][E]}{[E:S^{III}]}$ $\dfrac{1}{K_m}$ = dissociation constant

Sub $[E] = [E_t] - [E:S^{III}]$

$\dfrac{k_1}{k_{-1}} = \dfrac{1}{K_m} = \dfrac{[S^{III}][E_T - [E:S^{III}]]}{[E:S^{III}]}$

(13) $[E:S^{III}] = \dfrac{E_T[S^{III}]}{K_m + [S^{III}]}$

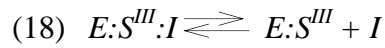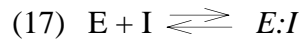(14) $\dfrac{dP}{dt} = k_4' \dfrac{E_T[S^{III}]}{K_m + [S^{III}]}$

(15) In the limit of high $[S]$ concentration define $R_{\max} = k_4''[E_T]$

(16) Thus $\dfrac{dP}{dt} = \dfrac{R_{\max}[S^{III}]}{K_m + [S^{III}]}$

132

Hence $\qquad \frac{dP}{dt} \alpha \, [Au(III)]$

Part 2: Inhibition

(16a) $[E_T] = [E] + [E:S^{III}] + [E:I] + [E:S^{III}:I]$

(17) $\mathrm{E + I} \rightleftharpoons E{:}I$

(18) $E{:}S^{III}{:}I \rightleftharpoons E{:}S^{III} + I$

(19) $K_m = \dfrac{[S^{III}][E]}{[E:S^{III}]}$

(20) $K_1 = \dfrac{[E][I]}{[E:I]}$

(21) $K_1^{'} = \dfrac{[E:S^{III}][I]}{[E:S^{III}:I]}$

(22) From equation (19): $[E] = K_m \dfrac{[E:S^{III}]}{[S^{III}]}$ (19a)

From equation (20): $[E:I] = K_m \dfrac{[E][I]}{K_1}$ (20a)

Substitute (19a) into (20a)

(23) $[E:I] = K_m \dfrac{[E:S^{III}][E][I]}{K_1[S^{III}]}$

From equation (21) $[E:S^{III}:I] = K_m \dfrac{[E:S^{III}][I]}{K_1^{'}}$ (21a)

Insert equations (19a), (21a), and (22) into (16a)

133

$$(24) \quad [E_T] = K_m \frac{[E:S^{III}]}{[S^{III}]} + [E:S^{III}] + K_m \frac{[E:S^{III}][E][I]}{K_1[S^{III}]} + \frac{[E:S^{III}][I]}{K_1'}$$

Rearrange (23)

$$[E_T] = [E:S^{III}] \left(\frac{K_m}{[S^{III}]} + 1 + \frac{K_m[I]}{K_1[S^{III}]} + \frac{[I]}{K_1'} \right)$$

$$[E_T] = [E:S^{III}] \left(\frac{K_m}{[S^{III}]} \left(\frac{K_m}{[S^{III}]} + \frac{[I]}{K_1} \right) + \left(1 + \frac{[I]}{K_1'} \right) \right)$$

$$(25) \quad [E] = [E:S] \left(\frac{K_m}{[S^{III}]} \alpha + \alpha' \right)$$

Where,

$$(26) \quad \alpha = \left(1 + \frac{[I]}{K_1} \right)$$

$$(27) \quad \alpha = \left(1 + \frac{[I]}{K_1'} \right)$$

We know form (10) that $R = k_4'[E:S^{III}]$

$$(28) \quad R = \frac{k_4'[E]}{\left(\frac{K_m}{[S^{III}]} \alpha + \alpha' \right)} = \frac{k_4'[E][S^{III}]}{\left(\alpha K_m + \alpha'[S^{III}] \right)}$$

Here α and α' represent the inhibiting effects of L31. In the absence of L31 $\alpha = \alpha'$

=1. The term $k_4'[E_T]$ corresponds to the rate in the limit of high Au^{III} concentration, in

other words when $S^{III} \gg K_m$. Under such conditions and L31 is absent $R = k_4'[E_T]$.

$$(29) \quad R = \frac{k_4'[E][S^{III}]}{\left(\alpha K_m + \alpha'[S^{III}]\right)} = \frac{R_{max}[S^{III}]}{\left(\alpha K_m + \alpha'[S^{III}]\right)} \quad \text{(from equation 15)}$$